Electron source for sub-relativistic single-shot femtosecond diffraction

Document status and date:
Published: 01/01/2010

Document Version:
Publisher's PDF, also known as Version of Record (includes final page, issue and volume numbers)

Please check the document version of this publication:

• A submitted manuscript is the version of the article upon submission and before peer-review. There can be important differences between the submitted version and the official published version of record. People interested in the research are advised to contact the author for the final version of the publication, or visit the DOI to the publisher's website.
• The final author version and the galley proof are versions of the publication after peer review.
• The final published version features the final layout of the paper including the volume, issue and page numbers.

Link to publication

Electron source for sub-relativistic single-shot femtosecond diffraction

PROEFSCHRIFT

ter verkrijging van de graad van doctor aan de
Technische Universiteit Eindhoven, op gezag van de
rector magnificus, prof.dr.ir. C.J. van Duijn, voor een
commissie aangewezen door het College voor
Promoties in het openbaar te verdedigen
op maandag 13 december 2010 om 16.00 uur

door

Thijs van Oudheusden

geboren te Bergen op Zoom

Dit proefschrift is goedgekeurd door de promotoren:

prof.dr. M.J. van der Wiel
en
prof.dr. K.A.H. van Leeuwen

Copromotor:
dr.ir. O.J. Luiten

Contents

This thesis is partially based on the following publications:

- Chapter 3:
  T. van Oudheusden, E. F. de Jong, S. B. van der Geer, W. P. E. M. Op 't Root, O. J. Luiten, and B. J. Siwick, *J. Appl. Phys.*, 102:093501, 2007.

- Chapter 6:
  T. van Oudheusden, P. L. E. M. Pasmans, S. B. van der Geer, M. J. de Loos, M. J. van der Wiel, and O. J. Luiten, submitted to *Phys. Rev. Lett.* and available at *arXiv*, 1006.2041v1 [physics.acc-ph], 2010.

1

Introduction

This thesis describes the introduction of the fourth dimension, time, in electron optics for sub-relativistic electrons. This development has led to the demonstration of a device that allows recording of a diffraction pattern in a single shot of femtosecond duration. This is the main reason for the development of billion dollar X-ray Free Electron Lasers (X-FELs). In this thesis we present the development of the electron-counterpart, which can be considered a 'poor man's X-FEL'. Below we describe the background of this development.

1.1   Electron and X-ray crystallography

Electron and X-ray crystallography are powerful techniques for structural analysis on the atomic scale. Both techniques have been following a similar development in time. In particular in the last decade, both are moving into new exciting regimes.

A powerful, widely used type of X-ray source is the synchrotron. This source provides high intensity X-ray pulses with broad spectra, from which the desired wavelength can be selected. About 50 facilities world-wide are in operation today, each with tens of beamlines, which have become indispensable analytical tools for scientists in the fields of condensed matter, material science, (bio-)chemistry, and structural biology [1]. Synchrotrons have been particulary successful in unravelling the complex 3-dimensional (3D) atomic structures of bio-molecules, as evidenced by the exponentially growing number of deposits in the protein data bank [2].

However, nearly all studies up to now have been done on equilibrium states. An exciting prospect is the study of structural dynamics with both spatial *and* temporal atomic resolution. To resolve atomic motions in, e.g., chemical reactions and phase transitions a temporal resolution of typically 100 fs is required. With the development of femtosecond lasers in the 1980s this atomic timescale has come within reach, providing the possibility to trigger, or 'pump', a sample at an instant in time, thereby initiating, e.g., a phase transition, a chemical reaction, or a conformation change. By probing the sample with ultrashort X-ray pulses at various time-delays with respect to a synchronized pump pulse, a 'molecular movie' may be recorded. Following such a pump-probe strategy Schotte et al. used synchrotron radiation in a 100-ps pulsed mode to study photolysis-induced migration of CO-groups in myoglobin [3]. However, to resolve structural dynamics at a truly atomic temporal scale X-ray pulses shorter than 100 fs are required, preferably of sufficient brightness to record a diffraction

pattern in a single shot. With the recent commissioning of the first hard X-ray free electron laser (X-FEL) at LCLS [4] single-shot, femtosecond X-ray diffraction experiments are now in principle possible. This marks the beginning of a new era in (bio-)chemistry, condensed matter physics, material science, and the life sciences.

In parallel, electron techniques have also evolved in a spectacular way. An important property of electrons is that their trajectories are fully controllable with electro-magnetic fields. As a result, charged-particle optics have been developed, which provide the possibility to directly image atomic configurations. This is in contrast with X-ray techniques, which can only operate in diffraction mode. The first electron microscope was already demonstrated in the 1930s by Ernst Ruska. The development of high-brightness electron sources and aberration corrected lens systems have recently culminated in transmission electron microscopy (TEM) with a spatial resolution smaller than $1\,\text{Å}$, i.e., less than the size of an atom [5]. The ultimate goal would be $100\,\text{fs}$ TEM. An interesting recent development in this perspective is so-called 'dynamic' TEM (DTEM)[6], where a single nanosecond electron pulse carries sufficient charge to make a full image. However, even for these relatively long pulse durations ($\sim 1\,\text{ns}$) Coulomb forces between the electrons spoil the beam, resulting in $\gtrsim 1\,\text{nm}$ spatial resolution. With present-day technology it is impossible to pack $\gtrsim 10^8$ electrons -required for a full image- in a $100\,\text{fs}$ pulse, while still obtaining sub-nm resolution.

By leaving out the imaging lens and working in the diffraction mode, however, typically about 100 times fewer electrons are required, and a lower beam quality, in terms of angular spread and energy spread, is allowed to capture a high-quality diffraction pattern.

There are thus two promising techniques to study structural dynamics with atomic resolution at the femtosecond timescale: ultrafast X-ray diffraction and ultrafast electron diffraction (UED). The obvious question arises why one should use electrons, as a first X-FEL (LCLS) has recently become operational. The fundamental difference between X-ray and electron diffraction is the interaction with the sample: hard X-rays scatter mainly off the inner shell electrons, whereas electrons scatter mainly off the atomic nuclei themselves. The different interaction mechanisms lead to other differences between X-ray and electron crystallography, which are summarized in Table 1.1.

Firstly, the different mean free paths of X-rays and electrons naturally favor electrons when studying thin films (in transmission) or surfaces (in reflection). X-rays are favored for the study of thicker samples. But the main difference is sample damaging. Using X-rays, more than three times as many inelastic scattering events happen per useful, i.e., elastic scattering event. Moreover, per inelastic event the energy deposited is about a 1000 times more than for electrons. An ultrashort X-ray pulse will therefore generally destroy a sample, making it useless for further experiments. This is mainly a problem for, generally delicate, biological samples. Important practical advantages of electron diffraction setups are the relatively small scale and relatively low cost, compared to billion dollar facilities like an X-FEL.

These considerations underly the efforts being made in various laboratories to develop ultrafast electron diffraction.

Table 1.1: *X-ray versus electron diffraction.*

property	X-rays (10 keV)	electrons (100 keV)
wavelength	1.2 Å	0.037 Å
elastic mean free path (relative to electrons)	$10^5 - 10^6$	1
ratio inelastic/elastic scattering	10	3
energy deposited per elastic event (relative to electrons)	1000	1
damage mechanism	photoelectric effect	secondary electron emission

1.2 Ultrafast electron diffraction: fighting the Coulomb force

To obtain a high-quality diffraction pattern typically 10^6 electrons are required in low-emittance pulses. The space-charge forces in a pulse containing that number of electrons, are still broadening the pulse to durations longer than 100 fs. Several approaches to circumvent this space-charge problem have been attempted.

The obvious way to avoid the space-charge expansion is by using only a single electron per pulse. To limit the time necessary to build up a diffraction pattern the repetition frequency is raised to several MHz [7]. In this approach the temporal resolution is determined by the jitter of the arrival time of the individual electrons at the sample. Simulations show that, using radio-frequency (RF) acceleration fields, the individual electrons could arrive at the sample within a time-window of several fs (possibly even sub-fs) [8]. This single-electron approach, however, requires that the sample be reproducibly pumped and probed $\sim 10^6$ times to obtain a diffraction pattern of sufficient quality. This strategy has been adopted by the CalTech group of Zewail. He uses a femtosecond laser to extract on average less than a single electron per pulse from a field-emission tip in an otherwise regular electron microscope [9]. This technique is called ultrafast electron microscopy (UEM), which includes imaging, diffraction, and electron energy loss spectroscopy (EELS) [10]. Examples of exciting studies with the aid of UEM are structural changes of interfacial water (on a hydrophilic surface) [11], structural dynamics of impulsive laser-excited graphite [12], and the transition of high-temperature superconducting cuprates to the metallic state initiated by heating with a femtosecond laser pulse [13].

A second approach is to extract ~ 1 fC electron bunches by femtosecond photoemission from a flat metal photocathode, and to put the sample at a position as close as possible to the accelerator. In this way there is simply less time for the Coulomb force to broaden the pulse. Using this strategy Siwick *et al.* studied the structural dynamics of melting aluminum with ~ 300 fs resolution [14]. Current state-of-the-art compact electron photoguns provide sub-ps electron bunches, containing several thousand electrons per bunch at sub-100 keV energies [15, 16]. Space-charge effects limit the number of electrons to less than 10^4 per bunch for applications requiring high temporal resolution. The closest to single-shot, femtosecond operation has been achieved by Sciaini et al., who used bunches containing 10^4 electrons and integrated 4-12 shots per time point to monitor electronically driven atomic motions of Bi [17] with 350 fs resolution.

A third method to overcome space-charge problems is to accelerate the bunch to relativistic speeds as quickly as possible. Close to the speed of light the Coulomb repulsion is effectively suppressed by relativistic effects. Bunches of several hundred femtosecond durations, containing several pC, are routinely available from RF photoguns. The application of such a device in an electron diffraction experiment was recently demonstrated [18, 19]. However, energies in the MeV range pose their own difficulties, including the very short De Broglie wavelength λ ($\approx 0.002\,\text{Å}$ at $5\,\text{MeV}$), radiation damage to samples, reduced cross-section for elastic scattering, non-standard detectors and general expense of the technology.

1.3   Waterbag electron bunches: using the Coulomb force

Briefly, electron crystallographers would prefer to work in the $30 - 300\,\text{keV}$ energy range, with bunch charges $\gtrsim 0.1\,\text{pC}$ (i.e., $\gtrsim 10^6$ electrons), while maintaining a high-quality beam and better than $100\,\text{fs}$ temporal resolution. The ultimate goal can therefore be formulated as an electron diffraction setup with X-FEL capabilities, i.e., single-shot operation on the atomic spatio-temporal scale. However, none of the approaches treated in the previous section is able to reach this goal. Those are based on the idea that the problem of ultrashort electron bunches is the strong Coulomb repulsion associated with the high charge density. Fundamentally, however, the *magnitude* of the charge density is not the real problem, but the charge *distribution*. This problem is solved by creating a bunch, of which the space-charge density distribution gives rise to fully controllable, i.e., linear[1], space-charge fields. This is the case for a 3-dimensional ellipsoid with a uniform charge density, also called a *waterbag* bunch. Of course the waterbag bunch still explodes due to Coulomb's force, but it retains its uniform ellipsoidal distribution and thus its linear space-charge fields. Because of its linear space-charge fields a waterbag bunch can be compressed reversibly in the transverse and longitudinal direction with electro-magnetic lenses that have linear fields.

A waterbag bunch can be created by the space-charge blow-out of an ultrathin sheet of electrons as produced in a femtosecond-laser driven photogun, which under certain conditions evolves into a waterbag bunch [20]. The first realization of relativistic waterbag bunches has been shown by Musumeci et al. [21].

1.4   Scope of this thesis

The experiments described in this thesis involve 100-fold compression of $95\,\text{keV}$ (waterbag) bunches to sub-$100\,\text{fs}$ durations. Thereby we realized sub-relativistic electron bunches, that are suitable for single-shot femtosecond electron diffraction. The novel way to realize these bunches is based on a linear space-charge-induced expansion of the electron bunch [20], followed by compression using the time-dependent field sustained in a RF cavity. This compression principle is schematically shown in Fig. 1.1. By synchronizing the phase offset of the RF field to our photoemission laser pulses, we are able to inject a bunch into the cavity at a phase such that the faster electrons at the front of the bunch are decelerated and the slower electrons at the back are accelerated. The inversion of the longitudinal velocity-position

---

[1]Throughout this theses we use 'linear' as a short way of saying 'a linear function of position'.

correlation by the action of the RF field leads to bunch compression in the subsequent drift space.

In Ch. 2 some basic theory concerning waterbag electron bunches is presented. The recipe to create such bunches is described, and the expansion of ultrathin bunches into a fully-fledged ellipsoid is treated analytically. Next, in Ch. 3 we describe the concept of our novel UED source, which relies on the compression of ellipsoidal electron bunches by means of a RF field. The setup itself consists of a 100 kV DC photogun that is described in more detail in Ch. 4, and of a 3 GHz RF cavity that is described in more detail in Ch. 5. With this novel UED source sub-relativistic, space-charge-dominated, sub-100-fs electron bunches have been realized, as shown in Ch. 6. This constitutes the first demonstration of the introduction of the fourth dimension in sub-relativistic electron optics. In Ch. 7 we discuss some basic electron diffraction theory, which we use to analyze an actual diffraction pattern of a gold film that we recorded with a single electron pulse. The recording of this high-quality diffraction pattern confirms that our bunches are suitable for single-shot UED. As such, we have demonstrated the operation of a 'poor man's X-FEL'. Preliminary measurements of the transverse phase-space of -presumably waterbag- bunches produced with our photogun are presented in Ch. 8. Finally, in Ch. 9 we summarize our main conclusions and we describe the potential for extending the applicability of our femtosecond diffraction source to the regime of large (bio-)molecules.
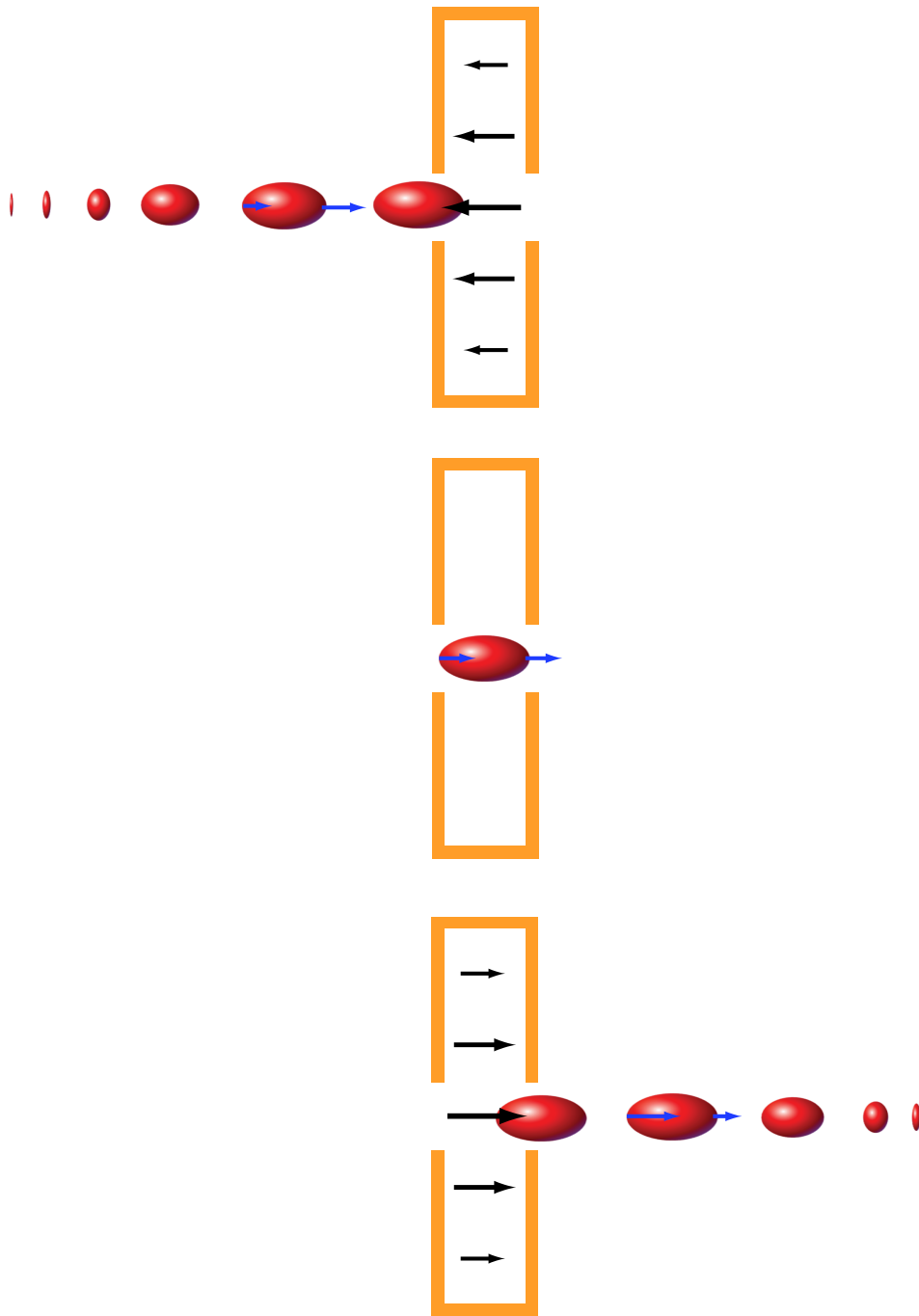
Figure 1.1: *Principle of longitudinal compression of a (waterbag) electron bunch with a RF cavity. From top to bottom the same cavity is shown at increasing phase of a single RF cycle. (top) While traveling towards the cavity the bunch is expanding, as indicated by the blue velocity vectors. (Multiple bunches are shown for clarity.) The bunch enters the cavity when the force (black arrows) exerted by the RF field is decelerating. (center) While the bunch travels through the cavity the RF field goes through zero and will change sign. (bottom) As a result electrons at the back of the bunch are accelerated, such that they will overtake the front electrons in the subsequent drift space.*

References

[1] D. H. Bilderback, P. Elleaume, and E. Weckert, J. Phys. B **38** (2005).

[2] Research Collaboratory for Structural Bioinformatics (RCSB) Protein Data Bank (PDB), http://www.pdb.org/.

[3] F. Schotte, M. Lim, T. A. Jackson, A. V. Smirnov, J. Soman, J. S. Olson, G. N. Philips Jr., M. Wulff, and P. A. Anfinrud, Science **300**, 1944 (2003).

[4] B. McNeil, Nature Photonics **3**, 375 (2009).

[5] D. Hubert, Microscopy **16** (2007).

[6] T. LaGrange *et al.*, Appl. Phys. Lett. **89** (2006).

[7] J. D Geiser, and P. M. Weber, High repetition rate time-resolved gas phase electron diffraction, in *Proceedings of the SPIE conference on Time-Resolved Electron and X-Ray Diffraction*, volume 2521, page 136, 1995.

[8] E. Fill, L. Veisz, A. Apolonski, and F. Krausz, New J. Phys. **8**, 272 (2006).

[9] V. A. Lobastov, R. Srinivasan, and A. H. Zewail, Proc. Natl. Acad. Sc. USA **102** (2005).

[10] A. H. Zewail, Science **328**, 187 (2010).

[11] D.-S. Yang, and A. H. Zewail, Proc. Natl. Acad. Sc. USA **106** (2009).

[12] F. Carbone, P. Baum, P. Rudpolf, and A. H. Zewail, Phys. Rev. Lett. **100** (2008).

[13] F. Carbone, D.-S. Yang, E. Giannini, and A. H. Zewail, Proc. Natl. Acad. Sc. USA **105** (2008).

[14] B. J. Siwick, J. R. Dwyer, R. E. Jordan, and R. J. D. Miller, Science **302**, 1382 (2003).

[15] C. T. Hebeisen, G. Sciaini, M. Harb, R. Ernstorfer, T. Dartigalongue, S. G. Kruglik, and R. J. D. Miller, Opt. Express **16**, 3334 (2008).

[16] M. Harb, R. Ernstorfer, T. Dartigalongue, C. T. Hebeisen, R. E. Jordan, R. J. D. Miller, J. Phys. Chem. B **110**, 25308 (2006).

[17] G. Sciaini *et al.*, Nature **456**, 56 (2009).

[18] J. B. Hastings, F. M. Rudakov, D. H. Dowell, J. F. Smerge, J. D. Cardoza, J. M. Castro, S. M. Gierman, H. Loos, and P. M. Weber, Appl. Phys. Lett. **89**, 184109 (2006).

[19] P. Musumeci, J. T. Moody, C. M. Scoby, M. S. Gutierrez, H. A. Bender, and N. S. Wilcox, Rev. Sci. Instrum. **81**, 013306 (2010).

[20] O. J. Luiten, S. B. van der Geer, M. J. de Loos, F. B. Kiewiet, and M. J. van der Wiel, Phys. Rev. Let. **93**, 094802 (2004).

[21] P. Musumeci, J. T. Moody, R. J. England, J. B. Rosenzweig, and T. Tran, Phys. Rev. Lett. **100**, 244801 (2008).

2

Uniformly charged ellipsoidal electron bunches

In classical physics an ensemble of N particles, such as an electron bunch, is fundamentally described in a 6N-dimensional phase-space. For the particular case of identical, non-interacting particles this reduces to a 6-dimensional (6D) phase-space, in which the local density along a trajectory is a conserved quantity, according to Liouville's theorem. Beam physics involves the control of the phase-space of the beam, ideally with linear electro-magnetic fields to prevent beam deterioration. For interacting particles, such as electrons in a bunch, Liouville's theorem still applies if statistical Coulomb effects can be neglected, i.e., if the space-charge field can be described by a mean field [1]. These space-charge fields, however, are generally nonlinear functions of position, resulting in a nonlinear phase-space distribution. The only charged particle distribution of which the space-charge fields are linear functions of position, is a uniformly charged ellipsoid. If the particles initially have zero velocity (or, to put it differently, zero temperature), these linear fields give rise to linear phase-space distributions even in the presence of strong space-charge fields.

If for all particles the motion associated with each degree of freedom is independent of the other two, the 6D phase-space can be split up in three separate 2D phase-spaces, one for each degree of freedom. The area occupied by the projection of the phase-space density distribution onto one of the 2D phase-spaces is a measure for the beam quality in that dimension. Usually this is expressed in term of the emittance, as described in Sec. 2.1.

For the ideal case where the momenta of the electrons are linear functions of position the emittance is zero. However, when creating an electron bunch by photoemission the momentum distribution is uncorrelated, i.e., the electron bunch has a finite (effective) temperature. The bunch therefore has an initial or 'thermal' emittance, which is also treated in Sec. 2.1.

The remainder of this chapter is about the properties of a uniformly charged ellipsoidal electron bunch, also called 'waterbag' distribution. In Sec. 2.2 we present its space-charge fields, and we treat the dynamics and kinematics of a waterbag bunch. Then, in Sec. 2.3, we describe how such a bunch can be created in practice. Finally, in Sec. 2.4 we come to the conclusion that it is possible to realize a waterbag bunch with the parameters required for ultrafast electron diffraction.

2.1 Beam quality measure: emittance

2.1.1 Definition

A general figure of merit of the transverse beam quality is the transverse normalized root-mean-square (RMS) emittance, which is defined by

$$\varepsilon_{n,x} = \frac{1}{mc}\sqrt{\sigma_x^2\sigma_{p_x}^2 - cov^2(x, p_x)}, \tag{2.1}$$

with m the electron mass, c the speed of light, x the transverse position, and p_x the transverse momentum. The standard deviation is defined as usual by $\sigma_a \equiv \sqrt{<(a- <a>)^2>}$, where the brackets $<>$ indicate an average over the ensemble of electrons in the bunch. In the definition of emittance any correlation between x and p_x is canceled out by taking the covariance $cov(x, p_x) \equiv <(x- <x>)(p_x- <p_x>)>$ into account.

The transverse emittance in the y-direction and the longitudinal emittance in the z-direction are defined analogously. The product of these three emittances is a measure for the phase-space volume occupied by the bunch. Assuming that the motions in the x-, y-, and z-direction are completely decoupled, which is generally a reasonable assumption for freely propagating particle beams, Liouville's theorem states that the emittances are conserved quantities.

In practice the emittance is not measured in the phase-space, but in the so-called trace-space. This so-called geometrical emittance is given by

$$\varepsilon_x = \sqrt{\sigma_x\sigma_{x'} - cov^2(x, x')}, \tag{2.2}$$

with the paraxial angle given by $x' = \frac{dx}{dz}$. A paraxial approximation can be applied if the longitudinal velocity is much greater than the transverse velocities: v_x, $v_y \ll v_z$. Then $\beta_x = v_x/c \approx \beta\frac{v_x}{v_z} \approx \beta x'$ and, analogously, $\beta_y \approx \beta y'$, with $\beta \equiv \frac{v}{c} \approx \beta_z$. Substitution into Eq. (2.1) leads to the following equation for the normalized RMS emittance expressed in the trace-space quantities x and x':

$$\varepsilon_{n,x} = \sqrt{\sigma_x^2\sigma_{\gamma\beta x'}^2 - cov^2(x, \gamma\beta x')}, \tag{2.3}$$

with the Lorentz factor $\gamma \equiv (1-\beta^2)^{-1/2}$. In a beam waist, where the phase-space distribution is non-skewed, this general definition of emittance reduces to

$$\varepsilon_{n,x} = \gamma\beta\varepsilon_x; \tag{2.4a}$$

$$\varepsilon_{n,y} = \gamma\beta\varepsilon_y; \tag{2.4b}$$

$$\varepsilon_{n,z} = \sigma_z\sigma_{\gamma\beta} = \frac{1}{mc}\sigma_t\sigma_{\scriptscriptstyle U}, \tag{2.4c}$$

where U is the energy of an electron in the bunch. For a beam the energy of an electron is much larger than the energy spread, so that $\sigma_{\gamma\beta} \approx \left|\frac{\partial(\gamma\beta)}{\partial\gamma}\right|\sigma_\gamma = \frac{\sigma_\gamma}{\beta}$. Note that the geometrical emittance ε_x is not Lorentz invariant: it is a decreasing function of the energy, an effect which is called 'adiabatic damping'.

The emittance can be interpreted as a measure for the focusability of an electron beam. When realizing that the angular spread $\sigma_{x'}$ is maximally equal to unity, it is easy to see that a beam of given emittance $\varepsilon_{n,x}$ can be focused to a minimum spot size $\sigma_x \geq \frac{\varepsilon_{n,x}}{\gamma\beta}$, i.e., the value of the geometrical emittance. If smaller spot sizes have to be realized the emittance of the beam has to be decreased. A high-quality beam is thus characterized by small emittances.

2.1.2   Space-charge driven emittance growth

Due to Coulomb interactions between the charged particles in a bunch the emittance is likely to grow. It is straightforward to show that the time derivative of the emittance squared can be written as[1]

$$\frac{d}{dt}\varepsilon_{n,x}^2 = 2 \left| \begin{array}{cc} cov(x,x) & cov(x,eE_x) \\ cov(x,p_x) & cov(p_x,eE_x) \end{array} \right|, \tag{2.5}$$

where we have used the relations $\frac{dx}{dt} = \frac{p_x}{m}$, and $\frac{dp_x}{dt} = eE_x$, with e the elementary charge. The determinant in Eq. (2.5) equals zero only for the special case of a distribution, of which both the momentum $\vec{p}$ and the space-charge field $\vec{E}$ are linear functions of position $\vec{r}$. The only distribution with these ideal linear properties is the uniformly filled ellipsoidal bunch, also known as 'waterbag' bunch (see Sec. 2.2). For a waterbag bunch of zero temperature, and thus zero emittance, the emittance remains zero, even though strong space-charge fields are present.

2.1.3   Thermal emittance

In reality, the photoemitted electron bunch starts off with nonzero uncorrelated energy spread and angular spread, which can be described by a nonzero effective electron temperature. Therefore the bunch has a finite initial emittance, usually called 'thermal emittance' $\varepsilon_{n,th}$, given by

$$\varepsilon_{n,th} = \sigma_x \sqrt{\frac{k_{\mathrm{B}}T_e}{mc^2}}, \tag{2.6}$$

where k_{B} is Boltzmann's constant. The thermal emittance is the minimum possible emittance of a bunch with an effective temperature T_e that depends, among others, on the bandwidth of the photoemission laser, the Schottky effect, the cathode roughness, and the cathode impurity. In literature $\varepsilon_{n,x}^{th} = \sigma_x \cdot 8 \cdot 10^{-4}\,\mathrm{m}$ is reported [2] for bunches created in radio-frequency photoguns. This corresponds to $T_e = 0.33\,\mathrm{eV}$.

In bunches of nonzero temperature the correlations between the space-charge field and position, and between momentum and position are not perfectly linear. However, for a waterbag bunch with a thermal energy $U_{th} = k_{\mathrm{B}}T_e$ much smaller than the potential space-charge energy, the approximation of linear space-charge fields and linear momentum-position-correlations is still correct.

---

[1]The same equation holds for the y-, and z-direction.

2.2   Waterbag bunch: properties

As shown in Sec. 2.1.2 the emittance of space-charged dominated bunches is conserved only if the momenta and space-charge fields are linear functions of position. This is precisely the case for a uniformly charged ellipsoidal bunch, or 'waterbag' bunch, (with zero initial velocities in the bunch's rest frame). Moreover, such a bunch can be compressed reversibly in all three directions with linear electro-magnetic fields. The importance of linear space-charge fields in *beams* has already been recognized for a long time since the work of Kapchinski and Vladimirski. To create *bunches* with linear space-charge fields in all three directions Luiten *et al.* were the first to propose a practical method, see Ref. [3] and Sec. 2.3. Adopting this method Musumeci *et al.* have realized relativistic waterbag bunches for the first time [4]. In this section we present, for completeness, the well-known space-charge fields of waterbag bunches. We extend the earlier description of waterbags with closed expressions for the dynamics and kinematics.

2.2.1   Charge density profiles

The spatial distribution $\rho\left(\vec{r}\right)$ of an ellipsoidal bunch of uniform density ρ_0, also called 'waterbag' distribution, is given by:

$$\rho\left(\vec{r}\right) = \rho_0 \Theta\left(1 - \left(\frac{x}{A}\right)^2 - \left(\frac{y}{B}\right)^2 - \left(\frac{z}{C}\right)^2\right), \tag{2.7}$$

where A, B, and C are the semi-axes of the ellipsoid, and $\rho_0 = 3Q/(4\pi ABC)$ is the charge density. The function $\Theta(x)$ is the Heaviside step function, which is defined as

$$\Theta\left(x\right) = \begin{cases} 0 & \text{, if } x < 0 \\ 1 & \text{, if } x \geq 0. \end{cases} \tag{2.8}$$

The charge density of a waterbag bunch is by definition homogeneous. This implies that a fluid model is applied, which is a valid simplification for bunches with a high charge density. In Sec. 2.3 the validity of this simplification is discussed in some more detail.

When integrating Eq. (2.7) along one axis, e.g., the longitudinal direction as if the bunch were projected onto a phosphor screen, the density profile of the obtained 2D spot is given by

$$\sigma(x,y) = 2\rho_0 C \sqrt{1 - \left(\frac{x}{A}\right)^2 - \left(\frac{y}{B}\right)^2}. \tag{2.9}$$

Integrating this spot in a transverse direction, e.g., the y-direction, yields a parabolic line density profile

$$\Lambda(x) = \rho_0 \frac{\pi BC}{A^2}\left(A^2 - x^2\right). \tag{2.10}$$

Finally, integration of the line profile yields the charge Q of a waterbag bunch, which simply is the charge density times the volume of an ellipsoid:

$$Q = \rho_0 \frac{4\pi}{3} ABC. \tag{2.11}$$

2.2.2 Space-charge fields

Inside a uniformly filled spheroid (a cylindrically symmetric ellipsoid) with maximum radius $A = B = R$, and half-length $C = L$ the electrostatic potential $V(r,z)$ as a function of the radial coordinate $r = \sqrt{x^2 + y^2}$ and the longitudinal coordinate z is given by [5]

$$V(r,z) = \frac{\rho_0}{2\varepsilon_0} \left(MR^2 - M_r r^2 - M_z z^2 \right), \tag{2.12}$$

where $\rho_0 = (3Q)/(4\pi R^2 L)$ is the charge density (see Eq. (2.11)), and ε_0 is the permittivity of vacuum. In Eq. (2.12) the geometrical factors are given by [5]

$$M = \frac{\arctan(\Gamma)}{\Gamma}; \tag{2.13a}$$

$$M_r = \frac{1}{2} \left(1 - M_z \right); \tag{2.13b}$$

$$M_z = \frac{1 + \Gamma^2}{\Gamma^3} \left[\Gamma - \arctan\left(\Gamma \right) \right], \tag{2.13c}$$

with the eccentricity of the ellipsoid defined as $\Gamma \equiv \sqrt{R^2/L^2 - 1}$. Note that the eccentricity defined in this way is real for an oblate spheroid ($R > L$) and purely imaginary for a prolate spheroid ($R < L$). However M, M_r, and M_z are real-valued for both $R > L$ and $R < L$. The potential given by Eq. (2.12) is defined such that it equals zero if $R, L \to \infty$. Using $\vec{E} = -\vec{\nabla}V$ it follows immediately that the space-charge fields inside a uniformly charged ellipsoidal bunch are linear functions of position, given by

$$\vec{E}(r,z) = \frac{\rho_0}{\varepsilon_0} \left[M_r r \vec{e_r} + M_z z \vec{e_z} \right]. \tag{2.14}$$

For pancake-like bunches, i.e., bunches with $R \ggg L$, Eqs. (2.13b) and (2.13c) can be approximated by $M_r \approx \frac{L}{R} \frac{\pi}{4}$ and $M_z \approx 1$. The components of the space-charge field inside a thin spheroid thus reduce to

$$E_r(r) \approx \frac{3Q}{16\varepsilon_0 R^2} \frac{r}{R}; \tag{2.15a}$$

$$E_z(z) \approx \frac{3Q}{4\pi\varepsilon_0 R^2} \frac{z}{L}. \tag{2.15b}$$

2.2.3 Space-charge dynamics of waterbag bunches

Because of its linear space-charge fields an expanding uniformly charged ellipsoid will remain a uniform ellipsoid. The space-charge expansion is therefore completely described by simply tracking the evolution of the semi-axes A, B, and C in time. For a spheroid with radius R and

half-length L the expansion is exactly described by the following set of coupled differential equations:

$$\frac{d^2 R(t)}{dt^2} = \frac{eE_r(R,0)}{m} = \frac{e\rho_0}{2m\varepsilon_0} \left\{ 1 - \frac{1+\Gamma^2}{\Gamma^3} \left[\Gamma - \arctan(\Gamma) \right] \right\}; \qquad (2.16a)$$

$$\frac{d^2 L(t)}{dt^2} = \frac{eE_z(0,L)}{m} = \frac{e\rho_0}{m\varepsilon_0} \frac{1+\Gamma^2}{\Gamma^3} \left[\Gamma - \arctan(\Gamma) \right]. \qquad (2.16b)$$

Unfortunately, this set of differential equations cannot be solved analytically. However, as we will show below, a solution in closed form is possible when using the approximate space-charge fields given by Eqs. (2.15a) and (2.15b). Moreover, we will show that the resulting solution quite accurately describes the blow-out of a thin spheroid into a fully-fledged ellipsoid.

Inserting Eqs. (2.15a) and (2.15b) into Newton's law of motion leads to the following two coupled differential equations for the radius R and the half-length L of an expanding, initially thin, ellipsoid:

$$\frac{d^2 R(t)}{dt^2} = \frac{3Qe}{16m\varepsilon_0} \frac{1}{R^2(t)}; \qquad (2.17a)$$

$$\frac{d^2 L(t)}{dt^2} = \frac{3Qe}{4\pi m\varepsilon_0} \frac{1}{R^2(t)}, \qquad (2.17b)$$

Solving equation (2.17a) yields

$$R(t) = 2R_0 + \frac{2}{3}R_0\frac{t}{\tau} - R_0\left(1 + \frac{t}{\tau}\right)^{2/3}, \qquad (2.18)$$

with initial radius R_0, and the time constant $\tau = \sqrt{\frac{32m\varepsilon_0}{27Qe}R_0^3}$ (which can be seen as an inverse plasma frequency). The differential equation (2.17b) describing the longitudinal expansion cannot be solved analytically. However, when using the Taylor approximation $R(t) \approx R_0\left[1 + \frac{2}{9}\left(\frac{t}{\tau}\right)^2\right]$ an analytical solution is possible, yielding

$$L(t) = L_0 + \frac{3Qe}{4\pi m\varepsilon_0} \frac{3\sqrt{2}\tau}{4R_0^2} t \arctan\left(\frac{\sqrt{2}}{3}\frac{t}{\tau}\right), \qquad (2.19)$$

with L_0 the initial half-length of the bunch. In Figs. 2.1(a) and 2.1(b) the closed (analytical) expressions for $R(t)$ and $L(t)$, as given by Eqs. (2.18) and (2.19), are compared with the results of numerically integrating the set of coupled differential equations (2.16a) and (2.16b). For both the bunch radius and the bunch length the model governed by Eqs. (2.18) and (2.19) is in excellent agreement with the exact solution if $t \lesssim \tau$. The agreement is even reasonable for $t/\tau \gg 1$ where the aspect ratio of the bunch is close to 1, so strictly speaking the space-charge fields can no longer be approximated by those of a thin spheroid. However, because the expansion leads to lower space-charge fields, the dynamics are dominated by the behavior at $t \lesssim \tau$. For $t \gg \tau$ the deviation from the exact solution is about 5% for the radius and 20% for the length.

The space-charge-induced expansion of a spheroidal electron bunch ends up in a ballistic expansion with radial and longitudinal asymptotic velocities that can be calculated with Eqs. (2.18) and (2.19), yielding

$$v_{\mathrm{R},\infty} = \frac{2R_0}{3\tau} = \sqrt{\frac{3Qe}{8m\varepsilon_0 R_0}};$$ (2.20a)

$$v_{\mathrm{L},\infty} = \sqrt{2}\frac{R_0}{3\tau} = \sqrt{\frac{3Qe}{16m\varepsilon_0 R_0}}.$$ (2.20b)

It is concluded that the expansion of a thin spheroid into a fully-fledged 3D spheroid is reasonably well described by using the space-charge fields of a thin spheroid: equations (2.18) and (2.19) are powerful tools to estimate the dimensions of an expanding pancake bunch.
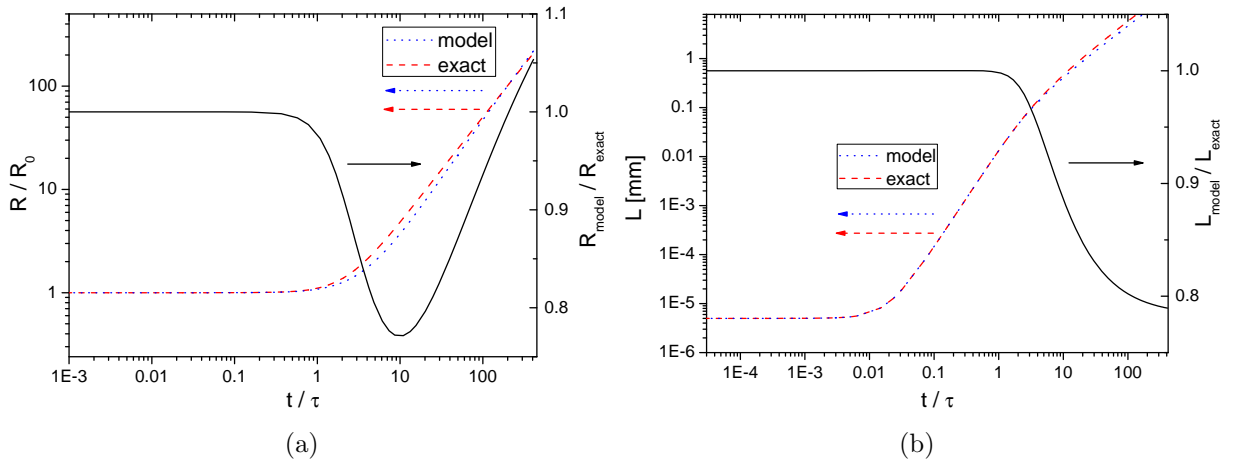
Figure 2.1: *Expansion of a* $0.1\,\mathrm{pC}$ *pancake bunch with initial radius* $R_0 = 100\,\mu\mathrm{m}$ *and initial half-length* $L_0 = 5\,\mathrm{nm}$. *(a) Bunch radius R (b) bunch half-length L as a function of* t/τ *according to Eqs. (2.18) and (2.19) (dotted lines), and as obtained by numerical integration of the coupled differential equations (2.16a) and (2.16b) (dashed lines). In both panels the solid line is the ratio of the approximate to the exact solution.*

2.2.4 Kinematics of waterbag bunches

Using Eq. (2.12) the potential energy U_p of a uniformly charged spheroidal bunch is readily calculated:

$$
\begin{aligned}
U_p &= \frac{1}{2} \int \rho_0 V(\vec{r}) \mathrm{d}^3 r \\
&= \pi \int_{-L}^{L} \mathrm{d}z \int_{0}^{R_0 \sqrt{1-z^2/L^2}} \rho_0 V(r,z) r \mathrm{d}r \\
&= \frac{3Q^2}{20\pi\varepsilon_0 L} \frac{\arctan(\Gamma)}{\Gamma}.
\end{aligned} \tag{2.21a}
$$

In the limit of a disk of zero thickness, i.e., $L \to 0$, the potential energy remains finite and is given by

$$
U_{p,disk} = \frac{3Q^2}{40\varepsilon_0 R_0}. \tag{2.22}
$$

If all particles in a uniformly charged ellipsoidal bunch start out with zero velocity, then the velocity distribution will become linearly chirped due to the linear space-charge fields, i.e., $\vec{v}(r,z) = \frac{r}{R}v_R\vec{e}_r + \frac{z}{L}v_L\vec{e}_z$, where the velocity parameters v_R and v_L depend on the initial charge density. In the bunch's rest frame the total kinetic energy U_k of all electrons in the bunch can be expressed in terms of the velocities v_R and v_L:

$$
\begin{aligned}
U_k &= \frac{m\rho_0}{2e} \int_{-L}^{L} \mathrm{d}z \int_{0}^{R\sqrt{1-z^2/L^2}} r\mathrm{d}r \int_{0}^{2\pi} |\vec{v}(r,z)|^2 \mathrm{d}\phi \\
&= \frac{Qm}{e} \left(\frac{1}{5}v_R^2 + \frac{1}{10}v_L^2 \right),
\end{aligned} \tag{2.23}
$$

When the bunch expansion has become ballistic the kinetic energy is readily calculated by inserting Eqs. (2.20a) and (2.20b) into Eq. (2.23):

$$
U_k = \frac{5}{4} \frac{3Q^2}{40\varepsilon_0 R_0}. \tag{2.24}
$$

Comparing this to the potential energy of a disk as given by Eq. (2.22) it is seen that, with the approximate asymptotic velocities obtained from dynamical theory, the kinetic energy of a ballistically expanding spheroid is overestimated by 25%.

Using the knowledge that $v_{R,\infty} \approx v_{z,\infty}$ an asymptotic expansion velocity can also be calculated from the kinematics presented in this section. Equating the potential energy of a disk to the kinetic energy of a ballistically expanding spheroid, and inserting $v_{R,\infty} = v_{z,\infty} = v_\infty$, yields

$$v_\infty = \sqrt{\frac{Qe}{4m\varepsilon_0 R_0}}, \qquad (2.25)$$

which is in between the results for $v_{\mathrm{R},\infty}$ and $v_{\mathrm{z},\infty}$ obtained in the previous section. As an illustration we calculate the value of v_∞ for a $0.1\,\mathrm{pC}$ pancake bunch with an initial radius of $100\,\mu\mathrm{m}$, resulting in $v_\infty = 2.2 \cdot 10^6\,\mathrm{m/s}$.

2.3   Waterbag bunch creation

In Ref. [3] Luiten *et al.* describe a practical way to realize a waterbag bunch by the space-charge induced blow-out of a thin sheet of electrons created by photoemission with a transversely shaped ultrashort laser pulse [3]. In this section we discuss in some more detail the conditions, as mentioned in Ref [3], for which the photoemitted sheet of electrons will develop into a waterbag bunch. Furthermore, we discuss the validity of the 'fluid' model that is used to calculate the space-charge fields and to describe the dynamics of an electron bunch.

In theoretical astrophysics it has been realized already for some time that a uniform prolate spheroid will collapse under its own weight into a flat disk, i.e., an oblate spheroid with $L = 0$ [6]. This collapse is the time-reversed analogue of the explosion of an electron bunch, because the driving force (gravitation) has the same $\propto 1/r^2$ dependency as the Coulomb force, but with opposite direction. The density distribution $\rho(r,z)$ of the flat disk (after the collapse) is given by

$$\rho(r,z) = \sigma_0 \sqrt{1 - (r/R)^2}\,\delta(z), \qquad (2.26)$$

where $\sigma_0 = 3Q/(4\pi R^2)$ is the surface charge density at the center, and $r = \sqrt{x^2 + y^2}$. Reversing this collapsing process implies that an ultrathin sheet of electrons with a charge density distribution as given by Eq. (2.26) will evolve into a uniformly charged spheroid. However, it is obvious that an infinitely thin flat disk (a 2D body) will not evolve into any 3D body. So it is not completely true that the evolution of an ultrathin sheet of electrons can be seen as the reverse of the collapse process. Contrary to the flat disk the ultrathin sheet has a small, but finite thickness. Furthermore, the sheet is created in time by photoemission from a metal surface. This has four consequences:

1. The initial charge density distribution does not fulfill Eq. (2.26): the Dirac delta function $\delta(z)$ has to be replaced by a realistic initial longitudinal distribution function $\lambda_n(z)$.

2. The front side of the ultrathin sheet is created earlier than the back side.

3. Image charge forces are counteracting the acceleration field during initiation of the bunch.

4. Under certain conditions the granularity of the bunch becomes apparent, leading to a different longitudinal space-charge field than calculated with a fluid model.

17
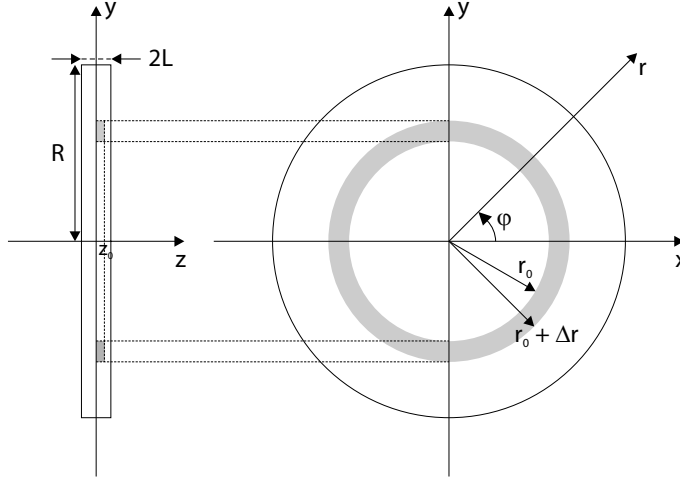
Figure 2.2: *Side view and front view of a pancake bunch in a polar coordinate system. The pancake bunch has radius a R and length $2L$. The gray parts of the bunch indicate the volume to which Gauss's law is applied to calculate the electric field at a point (r_0, z_0) inside the bunch.*

In the following these four points are examined in more detail.

Longitudinal charge density function
A pancake electron bunch is a bunch with an aspect ratio $L/R \ll 1$. Figure 2.2 shows a schematic of a pancake bunch in a polar coordinate system.

The radial component of the space-charge field inside a pancake bunch is in good approximation given by by Eq. (2.15a). However, since $\lambda_n(z)$ is not known exactly, the shape of the longitudinal component is not a priori clear. It can be estimated as follows. Suppose the bunch has a cylindrically symmetric charge density distribution $\rho(r, z)$. Assume that this can be written as the product of a surface charge density $\sigma(r)$ distribution and a longitudinal distribution function $\lambda_n(z)$: $\rho(r, z) = \sigma(r)\lambda_n(z)$. The longitudinal distribution is symmetrical in the plane $z = 0$ and is normalized to unity $\int_{-\infty}^{\infty} \lambda_n(z)dz = 1$, but otherwise arbitrary. To calculate the electric field at a point (r_0, z_0) inside the bunch, Gauss's law is applied to a volume bounded by $0 \le z \le z_0$, $r_0 \le r \le r_0 + \Delta r$, and $0 \le \varphi \le 2\pi$ as depicted in Fig. 2.2, resulting in the following equation:

$$\pi E_z \left[(r_0 + \Delta r)^2 - r_0^2 \right] + 2\pi E_r \left[(r_0 + \Delta r) - r_0 \right] z_0 = \frac{2\pi}{\varepsilon_0} \int_{r_0}^{r_0 + \Delta r} r\sigma(r)dr \int_0^{z_0} \lambda_n(z)dz. \quad (2.27)$$

Expanding Eq. (2.27) up to first order in $\Delta r/r_0$ (and dividing by 2π), results in

$$E_z + E_r \left(\frac{z_0}{r_0} \right) \approx \frac{1}{\varepsilon_0} \sigma(r_0) \int_0^{z_0} \lambda_n(z)dz. \quad (2.28)$$

From Eqs. (2.15a) and (2.15b) it follows that, for an thin oblate spheroid, $\frac{E_z}{E_r}\frac{r_0}{z_0} \approx \frac{R}{L}$. It is therefore reasonable to assume $E_z \gg E_r z_0/r_0$, resulting in the following approximation for the longitudinal component of the electric field inside a pancake bunch:

$$E_z(r, z) \approx \frac{\sigma(r)}{\varepsilon_0} \int_0^z \lambda_n(r, z')dz'. \tag{2.29}$$

Because the longitudinal space-charge field E_z inside a pancake bunch is proportional to the *integrated* longitudinal distribution, E_z is independent of the detailed shape of $\lambda_n(z)$ [3]. As a result, an electron inside a pancake bunch experiences the same acceleration as if it were part of the ideal charge density distribution described by Eq. (2.7), with $A = B = R \gg C = L$. To realize this charge density distribution the intensity profile of the laser pulse has to be shaped only transversely; the temporal shape is arbitrary. How the required transverse pulse shape can be obtained, is explained in Sec. 4.1.3.

Finite creation time

Because some electrons are photoemitted earlier than others (because of the finite laser pulse duration) the velocities of the first electrons increase during the photoemission process. This is leading to longitudinal velocity-position correlations associated with the laser pulse duration τ_l. But the idea of the waterbag concept is that velocity-position correlations are associated with, and only with, the space-charge fields. The photoemission process can be considered as being instantaneous, and thus negligible, if the laser pulse length is much shorter than the final bunch length:

$$\tau_l \ll t_b(\gamma) = t_{b,\infty} \sqrt{\frac{\gamma - 1}{\gamma + 1}}, \tag{2.30}$$

where t_b is expressed in terms of the Lorentz factor $\gamma = 1 + \frac{eE_{acc}z}{mc^2}$, and the asymptotic bunch duration $t_{b,\infty}$ is given by [7]

$$t_{b,\infty} = \frac{mc\sigma_0}{e\varepsilon_0 E_{acc}^2}, \tag{2.31}$$

with σ_0 the surface charge density, and E_{acc} the strength of a uniform acceleration field. For a bunch that is accelerated to a final energy of $100\,\text{keV}$ the Lorentz factor $\gamma = 1.2$, and Eq. (2.30) yields

$$\tau_l \ll 0.4 t_{b,\infty} = 0.4 \frac{mc\sigma_0}{e\varepsilon_0 E_{acc}^2}. \tag{2.32}$$

Image charge

The image charge fields exert a force on the electrons back towards the cathode. This causes undesired longitudinal velocity-position correlations, that can be neglected if the acceleration field E_{acc} is much stronger then the image-charge field $E_{im} \approx \sigma_0/\varepsilon_0$ [7]. This gives rise to a lower limit of the acceleration field strength according to

$$E_{acc} \gg \frac{\sigma_0}{\varepsilon_0}. \tag{2.33}$$

Combining the conditions on the laser pulse duration (Eq. (2.32)) and the image charge (Eq. (2.33)) yields

$$\frac{eE_{acc}\tau_l}{0.4mc} \ll \frac{\sigma_0}{\varepsilon_0 E_{acc}} \ll 1. \tag{2.34}$$

These two conditions are leading to constraints on the part of the parameter space (σ_0, E_{acc}) for which a pancake bunch will evolve into a waterbag bunch. This so-called 'waterbag existence regime' is visualized in Fig. 2.3. In this figure the laser pulse length has been chosen to be 30 fs. The solid black lines in Fig. 2.3 represent the case of equalities in Eq. (2.34). For the inner green triangle the inequalities are replaced by < 0.1, as indicated in Fig. 2.3. To find out what factor should really be taken for the $\ll$ symbols, particle tracking simulations and/or experiments have to be performed. Results of simulations are shown in Ref. [8], and preliminary experiments are presented in Ch. 8 in this thesis.
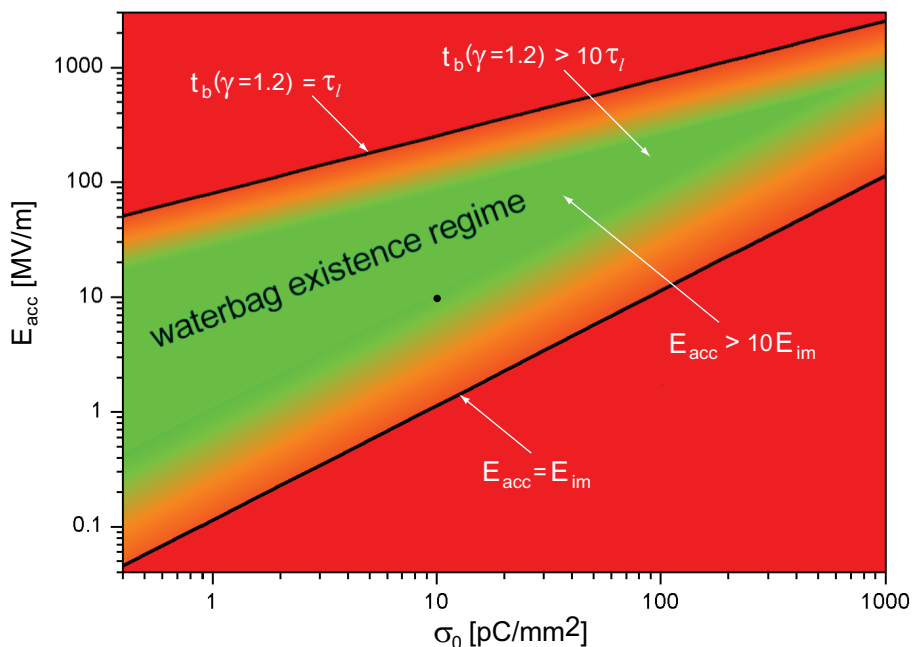
Figure 2.3: *Parameter space (σ_0, E_{acc}) in which a pancake electron bunch will develop into a waterbag bunch if the initial charge density distribution fulfills Eq. (2.26). The laser pulse length has been chosen to be 30 fs. The dot indicates the parameters to create an electron bunch suitable for single-shot ultrafast electron diffraction, as achieved in this thesis.*

Granularity

Generally an electron bunch is considered as a continuous charge distribution and a 'fluid' model is applied to calculate space-charge fields and dynamical behavior. However, because electrons are point particles, the assumption of a fluid model is not obvious. In the following we discuss the conditions for which the fluid model applies.

Consider an electron positioned at relative coordinates $r = r_0$ and $z = z_0$ with respect to another electron, as illustrated in Fig. 2.4. The longitudinal component of the Coulomb
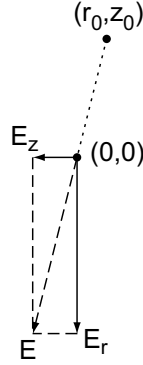
Figure 2.4: *Schematic of the radial component E_r and the longitudinal component E_z of the Coulomb field of an electron at relative coordinates $r = r_0$ and $z = z_0$ with respect to another electron.*

field at the position of either electron is

$$E_z = \frac{e}{4\pi\varepsilon_0} \frac{z_0}{(z_0^2 + r_0^2)^{3/2}} \tag{2.35a}$$

$$\approx \frac{e}{4\pi\varepsilon_0} \frac{z_0}{r_0^3}, \tag{2.35b}$$

where the approximation holds if $z_0 \gg r_0$. In a high aspect ratio ($R \gg L$) bunch only the nearest electrons (at small r_0) contribute considerably to the longitudinal space-charge field at a certain position. Therefore it is expected that the granular nature of the bunch shows up if $< r_0 > \gtrsim z_0$, where $< r_0 > = R\sqrt{N}$ is the average radial distance between two electrons in a bunch that contains N electrons. Maximizing z_0 by using $z_0 = 2L$ it follows that the 'fluid' model is valid if

$$N = Q/e \gtrsim \left(\frac{R}{L}\right)^2. \tag{2.36}$$

In the experiments described in this thesis, at the time of photoemission bunches are created with typically $R = 100\,\mu$m, $2L = 10$ nm, and $Q = 0.1$ pC, i.e., $< r_0 > \approx 130$ nm $\gg$ z_0. These bunches do not fulfill the condition expressed by Eq. (2.36), and consequently the longitudinal space-charge field differs strongly from the expected field based on the fluid model. This is illustrated in Fig. 2.5 where the longitudinal space-charge fields of a zero-temperature, thin spheroid are depicted, as calculated with GPT [?] using a point-to-point method and a particle-in-cell (i.e., fluid) method. Clearly there is a striking difference between the magnitude, especially at the bunch extremities, and the smoothness of the field.

Surprisingly however, the fluid space-charge model seems to describe the bunch evolution accurately. When studying the dynamics of an electron bunch created by photoemission, the finite effective temperature has to be taken into account, which is $T_e \approx 0.33$ eV (see Sec. 2.1.3). This is comparable to the work done by the acceleration field during the photoemission process: $W_{field} = E_{acc}2L = 10\,$MV/m $\cdot$ 10 nm $= 0.1$ eV. Therefore, the thermal velocities cannot be neglected. As a matter of fact, it is just because of these thermal velocities that the

bunch expands rapidly to the regime where the fluid model is valid, i.e., the bunch quickly expands to a length $2L \gtrsim R/\sqrt{N} \approx 100\,\text{nm}$ (for $R = 100\,\mu\text{m}$ and $Q = 0.1\,\text{pC}$). This is confirmed by GPT simulations of the dynamics of an electron bunch in the setup as described in Sec. 3.3. The macroscopic bunch parameters (radius, length, emittances) at time scales $t \gg \tau_l$ are independent of the choice of the space-charge model, i.e., the point-to-point method or the particle-in-cell method [9]. It is concluded that, although the fluid model is fundamentally wrong, it properly describes the space-charge blow-out of a pancake electron bunch.
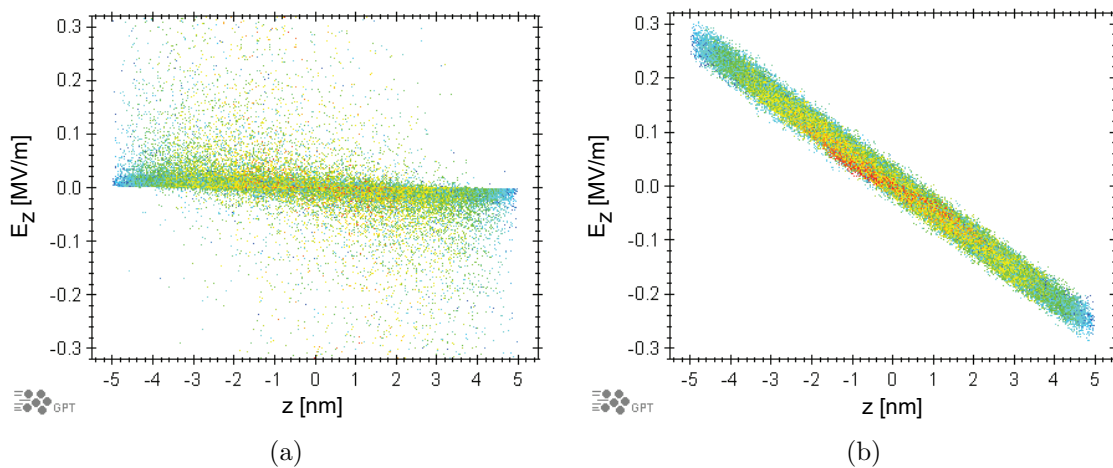
Figure 2.5: GPT *simulations of the longitudinal space-charge field E_z as a function of position z in the bunch, as calculated with (a) a point-to-point method, and (b) a particle-in-cell method. The bunch is a $T_e = 0$, $Q = 0.1\,\text{pC}$ spheroid with radius $R = 100\,\mu\text{m}$ and length $2L = 10\,\text{nm}$. Particles at larger radii are colored red, particles at smaller radii are colored blue.*

2.4 Conclusions

The emittance of a uniformly charged ellipsoidal bunch (or 'waterbag' bunch) is not spoiled by its own space-charge fields: because of the linear space-charge fields the velocity chirp will also be linear. This enables one to focus such a bunch in all three dimensions with linear electro-magnetic fields.

A waterbag bunch can be created by the blow-out of a pancake electron bunch with a charge density distribution $\rho(r, z) = \sigma_0\sqrt{1 - (r/A)^2}\lambda_n(z)$, if the two conditions given by Eqs. (2.30) and (2.33) are satisfied.

As indicated by the dot in Fig. 2.3 a 0.1 pC waterbag bunch with an initial bunch radius[2] of $50\,\mu\text{m}$ can be realized in an acceleration field of $10\,\text{MV/m}$. If such a bunch can be compressed to a duration less than 100 fs and focused to a width of about $100\,\mu\text{m}$, then

---

[2]This radius is required in order to have an emittance low enough for a diffraction experiment, as explained in Sec. 6.2.

a bunch would have been realized that is ideal to examine ultrafast processes with electron diffraction. An acceleration field $E_{acc} = 10\,\mathrm{MV/m}$ can be realized relatively easily in a DC photogun.

References

[1] C. Lejeune, and J. Aubert, Emittance and brightness: definitions and measurements, in *Applied Charged Particle Optics*, edited by A. Septier, Academic Press, 1980.

[2] Ph. Piot, Review of experimental results on high-brightness photo-emission electron sources, in *The Physics and Applications of High Brightness Electron Beams*, edited by J. Rosenzweig, G. Travish, and L. Serafini, page 127, 2002.

[3] O. J. Luiten, S. B. van der Geer, M. J. de Loos, F. B. Kiewiet, and M. J. van der Wiel, Phys. Rev. Let. **93**, 094802 (2004).

[4] P. Musumeci, J. T. Moody, R. J. England, J. B. Rosenzweig, and T. Tran, Phys. Rev. Lett. **100**, 244801 (2008).

[5] E. Durand, *Électrostatique, Tome 1: Les Distributions*, Masson et Cie, Paris, 1964.

[6] C. C. Lin et al., Astrophysics Journal **142**, 1431 (1965).

[7] O. J. Luiten, Beyond the rf photogun, in *The Physics and Applications of High Brightness Electron Beams*, edited by J. Rosenzweig, G. Travish, and L. Serafini, page 108, 2002.

[8] T. van Oudheusden, Dream beam, from pancake to waterbag, Master thesis, Technische Universiteit Eindhoven, 2006.

[9] M. J. de Loos, S. B. van der Geer, T. van Oudheusden, O. J. Luiten, and M. J. van der Wiel, Barnes & Hut tree code versus particle-in-cell, in *Proceedings of the 19th Symposium on Plasma Physics and Radiation Technology, Lunteren*, page A26, 2007.

3

Electron source concept for single-shot sub-$100\,\mathrm{fs}$ electron diffraction in the $100\,\mathrm{keV}$ range

Abstract. We present a method for producing sub-100 fs electron bunches that are suitable for single-shot ultrafast electron diffraction experiments in the 100 keV energy range. A combination of analytical estimates and state-of-the-art particle tracking simulations based on a realistic setup show that it is possible to create 100 keV, 0.1 pC, 20 fs electron bunches with a spotsize smaller than $500\,\mu$m and a transverse coherence length of 3 nm, using established technologies in a table-top setup. The system operates in the space-charge-dominated regime to produce energy-correlated bunches that are recompressed by radio-frequency techniques. With this approach we overcome the Coulomb expansion of the bunch, providing a single-shot, ultrafast electron diffraction source concept.

3.1   Introduction

The development of a general experimental method for the determination of non-equilibrium structures at the atomic level and femtosecond timescale would provide an extraordinary new window on the microscopic world. Such a method opens up the possibility of making 'molecular movies' which show the sequence of atomic configurations between reactant and product during bond-making and bond-breaking events. The observation of such transition states structures has been called one of the holy-grails of chemistry, but is equally important for biology and condensed matter physics [1, 2, 3].

There are two promising approaches for complete structural characterization on short timescales: ultrafast X-ray diffraction and ultrafast electron diffraction (UED). These methods use a stroboscopic -but so far multi-shot- approach that can capture the atomic structure of matter at an instant in time. Typically, dynamics are initiated with an ultrashort (pump) light pulse and then -at various delay times- the sample is probed in transmission or reflection with an ultrashort electron [4, 5] or X-ray pulse [6]. By recording diffraction patterns

as a function of the pump-probe delay it is possible to follow various aspects of the real-space atomic configuration of the sample as it evolves. Temporal resolution is fundamentally limited by the X-ray/electron pulse duration, while structural sensitivity depends on source properties like the beam brightness and the nature of the samples.

Electron diffraction has some unique advantages compared with X-ray techniques [7]: (1) UED experiments are table-top scale; (2) the energy deposited per elastic scattering event is about 1000 times lower compared to 1.5 Å X-rays; (3) for most samples the scattering length of electrons better matches the optical penetration depth of the pump laser. However, until recently femtosecond electron diffraction experiments had been considered unlikely. It was thought that the strong Coulombic repulsion (space-charge) present inside of high-charge-density electron bunches produced through photoemission with femtosecond lasers, fundamentally limited this technique to picosecond timescales and longer. Several recent developments, however, have resulted in a change of outlook. Three approaches to circumvent the space-charge problem have been attempted by several groups. The traditional way is to accelerate the bunch to relativistic energies to effectively damp the Coulomb repulsion. Bunches of several hundred femtosecond duration containing high charges (several pC) are routinely available from radio-frequency (RF) photoguns. The application of such a device in an electron diffraction experiment was recently demonstrated [8]. This is an exciting development; however, energies in the MeV range pose their own difficulties, including the very short De Broglie wavelength ($\lambda \approx 0.002$ Å at 5 MeV), radiation damage to samples, reduced cross-section for elastic scattering, non-standard detectors and general expense of the technology. Due to these and other considerations, electron crystallographers prefer to work in the $100 - 300$ keV range.

A second avenue to avoid the space-charge expansion is by reducing the charge of a bunch to approximately one electron, while increasing the repetition frequency to several MHz [9]. The temporal resolution is then determined by the jitter in the arrival time of the individual electrons at the sample. According to reference [10] simulations show that, by minimizing the jitter of the RF acceleration field, the individual electrons could arrive at the sample within a time-window of several fs (possibly even sub-fs). This technique, however, requires that the sample be reproducibly pumped and probed $\sim 10^6$ times to obtain diffraction patterns of sufficient quality.

Third, compact electron sources have been engineered to operate in a regime where space-charge broadening of the electron bunch is limited. The current state-of-the-art compact electron gun provides ~ 300 fs electron bunches, containing several thousand electrons per bunch at sub-100 keV energies and with a beam divergence in the mrad range [11, 12]. This source represents a considerable technical achievement, but is still limited by space-charge effects which limit the number of electrons to less than 10000 per bunch for applications requiring high temporal resolution. In comparison to that source our proposed concept increases the temporal resolution by one order of magnitude and the number of electrons per bunch by two orders of magnitude, thereby making single-shot UED possible.

The ideal source for single-shot transmission ultrafast electron diffraction (UED) experiments would operate at (several) 100 keV energies, providing bunches shorter than 100 fs, containing $\gtrsim 10^6$ electrons. The transverse coherence length $L_\perp$ should be at least a few nanometers -or several unit cell dimension- to ensure high-quality diffraction data. None of

the electron source concepts presently in use is able to *combine* these bunch requirements. Herein we present an electron source concept for UED experiments, based on linear space-charge expansion of the electron bunch [13] and RF compression strategies energies [14], that is able to obtain the ideal parameters presented above with potential well beyond these numbers.

The message of this paper is twofold. (1) We show on the basis of fundamental beam dynamics arguments and analytical estimations that single-shot, sub-100 fs UED in the 100 keV energy range is *in principle* possible. (2) To show that it can be realized *in practice* we have performed detailed particle tracking simulations of a realistic setup which confirm the analytical results.

The remainder of this paper is organized as follows. In Sec. 3.2 we discuss the beam dynamics of single-shot UED and show that the bunch requirements for single-shot UED can only be reached by operating close to fundamental space-charge limits. The high space-charge density inevitably leads to a fast Coulomb expansion, which needs to be reversed both in the longitudinal and the transverse direction. This can be accomplished with ellipsoidal bunches [13]. In particular we show how the longitudinal expansion can be reversed using the time-dependent electric field of a cylindrical RF cavity resonating in the TM_{010} mode. The beam dynamics discussion and analytical estimates very naturally lead to a setup, which is described in Sec. 3.3. The diode structure of the accelerator, and the RF cavity for bunch compression are described in some detail. Then, in section Sec. 3.4 we present the results of our particle tracking simulations, which confirm the analytical estimates and which convincingly show that single-shot, sub 100-fs electron diffraction at 100 keV is feasible. In Sec. 3.5 the stability of the setup is discussed. Finally, in Sec. 3.6, we draw our conclusions.

3.2 Single-shot UED beam dynamics

3.2.1 General considerations

The transverse coherence length $L_\perp$ is an important beam parameter in electron diffraction experiments. It is defined as follows in terms of the De Broglie wavelength λ and root-mean-square (RMS) angular spread σ_θ:

$$L_\perp \equiv \frac{\lambda}{2\pi\sigma_\theta}. \tag{3.1}$$

However, a more general figure of merit of the transverse beam quality, familiar to electron beam physicists, is expressed in terms of the transverse normalized emittance $\varepsilon_{n,x}$, as defined by Eq. (2.1). In a beam waist Eq. (2.1) reduces to $\varepsilon_{n,x} = \frac{1}{mc}\sigma_x\sigma_{p_x}$, where σ_x is the RMS bunch radius, and σ_{p_x} the RMS transverse momentum spread. The transverse coherence length at a beam waist, in particular in a beam focus, is therefore given by

$$L_\perp = \frac{\hbar}{mc}\frac{\sigma_x}{\varepsilon_{n,x}}, \tag{3.2}$$

where $\hbar$ is Planck's constant. When aiming for $L_\perp \geq 4\,\text{nm}$ and $\sigma_x \leq 0.2\,\text{mm}$ at the sample, which is placed in the focus of the beam, then it necessarily follows that $\varepsilon_{n,x} \leq 20\,\text{nm}$ in order

to obtain a diffraction pattern of sufficient quality. Moreover, recording a diffraction pattern in a single shot requires a bunch charge of least $0.1\,\mathrm{pC}$. Such low-emittance, highly charged, ultrashort bunches can only be created by pulsed photoemission [15]. The initial transverse emittance for pulsed photoemission from metal cathodes is $\varepsilon_{i,x} = 8 \times 10^{-4}\sigma_x$ [15], so that the initial RMS radius σ_x at the photocathode may not be larger than $25\,\mu\mathrm{m}$. Extracting a charge $Q = 0.1\,\mathrm{pC}$ in an ultrashort pulse from such a small spot leads to an image-charge density $\frac{Q}{2\pi\sigma_x^2}$ and therefore to an image-charge field $E_{im} = \frac{Q}{4\pi\varepsilon_0\sigma_x^2} \approx 1\,\mathrm{MV/m}$ [16], where ε_0 is the permittivity of vacuum. Acceleration of the bunch requires the acceleration field to be substantially higher, i.e., about $10\,\mathrm{MV/m}$.

The space-charge fields inside the bunch are of the same order of magnitude as the image-charge fields, resulting in a rapid expansion of the bunch to millimeter sizes within a nanosecond, as will be shown in the next section.

Up to now such a space-charge explosion was considered unavoidable, and strategies were developed aiming at minimizing this effect either by setting an upper limit to the charge of a bunch [7, 17] or by accelerating the bunch to relativistic velocities [8]. In this article however, we show that the space-charge expansion is not necessarily a problem, provided that the expansion results in a bunch with a linear velocity-position correlation.

3.2.2   Expansion and compression of ellipsoidal bunches

To be able to compress an electron bunch, both transversely *and* longitudinally, to the required dimensions while conserving its emittance, it is necessary that the rapid space-charge induced expansion is reversible; i.e., the space-charge fields must be linear, which is precisely the case for a homogeneously charged ellipsoidal bunch [18]. Such a bunch can actually be created in practice by femtosecond photoemission with a 'half-circular' radial laser profile (see Sec. 2.3 and Ref. [13]). The expansion in the transverse direction can be reversed by regular charged-particle optics, such as magnetic solenoid lenses. The reversal of the expansion in the longitudinal direction, i.e., bunch compression, is less straightforward. Several methods have been developed for relativistic accelerators, employing either constant magnetic fields [19] or time-dependent electric fields [14].

In this article we propose to use the time-dependent axial electric field of a cylindrical $3\,\mathrm{GHz}$ RF cavity oscillating in the TM_{010} mode. The idea is to apply a ramped electric field, such that the front particles, which move the fastest, are decelerated while the slower electrons at the rear of the bunch are accelerated, leading to ballistic compression in the subsequent drift space. The field ramp needs to be timed very accurately, since it has to coincide with the picosecond bunch. This can be realized by using an RF field, whose phase can be synchronized to the femtosecond photoemission laser pulse with an accuracy better than $50\,\mathrm{fs}$ [20].

We start by looking into the expansion of an ellipsoidal bunch. As shown in Sec. 2.2.2 the space-charge fields inside a uniformly filled spheroid (a cylindrically symmetric ellipsoid) are linear functions of position. As a consequence the particle velocities are also linear functions of position. The space-charge fields of a uniform ellipsoidal bunch thus lead to a linear expansion, with the result that the uniform ellipsoidal -and thus linear- character of the bunch is maintained. In our approach we initiate the bunch by pulsed photoemission

with a femtosecond laser pulse with a 'half-circular' transverse intensity profile as given by $I(r) = \sqrt{1 - (r/R)^2}$. As shown in Ref. [13] this is essentially equivalent to starting out with a flat, pancake-like spheroid ($L \ll R$). During the subsequent acceleration this pancake bunch automatically evolves into a 3-dimensional, hard-edged uniform spheroid as explained in Sec. 2.3. The space-charge-induced expansion of the bunch ends up in a ballistic expansion with an asymptotic velocity v_∞ given by Eq. (2.25). For a 0.1 pC bunch of 50 μm radius this results in $v_\infty = 3.2 \times 10^6$ m/s.

Interestingly, the value of the space-charge-induced asymptotic velocity difference $2v_\infty$ is not equal to the final longitudinal velocity difference $2v_L$ after the bunch has left the acceleration field. Due to the fact that the slower electrons at the back of the bunch spend a longer time in the acceleration field than the electrons at the front of the bunch, the electrons at the back gain additional momentum from the acceleration field. In this way the space-charge-induced velocity difference $2v_\infty$ is reduced by the 'longitudinal exit kick' of the acceleration field. Suppose the space-charge expansion is completed in a very short time, i.e., the asymptotic velocity difference $2v_\infty$ is reached after a distance the bunch has traveled much smaller than the acceleration gap. In a uniform acceleration field E_{acc} the bunch duration t_b at the end of the diode is then $t_b = \frac{2mv_\infty}{eE_{acc}}$, which implies that the particles at the back of the bunch acquire an additional momentum $p_{kick} = eE_{acc}t_b = 2mv_\infty$, canceling the space-charge-induced expansion speed. In reality however, this cancelation is not complete, since we have neglected the finite time it takes to complete the space-charge expansion. But clearly the asymptotic velocity difference $2v_\infty$ is reduced substantially due to the longitudinal exit kick of the diode.

Now that we have described the expansion dynamics of an ellipsoidal bunch, let us take a look at the compression of the bunch. Suppose the RF cavity has reversed the longitudinal velocity-position correlation, so that it is now given by $v_z = -\frac{z}{L}v_L$. Using the same energy conversion considerations as for the expansion case (see Sec. 2.2.4) we now estimate the required velocity difference $2v_L$ for ballistic compression of the bunch. Assume that the potential energy of the expanded bunch is much smaller than its kinetic energy, i.e., $U_p \ll U_k$. Furthermore, it is assumed that the beam has been collimated. The bunch thus has a linear velocity-position correlation with the transverse expansion speed much smaller than the longitudinal one: $v_R \ll v_L$. At the time-focus the bunch has reached its shortest possible length and $v_L = 0$: all kinetic energy has been converted into potential energy. With Eqs. (2.22) and (2.23) it can then be calculated that for an ellipsoidal bunch with charge $Q = 0.1$ pC and radius $R \approx 2\sigma_x = 400$ μm the required velocity difference for this ballistic compression is $2v_L = 3.9 \times 10^6$ m/s, which can be induced by the on-axis electric field component of a TM_{010} cavity. To calculate the momentum difference $\Delta p_{z,bunch}$ that the RF field introduces between the most outward electrons of a bunch, we first have a look at the momentum change $\Delta p_{z,1}$ of a *single electron*. Assuming that the velocity change due to the RF field is so small that the resulting change in the transit times through the RF cavity is negligible, the following equation holds

$$\Delta p_{z,1} = - \int_{t_1}^{t_1+d_{cav}/v_c} eE(t)\mathrm{d}t$$

$$= \frac{2eE_0}{\omega} \sin\left(\frac{\omega d_{cav}}{2v_c}\right) \sin\left(\varphi_0\right), \tag{3.3}$$

$$\tag{3.4}$$

where v_c is the velocity of the electron when it enters the cavity, and the electric field $E(t) = E_0 \sin(\omega t - \frac{\omega d_{cav}}{2v_c} + \varphi_0)$, with amplitude E_0, and angular frequency ω. The phase offset φ_0 is such that if $\varphi_0 = 0$ the electron will have no net momentum change after the RF cavity. If the phase offset $\varphi_c = \varphi_0$ for the center electron of a bunch of length $2L$, then the phase offset for an electron at the front of the bunch $\varphi_{front} = \varphi_0 - \omega L/v_c$ and for an electron at the back $\varphi_{back} = \varphi_0 - \omega L/v_c$. Subtraction of the momentum change of the front electron from the momentum change of the back electron yields

$$\Delta p_{z,bunch} = \frac{4eE_0}{\omega} \sin\left(\frac{\omega d_{cav}}{2v_c}\right) \sin\left(\frac{\omega L}{v_c}\right) \cos\left(\varphi_0\right). \tag{3.5}$$

Assuming that the transit time of an electron trough the cavity is much smaller than the time period of the RF field, i.e., $\omega d_{cav}/(2v_c) \ll 1$, and that the bunch duration $t_b = 2L/v_c$ at the moment of injection into the cavity is much shorter than the time period, i.e., $\omega L/v_c \ll 1$, Eq. (3.5) reduces to

$$\Delta p_{z,bunch} = \frac{eE_0\omega d_{cav}t_b}{v_c} \cos\left(\varphi_0\right). \tag{3.6}$$

From Eq. (3.6) it follows that the longitudinal momentum RF kick that is required for ballistic compression of a $100\,\mathrm{keV}$ bunch with duration $t_b = 3\,\mathrm{ps}$ can be realized by an RF field with amplitude $E_0 = 6.5\,\mathrm{MV/m}$ (if $\varphi_0 = 0$), in a cavity with resonant frequency $f = \frac{\omega}{2\pi} = 3\,\mathrm{GHz}$ and a length $d_{cav} = 1\,\mathrm{cm}$.

3.3 Single-shot UED setup

3.3.1 Overview

As an implementation of the ideas presented in Sec. 3.2, we propose a table-top UED setup as shown in Fig. 3.1(a), consisting of a DC photogun, two solenoidal magnetic lenses $S1$ and $S2$, and a RF cavity. The bucking coil is to null the magnetic field at the cathode surface. Electrons are liberated from a metal photocathode by a transversely shaped, ultrashort laser pulse (see Sec. 4.1.3) and accelerated through a diode structure to an energy of $100\,\mathrm{keV}$ (see Sec. 4.2). By applying a DC voltage of $100\,\mathrm{kV}$ between the cathode and the anode an acceleration field of $10\,\mathrm{MV/m}$ is obtained. Because of the linear space-charge fields the photoemitted bunch evolves such that its phase-space distribution becomes linearly chirped

with faster electrons towards the front and slower electrons towards the back. This is indicated in Fig. 3.1(c) by the schematic longitudinal phase-space distribution, i.e., longitudinal momentum p_z versus position z in the bunch. The electric field oscillating in the TM_{010} mode in the RF cavity either accelerates or decelerates electrons passing through along the axis, depending on the RF phase. By injecting a bunch just before the field goes through zero, the front electrons are decelerated and the back electrons are accelerated. In this way the longitudinal velocity-correlation in the bunch is reversed. To illustrate this scheme Fig. 3.1(c) shows the longitudinal phase-space distribution of the bunch at several key points in the setup.
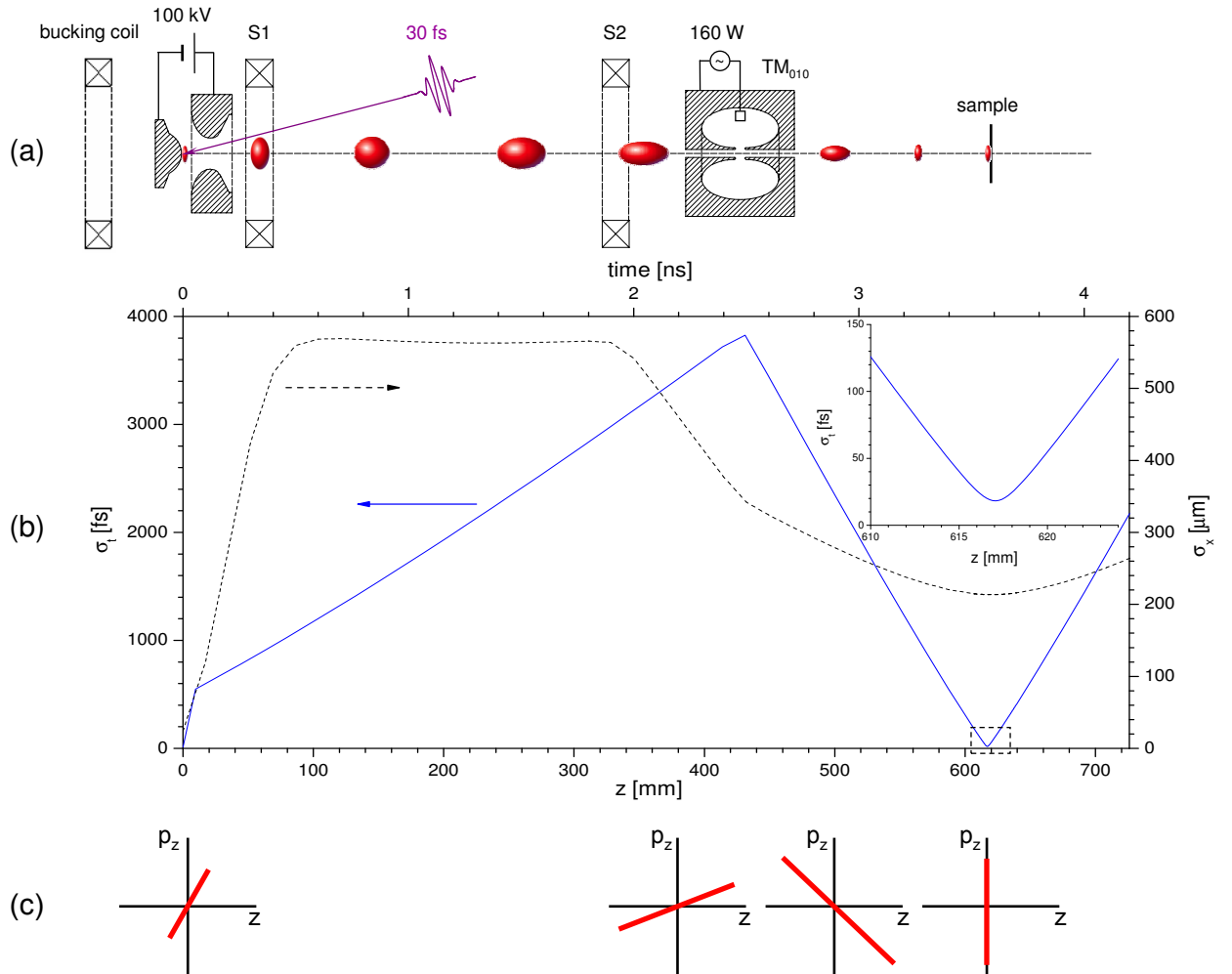
Figure 3.1: *(a) Schematic of the proposed setup. The setup is to scale, the bunches serve only as a guide to the eye. (b) RMS bunch duration σ_t (blue solid line) and RMS bunch radius σ_x (black dashed line) as a function of position z and time. The inset shows a close up of σ_t as a function of z around the focus position, which is indicated by the dashed square. (c) Schematics of the longitudinal phase-space distribution of the electron bunch at several key points in the setup.*

3.3.2 DC photogun design

We have designed a 100 kV DC photogun with the SUPERFISH code [21]. A bulk copper cathode is used, without a grid in front of it. Instead, an anode is used with a circular hole in it with a radius much larger than the typical beam radius. In this way field nonlinearities, which could lead to irreversible emittance growth, are minimized. The shapes of the cathode and the anode have been designed such that the highest field strength of 118 kV/cm is at the center of the cathode, while minimizing the divergence of the field around the particle trajectories. The center of the cathode is a flat circular area with a diameter of 1 mm, which is much larger than the laser spotsize. The diode geometry is shown in Fig. 3.2. The design of the entire photogun is described in detail in Sec. 4.2.
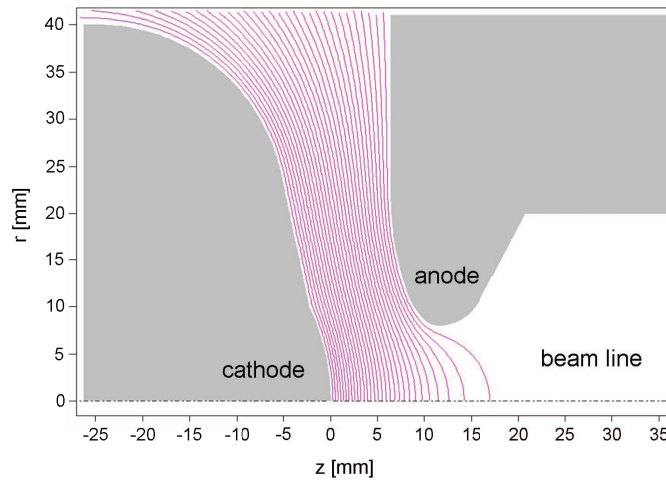
Figure 3.2: *The* SUPERFISH *design of the diode structure of the DC photogun. The dash-dotted line is the axis of rotational symmetry. The purple lines are equipotential lines.*

3.3.3 RF cavity design

The RF cavity has also been designed with the SUPERFISH code [21]. The design is shown in Fig. 3.3 and is described in detail in Sec. 5.4. This efficient cavity requires only 420 W input power to obtain the required field strength of 6.5 MV/m (see Sec. 3.2.2). This is a power reduction of about 90% compared with the regular pillbox geometry. 3 GHz RF powers up to 1 kW can be delivered by commercially available solid state RF amplifiers, so klystrons are not required. Furthermore, for transportation of the power from the RF source to the cavity coaxial transmission lines can be used instead of waveguides. Energy coupling between the coaxial line and the cavity is established with so-called magnetic coupling by bending the inner conductor of the coaxial cable into a small loop inside the cavity.
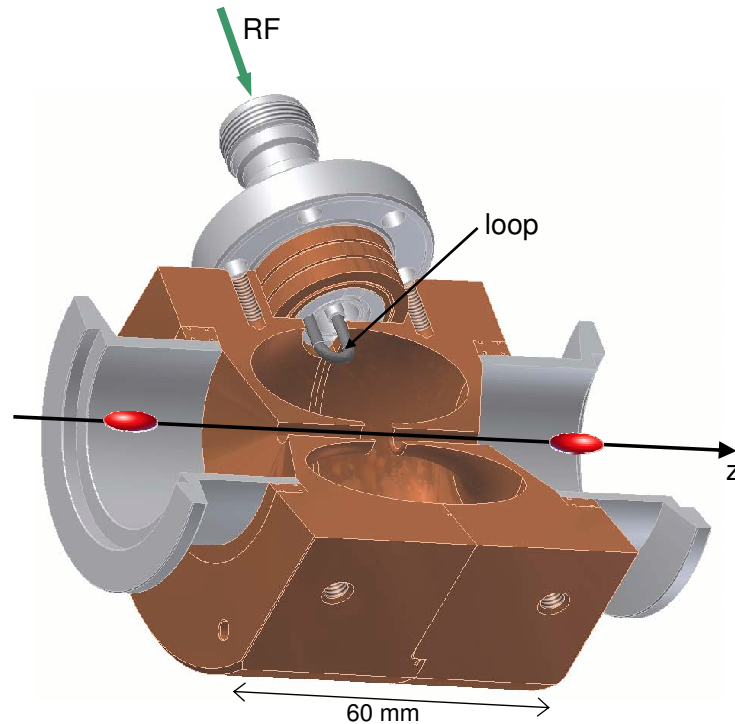
Figure 3.3: *Design of the RF cavity including the loop for energy coupling between the coaxial line and the cavity. The width of the gap where the electron bunches pass through is 6 mm, the total cavity width is 60 mm. The electron bunches are not to scale and serve only as a guide to the eye.*

3.4   Particle tracking simulations

The setup has been designed and optimized with the aid of the General Particle Tracer (GPT) code [22]. The bunch charge of 0.1 pC allows us to model the electrons in the bunch such that each macro-particle represents a single electron.

The electric fields of both the DC accelerator and the RF cavity, as presented in the previous section, have been calculated with the SUPERFISH set of codes [21] with $10\,\mu$m precision. The solenoids are modeled by a 4th order off-axis Taylor expansion from the analytical expression for the on-axis field. The effect of space-charge is accounted for by a Particle In Cell (PIC) method based on a 3-dimensional anisotropic multigrid Poisson solver, tailor made for bunches with extreme aspect ratios [23, 24]. Image charges are taken into account by a Dirichlet boundary condition at the cathode. Wakefields are not taken into account, but because of the low energy of the electrons, the low charge of the bunch, and the low peak current, these fields can be neglected.

The ideal initial half-circular electron density profile is approximated by a Gaussian transverse profile with a standard deviation of $\sigma_x = 50\,\mu$m truncated at a radius of $50\,\mu$m, corresponding to the one-sigma point. This profile is experimentally much more easy to realize and turns out to be sufficient to produce bunches with the required parameters at the focus. To simulate the photoemission process GPT creates a Gaussian longitudinal charge density

profile with a full-width-at-half-maximum (FWHM) duration of 30 fs. An isotropic 0.4 eV initial momentum distribution is used to model the initial emittance.

The optimized position of the RF cavity, at $z = 430$ mm, is a trade-off between desired longitudinal space-charge expansion to a few ps before injection and unavoidable accumulation of nonlinear effects. The position and on-axis field strength of solenoid $S2$, 334 mm and 0.03 T respectively, have been chosen such that the beam waist at the sample has the desired size and coincides with the time-focus.

The RF phase of the cavity must be tuned to minimize nonlinear effects in the longitudinal compression. The optimized phase is a slight deceleration: 11 degrees off the zero-crossing. To compensate for this slight RF deceleration the voltage of the DC accelerator has been raised from the nominal value of 100 kV to 120 kV to ensure we have at least 100 keV kinetic energy at the sample. Solenoid $S1$ is located at $z = 50$ mm, and produces an on-axis field of 0.05 T to collimate the beam. The amplitude of the cavity field is $E_0 = 4$ MV/m, which is lower than the result of the analytical calculation in Sec. 3.2.2. However, there it was assumed that the bunch had a constant RMS radius $\sigma_x = 200\,\mu$m, whereas from Fig. 3.1(b) it is clear that the radius is almost twice as large when the longitudinal compression starts. This larger radius results in a lower longitudinal space-charge field, so that a smaller compression field strength is required. Moreover, the assumption of a constant radius in the analytical calculation implies that the electrons have no transverse velocity, which is of course not the case: while longitudinal compression takes place the bunch is also transversely compressed. The contribution of the transverse velocity to the initial kinetic energy of the bunch is thus neglected in the analytical calculation.

The bunch evolution in the optimized setup is shown in Fig. 3.1(b). Due to the high space-charge fields the expansion becomes ballistic quickly after initiation of the bunch. The transverse and longitudinal asymptotic velocities are respectively $v_{R,\infty} = 2.9 \cdot 10^6$ m/s and $v_{L,\infty} = 3.5 \cdot 10^6$ m/s. These results are in good agreement with the analytical estimate in Sec. 3.2.2. After the diode the transverse beam-size is mainly determined by the two solenoids, but there is also a slightly defocusing effect of the RF cavity due to fringe fields at the apertures. When leaving the diode the longitudinal expansion speed drops abruptly by one order of magnitude to $v_L = 0.5 \times 10^6$ m/s due to the longitudinal exit kick of the diode, as explained in Sec. 3.2.2. The bunch then ballistically expands to several picosecond duration to be recompressed by the RF cavity to below 30 fs. From Fig. 3.1(b) it follows that this ballistic compression happens with a velocity difference $2v_L = 2.4 \times 10^6$ m/s, which is slightly smaller than the result of the estimation in Sec. 3.2.2. According to Eq. (3.6) this velocity difference can be induced with an RF field strength of only 4 MV/m, which is in perfect agreement with the value of this parameter in the simulation.

Figure 3.4 shows several projections of the phase-space distribution of the bunch at the sample: (a) the longitudinal phase-space distribution, (b) the transverse cross-section, (c) the current distribution, and (d) the transverse phase-space distribution. At the sample the 0.1 pC bunches are characterized by a RMS duration $\sigma_t = 20$ fs, a RMS radius $\sigma_x = 0.2$ mm, a transverse coherence length $L_\perp = 3$ nm, an average kinetic energy $U_k = 116$ keV, and a relative RMS energy spread $< 1\%$. In addition to the current distribution it is noted that the FWHM bunch duration of 30 fs covers 68% of the electrons in the bunch. A bunch duration of 100 fs covers 99.5% of the electrons. From Fig. 3.4 it is clear that the setup shown in Fig.

3.1(a) provides a practical realization of a device capable of producing electron bunches that fulfill *all* the requirements for single-shot UED.

Of all bunch parameters only the bunch duration is strongly dependent on the longitudinal position: over a range of 5 mm around the target position, i.e., $z = (617 \pm 2.5)$ mm, the RMS bunch duration varies between 20 fs and 50 fs, while the other parameters do not change significantly. To determine the location of the focal point in practice the bunch length has to be measured, which can be done with, e.g., laser ponderomotive scattering [11, 25] or Coulomb scattering with an electron cloud that is photoemitted from a metal grid [2].
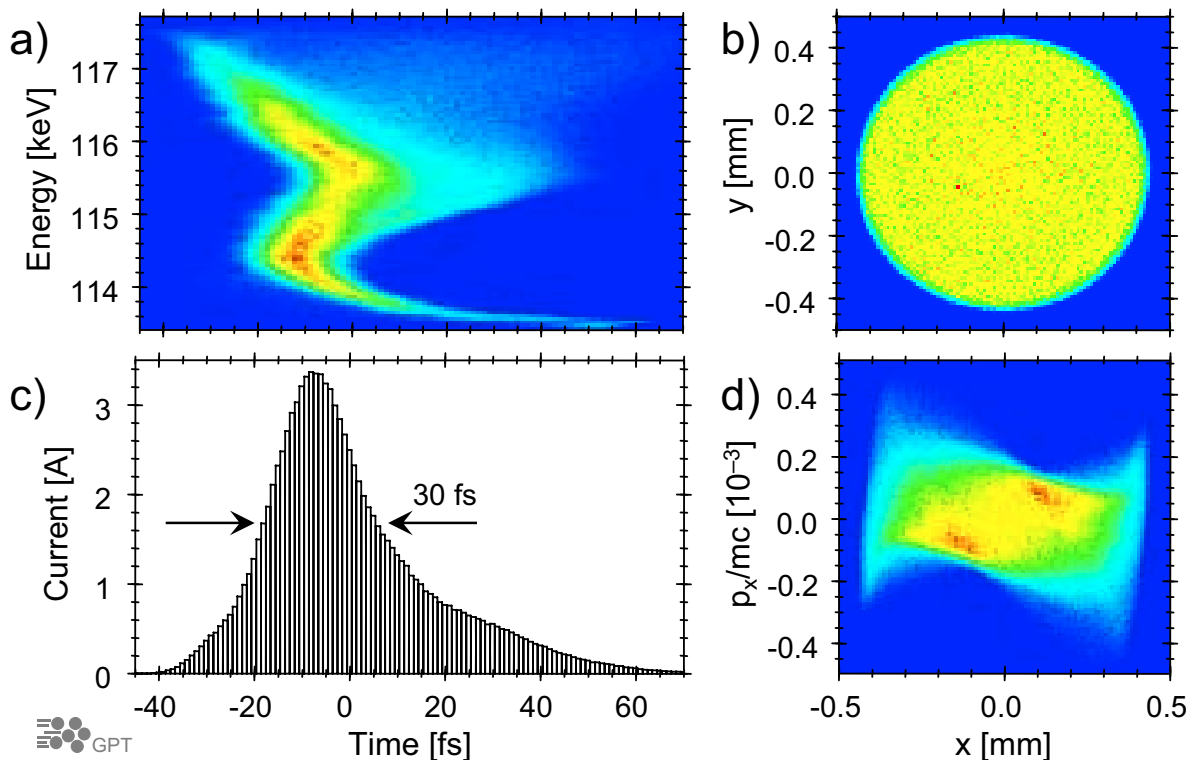
Figure 3.4: *(a) Longitudinal phase-space distribution, (b) cross-section, (c) current distribution, and (d) transverse phase-space distribution of the electron bunch at the sample.*

3.5 Stability considerations

For pump-probe experiments the arrival-time jitter should be less than the bunch duration, requiring a voltage stability of 10^{-6} for the power supply of the accelerator. This constraint is also more than sufficient for stable injection on the proper phase of the RF cavity. Such stable voltage supplies are commercially available. A second requirement is that the laser pulse is synchronized to the RF phase, also with an accuracy of less than the bunch duration. We have developed a synchronization system that fulfills this condition [20]. This leaves the initial spotsize as the main experimental parameter that influences the bunch quality. Simulations show that a deviation of 10% in spotsize decreases the coherence length by

0.2 nm as theoretically expected, while the bunch radius and bunch length at the sample do not change significantly.

3.6 Conclusions

In summary, we have presented a robust femtosecond electron source concept that makes use of space-charge driven expansion to produce the energy-correlated bunches required for radio-frequency compression strategies. This method does not try to circumvent the space-charge problem, but instead takes advantage of space-charge dynamics through transverse shaping of a femtosecond laser pulse to ensure the bunch expands in a reversible way [13]. This reversibility enables 6-dimensional phase-space imaging of the electron bunch, with transverse imaging accomplished by regular solenoid lenses and longitudinal imaging by RF bunch compression. Based on fundamental beam dynamics arguments and analytical estimates we have shown that in principle it is possible to create a 100 keV, 0.1 pC, sub-100 fs electron bunch, which has a spotsize smaller than 500 μm and a transverse coherence length of several nanometers. The results of our GPT simulations, which are consistent with the analytical estimates, convincingly show it is possible to realize such a bunch in realistic accelerating and focusing electric fields. We have designed a compact setup to create electron bunches that are suitable for single-shot, ultrafast electron diffraction experiments. With these bunches it will be possible for chemists, physicists, and biologists to study atomic level structural dynamics on the sub-100 fs timescale.

References

[1] R. Srinivasan, V. A. Lobastov, C.-Y. Ruan, and A. H. Zewail, Helv. Chim. Acta **86**, 1763 (2003).

[2] J. R. Dwyer, C. T. Hebeisen, R. Ernstorfer, M. Harb, V. B. Deyirmenjian, R. E. Jordan, and R. J. D. Miller, Phil. Trans. R. Soc. A **364**, 741 (2006).

[3] W. E. King, G. H. Campbell, A. M. Frank, B. W. Reed, J. Schmerge, B. J. Siwick, B. C. Stuart, P. M. Weber, J. Appl. Phys. **97**, 111101 (2005).

[4] B. J. Siwick, J. R. Dwyer, R. E. Jordan, and R. J. D. Miller, Science **302**, 1382 (2003).

[5] C.-Y. Ruan, V. A. Lobastov, F. Vigliotti, S. Chen, and A. H. Zewail, Science **304**, 80 (2004).

[6] F. Schotte, M. Lim, T. A. Jackson, A. V. Smirnov, J. Soman, J. S. Olson, G. N. Philips Jr., M. Wulff, and P. A. Anfinrud, Science **300**, 1944 (2003).

[7] B. J. Siwick, J. R. Dwyer, R. E. Jordan, and R. J. D. Miller, J. Appl. Phys. **92**, 1643 (2002).

[8] J. B. Hastings, F. M. Rudakov, D. H. Dowell, J. F. Smerge, J. D. Cardoza, J. M. Castro, S. M. Gierman, H. Loos, and P. M. Weber, Appl. Phys. Lett. **89**, 184109 (2006).

[9] J. D Geiser, and P. M. Weber, High repetition rate time-resolved gas phase electron diffraction, in *Proceedings of the SPIE conference on Time-Resolved Electron and X-Ray Diffraction*, volume 2521, page 136, 1995.

[10] E. Fill, L. Veisz, A. Apolonski, and F. Krausz, New J. Phys. **8**, 272 (2006).

[11] C. T. Hebeisen, G. Sciaini, M. Harb, R. Ernstorfer, T. Dartigalongue, S. G. Kruglik, and R. J. D. Miller, Opt. Express **16**, 3334 (2008).

[12] M. Harb, R. Ernstorfer, T. Dartigalongue, C. T. Hebeisen, R. E. Jordan, R. J. D. Miller, J. Phys. Chem. B **110**, 25308 (2006).

[13] O. J. Luiten, S. B. van der Geer, M. J. de Loos, F. B. Kiewiet, and M. J. van der Wiel, Phys. Rev. Let. **93**, 094802 (2004).

[14] S. B. van der Geer, M. J. de Loos, T. van Oudheusden, W. P. E. M. Op 't Root, M. J. van der Wiel, and O. J. Luiten, Phys. Rev. ST. Accel. Beams **9**, 044203 (2006).

[15] Ph. Piot, Review of experimental results on high-brightness photo-emission electron sources, in *The Physics and Applications of High Brightness Electron Beams*, edited by J. Rosenzweig, G. Travish, and L. Serafini, page 127, 2002.

[16] O. J. Luiten, Beyond the rf photogun, in *The Physics and Applications of High Brightness Electron Beams*, edited by J. Rosenzweig, G. Travish, and L. Serafini, page 108, 2002.

[17] B. W. Reed, J. Appl. Phys. **100**, 034916 (2006).

[18] O. D. Kellogg, *Foundations of Potential Theory*, Springer-Verlag, Berlin, 1929.

[19] B. Kung, H.-C.Lihn, H. Wiedemann, and D. Bocek, Phys. Rev. Lett. **73**, 967 (1994).

[20] F. B. Kiewiet, A. H. Kemper, O. J. Luiten, G. J. H. Brussaard, and M. J. van der Wiel, Nucl. Instrum. Methods A **484**, 619 (2002).

[21] J.H. Billen, and L.M. Young, Poisson Superfish.

[22] Pulsar Physics, `http://www.pulsar.nl/gpt`.

[23] S. B. van der Geer, O. J. Luiten, M. J. de Loos, G. Pöplau, and U. van Rienen, 3D space-charge model for GPT simulations of high brightness electron bunches, in *Institute of Physics Conference Series No. 175*, page 101, 2005.

[24] G. Pöplau, U. van Rienen, S. B. van der Geer, and M. J. de Loos, IEEE Trans. Magn. **40**, 714 (2004).

[25] B. J. Siwick, A. A. Green, C. T. Hebeisen, and R. J. D. Miller, Opt. Lett. **30**, 1057 (2005).

4

100 kV DC photogun

In the previous chapter a schematic overview of the entire setup is presented, with the focus on the physical concepts. In this and the next chapter the individual components are described in more technological detail as well as their connections regarding timing and synchronization. This chapter deals with the photogun, i.e., the laser and the accelerator, and magnetic lenses. First, in section 4.1, the femtosecond laser system is described that is used for photoemission of electrons. Section 4.2 is about the 100 kV DC accelerator. Key points in its design, that are presented in more detail, are the diode geometry and the high-voltage vacuum feedthrough. Also constructional details and practical operation are described. The solenoids, that are used for transverse focusing, are described in section 4.3. This chapter concludes with possible improvements of the setup in section 4.4.

4.1 Optical setup

4.1.1 Femtosecond laser

The laser system consists of an oscillator and an amplifier as shown schematically in Fig. 4.1. In the Ti:Sapphire oscillator (Coherent [1], Mantis) 30 fs pulses are created by means of self-mode-locking [2] through the Kerr effect. The center wavelength of the laser is 800 nm and the bandwidth is 84 nm. The repetition rate of the oscillator is adjustable between 74.84 MHz and 75.06 MHz with an accuracy of 3 kHz by moving an end mirror of the cavity. This mirror is placed on a piezo-motorized linear translation stage, that has a travel of 12 mm and a accuracy of 150 μm. We have added this feature to the standard design of the Mantis to be able to synchronize the 3 GHz radio-frequency (RF) phase to the laser pulses, as described in Sec. 5.8.1. During translation of this end mirror the oscillator remains mode-locked, while the output power (of typically 520 mW) changes less than 1 % and no alignment problems occur in the rest of the setup.

The pulses produced by the oscillator have an energy of typically 7 nJ. A Ti:Sapphire regenerative amplifier (Coherent, Legend) increases the pulse energy to 3.5 mJ by means of chirped pulse amplification [2]. The repetition rate of the amplifier is limited by its pump laser (Coherent, Evolution 30) that operates at 1 kHz. A Pockels cell is used to switch a pulse from the oscillator into the regenerative cavity, where it makes several round trips to
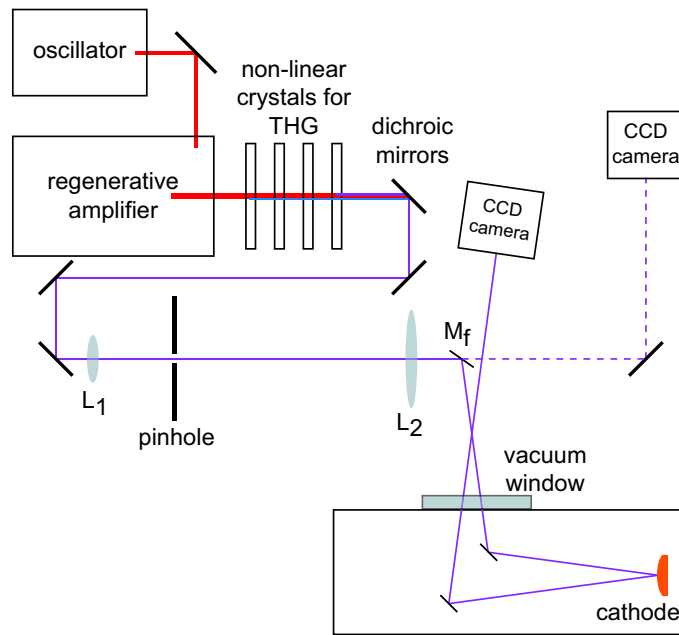
Figure 4.1: *Schematic overview of the laser system and beam path.*

be maximally amplified. A second Pockels cell switches the amplified pulse out of the cavity. For our experiments the repetition rate of the Pockels cells is set to 5 Hz.[1]

4.1.2   Third harmonic generation

The femtosecond laser pulses are used for photoemission of electrons from a copper cathode, as described in Sec. 3.3. Because the work function of copper is 4.65 eV the photon energy has to be tripled to enable linear photoemission. The third harmonic, ultraviolet (UV) pulse, is generated in a collinear setup of nonlinear crystals by means of sum-frequency generation, as described in detail in Ref. [3]. Based on the group velocity mismatch between the UV pulse and the fundamental (red) pulse it is estimated that the UV pulse has a duration of maximally 120 fs [3]. With a spotsize of approximately 1 mm the energy conversion efficiency from the red pulse to the UV pulse is several percent: a red pulse with energy of 1.5 mJ is sufficient to obtain a 20 μJ UV pulse. This enables extraction of electron bunches with charges $\lesssim 100$ pC from a copper photocathode, which is 2 orders of magnitude more than required for the experiments described in this thesis.

4.1.3   Laser pulse shaping

In order to create a waterbag bunch the transverse intensity profile of the photoemission laser pulse should be half-circular, as explained in Sec. 2.3. However, as shown in Sec. 3.4 a Gaussian profile, that is concentrically truncated at a radius $r = 1\sigma$ will also do. Because the latter profile is easier to realize we have used that one in our experiments. However, we

---

[1]The maximum repetition rate of the Pockels cells is equal to that of the pump laser, i.e., 1 kHz.
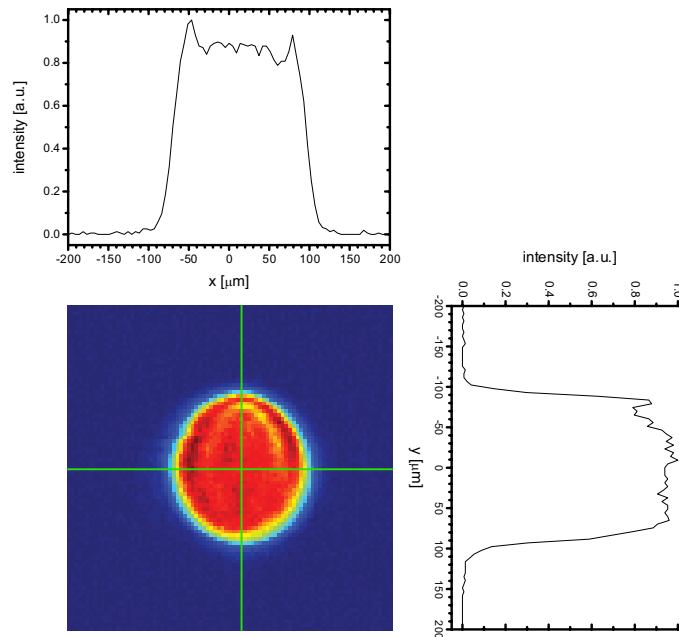
Figure 4.2: *Typical image of the UV laser spot at the virtual cathode, and horizontal and vertical intensity profiles along the lines indicated in the image.*

have also created a half-circular profile, as shown later on in this section, providing the possibility for future experiments on the precise conditions for creating a waterbag bunch. In this section first the creation of a truncated Gaussian laser profile is discussed.

Truncated Gaussian profile
A truncated Gaussian profile is created by focusing the laser onto a pinhole that has a diameter equal to the waist (2σ) of the laser. The pinhole is imaged 1:1 onto the photocathode using a single lens (see Fig. 4.1). The leakage through the final mirror before the vacuum entrance (mirror M_f in Fig. 4.1) is recorded by a CCD camera, that is positioned at the same distance from the pinhole as the photocathode. Hence this camera serves as a virtual cathode. Figure 4.2 shows a typical intensity profile of the laser spot at the virtual cathode.

A mirror, placed inside the electron beam line, directs the laser pulse onto the cathode, as illustrated in Fig. 4.1. The reflection of the laser pulse from the cathode surface is directed via another mirror to leave the vacuum. These two mirrors inside the beam line are spaced such that an electron bunch can pass in between. Outside the vacuum the cathode reflection is imaged onto a CCD camera. The lathing grooves of the cathode are clearly visible in the reflection which is conveniently used to align the laser at the center of the cathode, see Fig. 4.3.

Half-circular profile
A commercial device, called pi-shaper[2] [4], that presumably consists of two aspherical lenses[3], is used to convert a Gaussian laser profile into a half-circular profile. We have calculated the

---

[2]Originally this device had been developed to create a flat-top laser profile, which looks like the Greek letter pi. Hence the name pi-shaper.
[3]The manufacturer did not provide any details on the exact shape of the lenses.
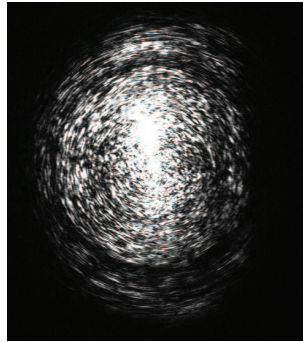
Figure 4.3: *Typical image of the reflection of the UV laser from the cathode. The lathing grooves of the cathode are clearly visible.*

shapes of two aspherical lenses that could be used together to create this profile [5]. The output profile of the pi-shaper depends on the size of the Gaussian laser spot at the entrance. According to simulations provided by the manufacturer it is possible to create a half-circular profile, as shown in Fig. 4.4(a). Figures 4.4(b) and 4.4(c) show typical profiles of a HeNe laser beam and of a femtosecond laser pulse respectively, both after being shaped with the pi-shaper. The required accuracy of the Gaussian width at the entrance of the pi-shaper, and the required accuracy of the alignment of the laser to the pi-shaper make it rather difficult to get the desired profile. Therefore shaping of the UV pulse with a pinhole, as described above, is used in our experiments, which is practically a much easier method.

(a)   (b)   (c)
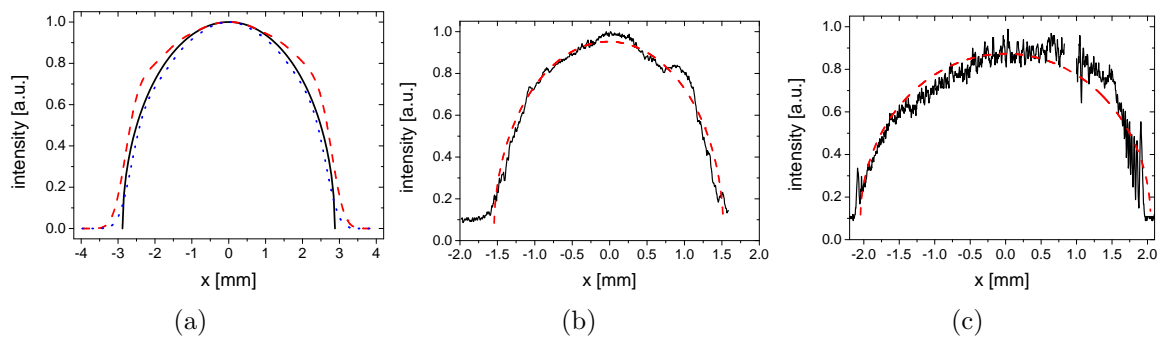
Figure 4.4: *(a) Simulations (performed by the manufacturer) of the output of the pi-shaper for a Gaussian laser beam with, at the entrance of the pi-shaper, $\sigma = 1.25\,\mathrm{mm}$ (dashed line) and $\sigma = 1.13\,\mathrm{mm}$ (dotted line) respectively. For comparison also an ideal half-circular profile is shown (solid line). (b,c) Measured output profiles (solid lines) of the pi-shaper, which are fitted to a half-circular profile (dashed lines). Panel (b) is the shaped profile of a HeNe laser, panel (c) is a profile of a femtosecond laser pulse. (The gap around $x = 0.9\,\mathrm{mm}$ is due to broken pixel arrays.)*

4.2   100 kV DC linear accelerator

This accelerator has been designed to demonstrate the waterbag concept and to be suitable for sub-relativistic electron diffraction. As follows from the parameter space (σ_0, E_{acc}), see figure 2.3, an acceleration field strength of about 10 MV/m should be sufficient to create a waterbag bunch with a charge of 0.1 pC and 50 μm initial radius. Taking into account the breakdown limit of vacuum, which is several tens of MV/m (see section 4.2.1), a maximum acceleration field strength of 10 MV/m is taken as starting point. The bunch has to leave the diode through a hole in the anode, which has to be considerably larger than the spotsize. According to particle tracking simulations a hole diameter of 1 cm is sufficient. The presence of this hole introduces nonlinearities in the acceleration field which are negligible close to the axis, if the distance between the cathode and the anode is larger than the radius of the hole [6]. These considerations are resulting in a gap spacing > 1 cm.

For electron diffraction experiments the preferred electron energy range is $30 - 300$ keV (see Sec. 3.1). In order to keep the DC gun compact a potential difference of 100 kV (instead of, e.g., 300 kV across a 3 cm gap) has been chosen. DC power supplies which go up to several 100 kV are commercially available.

Figure 4.5 shows an overview of the 100 kV DC photogun, that was designed and constructed in house. In the next section first some high-voltage considerations are addressed. Then the key parts of the accelerator are described in more detail, i.e., the diode geometry and constructional implementation, the high-voltage vacuum feedthrough, and the insulator.

4.2.1   High-voltage considerations

When the electric field strength at a surface is (locally) too high, breakdown can occur. In case of a breakdown a self-sustaining conducting path between the electrodes is created, meaning that the background gas in between the electrodes gets partially ionized. Although breakdown mechanisms are not fully understood yet, there are some generally accepted ideas, see e.g. [7, 8]. The ionization can be initiated by thermal emission, field emission, photoemission, or cosmic rays. Once a charged particle is present in the diode region it will be accelerated. Subsequent collisions of the accelerated particle with other atoms in the background gas may lead to further ionization. This way an avalanche could be built up, eventually leading to breakdown. Whether the avalanche grows or dies out depends on the chance that an accelerated charged particle ionizes other particles in the vacuum. This chance depends on the pressure p and the diode gap d. The breakdown voltage as a function of the product pd is described by the well-known Paschen law. For pressures below 10^{-4} mbar the mean free path of an electron is larger than about 1 m which is generally larger than the distance between the electrodes. For these lower pressures the breakdown voltage as a function of the diode gap has been determined empirically, yielding a breakdown voltage of 250 kV in case of a 1 cm gap [9]. Our goal of a 10 MV/m acceleration field strength, created by a potential difference of 100 kV across a 1 cm gap, as described in the previous section, is well below this empirical breakdown limit.

The local field strength is not only dependent on the potential difference and the distance between the electrodes, but also on the local curvature. For example, for a perfectly hemi-
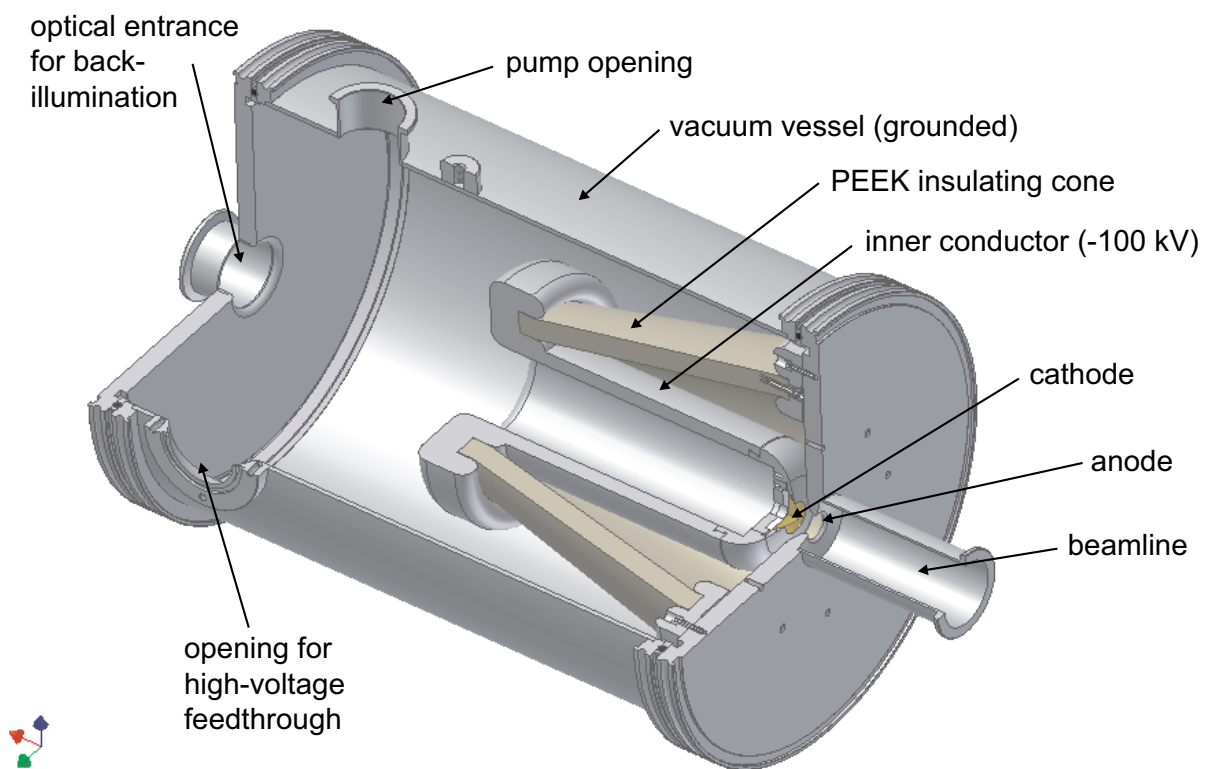
Figure 4.5: *3-Dimensional view of the design of the* 100 kV *DC photogun. Photoemitted electrons are accelerated towards the anode and are entering the beam line via the hole in the anode.*

spheric bump it can be calculated that the field at the top of the bump is increased by a factor of 3. For more peaked whiskers this factor is even higher. Because of the resulting local field enhancement, field emission is likely to occur and the whisker has become a possible breakdown initiator. Due to the high field strength the whiskers also heat up and could evaporate. This would increase the background pressure, and thereby the collision rate of charged particles with the background gas. Clearly microscopic surface roughness has to be seriously considered in the design and manufacturing of an accelerator.

Another location where a conducting path can be created is along the surface of an insulator, a breakdown mechanism called 'surface tracking' or 'surface flashover'. Especially when the field lines are parallel to the surface of the insulator released electrons can gain enough energy to cause a burst of insulating material on impact. Because the secondary emission coefficient generally exceeds unity an impact leads to a local positive charge, which then acts as an attractor for the (released) electrons. According to Ref. [10] a gradient $\lesssim 3\,\mathrm{kV/cm}$ parallel to the insulator surface is sufficient to prevent surface tracking.

Finally, so-called triple points, which are junctions of three different media, should be avoided or properly shielded. In designing an accelerator, triple points arise naturally at those places where a conductor connects to an insulator in a vacuum surrounding. Depending on the precise geometry the electric field strength could get enhanced in the vicinity of these points. Moreover, if the insulator gets locally charged due to secondary electron emission the field enhancement could lead to breakdown.

4.2.2   Accelerating diode structure: geometry optimization

The design of the diode is based on two requirements:

- the point of maximum field strength should be the tip of the cathode;

- the acceleration field in the diode should be sufficiently uniform over the diameter of the electron beam.

The first requirement ensures that the breakdown limit of the gun is determined by the diode, not by other parts of the gun. The second requirement is to prevent bunch degradation during acceleration.

The strategy is to design the diode with SUPERFISH [11], a 2-dimensional (2D) Poisson solver[4] to get the high-voltage requirements right. Next, particle tracking simulations with GPT are performed to check whether the designed diode field does not introduce unacceptable bunch degradation. The resulting optimized diode geometry is shown in Fig. 4.6, including equipotential lines. The ellipsoidal shape of the anode is the result of a trade off between the degree of curvature of the anode surface and the distance between the anode and the cathode, such that field enhancement is maximal at the cathode's tip. As explained in the previous section, the electric field gets enhanced at curved surfaces, requiring the distance to

---

[4]Because of the cylindrical symmetry of the geometry a 2D solver can be used.

the other electrode to be increased in order to keep the field strength below the breakdown limit.

The diode gap is 11.4 mm measured from the cathode's tip to the center of the hole in the anode. The radius of that hole is 8.0 mm. When supplying a voltage of -100 kV the acceleration field strength is 118 kV/cm at the cathode due to field enhancement. The effective diode gap is therefore 100 kV$/118$ kV/cm $= 8.5$ mm.
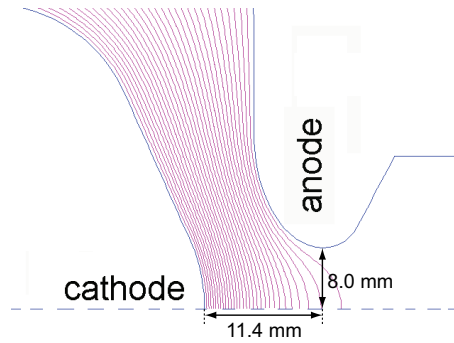
Figure 4.6: *Close-up of the diode geometry and the equipotential lines (between the cathode and the anode) as calculated with* SUPERFISH. *The dashed line is the axis of symmetry.*

4.2.3 Accelerating diode structure: constructional details

The photocathode itself could be either bulk, high-purity (99.99 %) OFHC copper (Outokumpu, ASTM C10100) or a piece of copper-coated glass. The latter allows back-illumination by the photoemission laser, which is easier to align. However, the quantum efficiency of the copper coating is low compared to bulk copper and the coating is damaged more easily. Therefore in our experiments we have used a bulk cathode.

The photocathode is clamped in a holder as shown in Fig. 4.7. At its backside a ring is screwed to push the cathode to ensure electrical contact with the holder (see Fig. 4.7). This design allows easy replacement of the cathode in case of deterioration or destruction due to, e.g., sparking.

The cathode-holder is screwed onto the head of an aluminum cylinder, that is at a negative high-voltage (down to -100 kV). The outer cylinder, i.e., the stainless steel vacuum vessel, is grounded and insulated from the inner conductor by a PEEK (PolyEtherEtherKeton) cone. The stainless steel plate at the right side of the gun is the anode, which is grounded as it is connected to the outer cylinder of the gun. The photoemitted electrons are accelerated towards the anode and are leaving the gun through the hole. All parts of the gun are made with an accuracy better than 0.1 mm, which is sufficient for proper alignment of the cathode with respect to the hole in the anode.

4.2.4 Insulator

The dimensions of the 100 kV photogun result in a natural way from the breakdown considerations discussed in Sec. 4.2.1. The insulating PEEK (PolyEtherEtherKeton) cone should
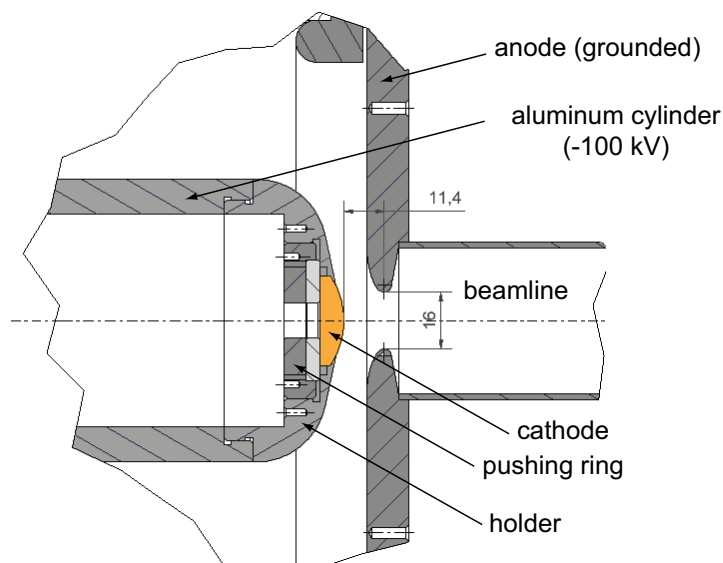
Figure 4.7: *Technical drawing of a bulk copper photocathode clamped in the holder. A ring is pushing at the back to ensure electrical contact between the cathode and the holder.*

have a length of minimally 30 cm and the cone should be oriented such that the electric field lines are not parallel to the cone's surface. Other distances and radii are chosen such that the electric field strength is lower than 100 kV/cm, keeping a safety margin with the earlier quoted limit of 250 kV/cm. Triple points are shielded by structures as illustrated in Fig. 4.8, which counteract local field enhancement.

The PEEK cone splits the vacuum chamber into two parts, inside and outside the cone. However, both parts are connected to the same vacuum pump and the junction of the PEEK cone to the anode plate is not vacuum sealed.

With its good milling machine characteristics and ultrahigh vacuum applicability PEEK is a low-cost alternative to other vacuum-compatible insulators, like Macor.
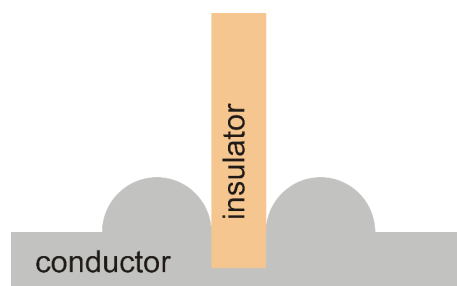
Figure 4.8: *Triple point shielding.*

4.2.5 High-voltage supply and vacuum feedthrough

The high-voltage power supply (Matsusada [12], AU-100N1.5-L(220V)) has an output ranging from 0 to −100 kV and can deliver a maximum current of 1.5 mA. The high-voltage coaxial
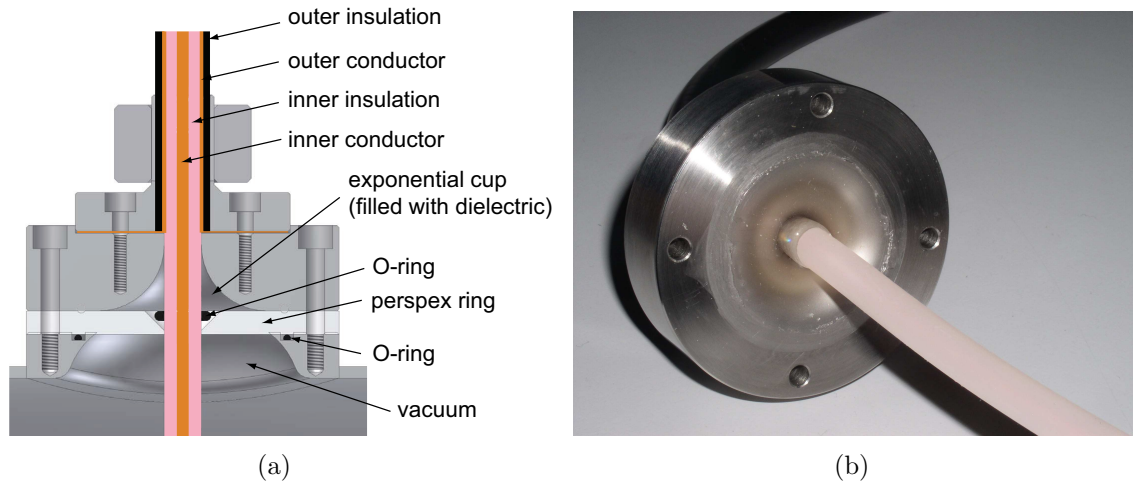
Figure 4.9: *The high-voltage feedthrough. (a) Technical drawing. (b) Photograph. The inner conductor and the inner insulation pass through the feedthrough. The exponential cup is filled with a dielectric.*

cable enters the gun via the feedthrough shown in Fig. 4.9. About 50 cm from the end of the cable the outer conductor is stripped off and connected to the vacuum vessel. The inner insulator and conductor enter the vacuum vessel. The inner side of the feedthrough widens exponentially, as shown in Fig. 4.9(a), to lower the field strength along the cable. This so-called exponential cup is the result of a trade off between distance and curvature. At the entrance, where the cup has a small diameter, there will be a large voltage drop across the vacuum between the cup and the inner insulation of the cable. To lower the maximum field strength the cup is filled with dielectric material (Emerson & Cuming, Stycast 1266), which is poured as a liquid into the cup and subsequently cured. In this process special care should be taken to prevent air bubbles in the dielectric, which may lead to high field strengths in the cup.

To make the feedthrough vacuum compatible an O-ring is put tightly around the inner insulation of the cable. A perspex ring pushes the O-ring onto the epoxy. The assembly is screwed on top of the vacuum vessel where another O-ring (between the vessel and the perspex ring) seals the vacuum.

At the end of the cable about 1 cm of the insulation is stripped off. The inner conductor is connected to the high-voltage cylinder inside the gun, onto which the cathode is mounted. A cable length of about 40 cm inside the gun is necessary to minimize surface tracking. On the other hand the cable should not be to close to the wall to prevent breakdown.

4.2.6 Training of the 100 kV DC photogun

As whiskers are believed to be the main source of breakdowns they should be removed from the surfaces inside the accelerator. This is done by so-called 'training' or 'conditioning' of the photogun. This simply means that the voltage is gradually increased until a breakdown occurs. Then quickly the high voltage is lowered or turned off. In this way 'gentle' breakdowns will smooth the surfaces: due to heating whiskers are evaporated, but there has not been
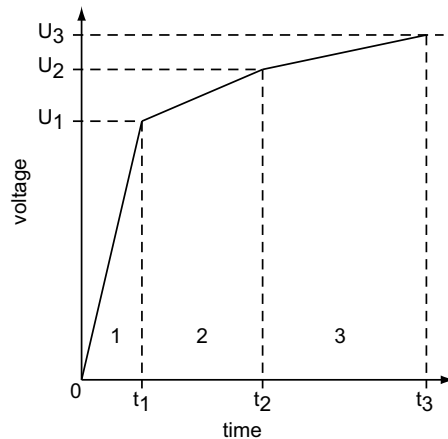
Figure 4.10: *Training scheme of the photogun. There are three different regimes of which the ramp and final voltage are adjustable.*

enough time to build up a severe breakdown, which may lead to increased surface roughness.

We have automated this process. Three ramping regimes are used, as illustrated in Fig. 4.10. The voltage limits U_1, U_2, and U_3 are adjustable. Also the ramps in the three regimes are adjustable and are chosen to be 10 kv/min, 1 kV/min and 0.5 kV/min. Once the accelerator has been fully conditioned (i.e., when 100 kV can be reached without breakdown problems) we choose for the limits $U_1 = 75.0$ kV, $U_2 = 90.0$ kV, and $U_3 = 100$ kV. In case of a breakdown the voltage is shut off and the values of U_1 and U_2 are set to 85% and 95% of the breakdown voltage, before restarting the conditioning.

Furthermore, during the voltage ramp the current is monitored continuously. In case of a current between 5 μA and 10 μA the voltage is held constant until the current has dropped to below 5 μA. In case of a current higher than 10 μA the voltage is shut off.

With this strategy the final voltage of 100 kV is reached within 2 days of conditioning. However, for stability reasons most experiments have been carried out at 90.0 or 95.0 kV.

4.3   Solenoidal magnetic lens

To focus charged particle beams solenoids are commonly used. The focal length f_l of a solenoid is given by [7]

$$f_l = \frac{4U_k(U_k + 2mc^2)}{c^2 e^2 \int_{-\infty}^{\infty} B_z(0,z)^2 dz},\tag{4.1}$$

with U_k the kinetic energy and m the mass of the particle, c the speed of light, and e the elementary charge. $B_z(0,z)$ is the longitudinal magnetic field on the z-axis, which is the axis of cylindrical symmetry, and is given by [13]
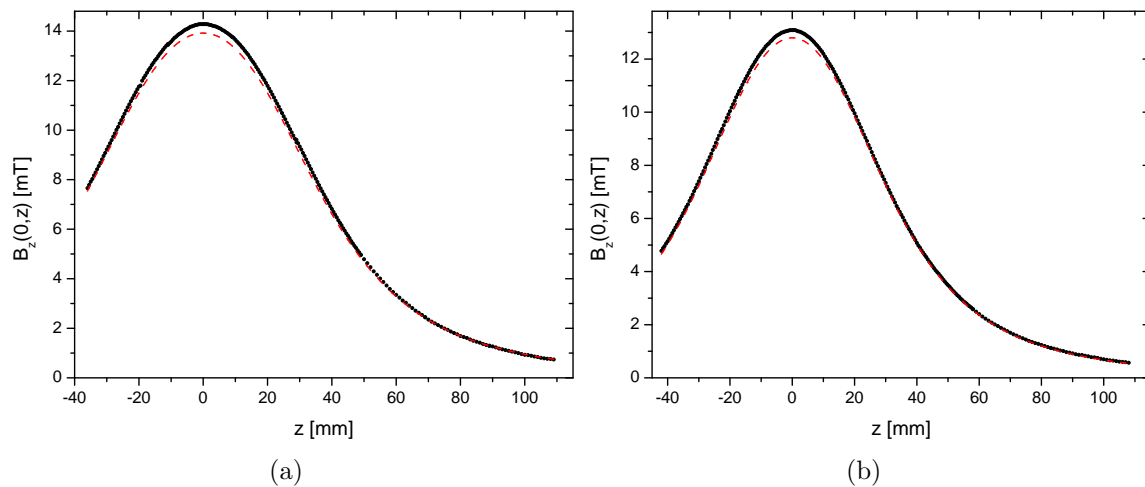
Figure 4.11: *Measured (dots) and calculated (dashed line) on-axis magnetic field at $I_s = 1\,\mathrm{A}$ of (a) solenoid 1 and (b) solenoid 2. The dimensions of the solenoids are specified in Table 4.1.*

$$B_z\left(0, z\right) = \frac{\mu_0 N_w I_s}{2L\left(\alpha - 1\right)}\left\{ z \ln\left[\alpha\frac{1 + \frac{1}{\alpha\rho_{in}}\sqrt{\alpha^2\rho_{in}^2 + z^2}}{1 + \frac{1}{\rho_{in}}\sqrt{\rho_{in}^2 + z^2}}\right] - \ldots\right.$$

$$\left.\ldots\left(z - \beta\rho_{in}\right)\ln\left[\alpha\frac{1 + \frac{1}{\alpha\rho_{in}}\sqrt{\alpha^2\rho_{in}^2 + (z - \beta\rho_{in})^2}}{1 + \frac{1}{\rho_{in}}\sqrt{\rho_{in}^2 + (z - \beta\rho_{in})^2}}\right]\right\}, \qquad (4.2)$$

with μ_0 the permeability of vacuum, I_s the current, N_w the number of windings, L the length of the solenoid, ρ_{in} and ρ_{out} the inner and outer radius of the solenoid respectively, $\alpha = \rho_{out}/\rho_{in}$, and $\beta = L/\rho_{in}$.

As pointed out in Sec. 3.3 two solenoids are used in our setup to focus $100\,\mathrm{keV}$ electron bunches. The specifications of both solenoids are summarized in Table 4.1. Figure 4.11 shows the measured on-axis magnetic fields of solenoid 1 and 2, which are mostly consistent with the calculated profiles (using Eq. (4.2)), except around $z = 0$ where the measured value is about 3% higher than the theoretical value.

The wire of the solenoids has a copper core, an insulating layer and a bonding layer. The solenoid is maximally packed, such that neighboring windings connect to each other. After winding, the solenoid is heated in an oven to melt the bonding layer, thereby merging the insulation of the wires for optimum thermal conductivity. When the solenoid is in operation the heat is dissipated to a water channel at the side plate of the solenoid. This method is sufficient to prevent excessive heating when driving the solenoids with currents up to $5\,\mathrm{A}$.

A third solenoid was designed and constructed in house. To conduct heat from the inside of the solenoid to the outside spaces between the loops are filled with thermoconductive paste. This solenoid is used to image a diffraction pattern onto a micro-channel plate.

Table 4.1: *Specifications of the solenoids. The magnetic field strengths have been measured with a Hall probe.*

parameter	solenoid 1	solenoid 2	solenoid 3
ρ_{in} [mm]	60.0	60.0	58.4
ρ_{out} [mm]	102.0	91.8	91.6
L [mm]	51.7	38.3	42.0
N	1055	859	600 ± 20
R [Ω]	5.90	6.88	4.3 ± 0.5
$B_z(0,0)$ [mT] @ $I_s = 1$ A	14.3 ± 0.1	13.1 ± 0.1	8.9 ± 0.5

4.4   Recommendations

After more than 4 years of reliable operation we conclude that the design of our 100 kV DC photogun is robust. Only two problems showed up in practice. (1) Initially, inside the photogun the high-voltage cable was too close to the wall. This was easily solved by shortening the cable [14]. (2) After about 1 year of operation the high-voltage feedthrough developed a vacuum leak. At the time the exponential cup was filled with another epoxy (Dow Corning, Sylgard 184 Silicone elastomer). Also, in the initial design the O-ring around the inner cable and the perspex ring to push this O-ring, were not present. Adding this feature provided a quick solution, and thereafter the feedthrough has been operating without any problems.

Concerning the trajectories of sub-relativistic electrons, it is recommended to place coils around the setup that compensate for the earth magnetic field. The beam line should be made out of non-magnetic materials. This holds for all components, like flanges, bellows, clamps, screws, bolts, and nuts. Other common components in a vacuum system that can have magnetic parts are pressure gauges and valves, which should be shielded or placed sufficiently far away from the electron beam path.

If higher kinetic energies are required the design of this photogun can principally be upscaled. However, it quickly becomes a rather big apparatus. Therefore, it is recommended to add a booster radio-frequency (RF) cavity to the 100 kV DC photogun, or to use a RF photogun if higher energies are required.

References

[1] Coherent Inc., `http://www.coherent.com`.

[2] J.-C. Diels, *Ultrashort Laser Pulse Phenomena*, Academic Press, 1996.

[3] W. P. E. M. Op 't Root, *Generation of high-field, single-cycle terahertz pulses using relativistic electron bunches*, PhD thesis, Technische Universiteit Eindhoven, 2009.

[4] MolTech GmbH, `http://www.mt-berlin.com/`.

[5] E. P. Smakman, Transverse laser profile shaping: evaluating the pishaper, Master thesis, Technische Universiteit Eindhoven, 2007.

[6] J. D. Jackson, *Classical Electrodynamics*, John Wiley & Sons, New York, 1999.

[7] S. Humphries Jr., *Principles of Charged Particle Acceleration*, John Wiley & Sons, New York, 1997.

[8] D. B. Go, and D. A. Pohlman, J. Appl. Phys. **107**, 103303 (2010).

[9] L. L. Alston, *High Voltage Technology*, Oxford University Press, 1968.

[10] A. Roth, *Hochspannungstechnik*, Springer-Verlag, 1965.

[11] J.H. Billen, and L.M. Young, Poisson Superfish.

[12] Matsusada Precision Inc., `http://www.matsusada.com`.

[13] H. Zijlstra, *Experimental Methods in Magnetism, 1. Generation and Computation of Magnetic Fields*, North Holland Publishing Co., 1967.

[14] T. van Oudheusden, Dream beam, from pancake to waterbag, Master thesis, Technische Universiteit Eindhoven, 2006.

5

RF cavities

To manipulate and diagnose the longitudinal phase-space of electron bunches we use radio-frequency (RF) cavities (see Fig. 6.3). A cavity oscillating in the TM_{010} mode is used to compress the bunch, and a cavity oscillating in the TM_{110} mode acts as a deflector in a streak camera to measure the bunch length. In this chapter the design, fabrication, and characterization of both cavities is presented. Our cavities have a design resonant frequency of 2.9985 GHz. As this is the standard European S-band radar frequency, high precision components are commercially available. Over the last decade our group has gained experience with RF accelerators and accompanying sources and infrastructure that operate at this frequency [1, 2].

The cavities in this thesis have a more power efficient design than the straightforward pillbox geometry. However, a pillbox cavity allows analytical calculations of the field distribution and the Q-factor. Basic cavity theory, based on a pillbox cavity, is presented in Sec. 5.1. Then, in Sec. 5.2, a cavity is modeled by lumped elements to derive its frequency dependent absorption and transient behavior. The basic geometry of a more power efficient cavity design is presented in Sec. 5.3. Then the actual design and characterization (absorption and on-axis field profile) of both the compression cavity and the streak cavity are presented in Sec. 5.4 and 5.5 respectively. Details on the loop antenna, that is used to couple the power into the cavity, are described in Sec. 5.6. The entire setup for high power driving of the cavities is presented in Sec. 5.7 as well as thermal effects. Finally, in Sec. 5.8, synchronization of the RF phase to the femtosecond laser is described.

5.1   Pillbox cavity

The pillbox cavity is a cylinder with radius R and length d, as illustrated in Fig. 5.1. It is the simplest cylindrically symmetric cavity geometry. For completeness we show in this section its well-known electro-magnetic (EM) fields and its quality factor. In the next section we show its resonant frequency, bandwidth, and transient behavior as follows from lumped element modeling.
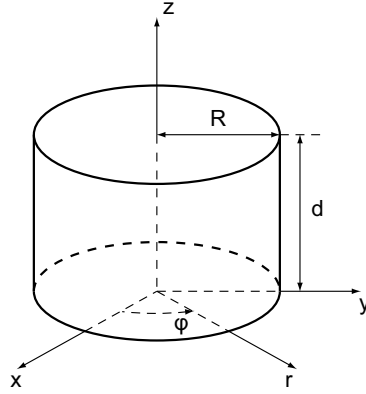
Figure 5.1: *Pillbox cavity with radius R and length d and definition of cylindrical coordinates r, φ, and z.*

5.1.1 RF fields

Maxwell's equations together with proper boundary conditions give a closed description of the electric and magnetic fields inside a cavity. Consider a pillbox cavity with perfectly conducting walls, and containing a lossless medium that is characterized by a permittivity ϵ and a permeability μ. The longitudinal component of the electric field of transverse magnetic (TM) modes inside such a cavity is given by

$$E_z(r, \varphi, z, t) = E_0 J_m(kr) \cos(m\varphi) \cos\left(p\pi\frac{z}{d}\right) \cos(\omega t), \tag{5.1}$$

where J_m is the m-th Bessel function of the first kind, and $k^2 = \epsilon\mu\omega^2 - p^2\pi^2/d^2$, with angular frequency $\omega = 2\pi f$. The different possible modes are characterized by m and p, with $\{m, p\} \in \mathbb{N}_0$. The assumption of perfectly conducting walls is described by the boundary condition $E_z(R, \varphi, z, t) = 0$ that is fulfilled when $J_m(kR) = 0$. From this it follows that the resonant frequency ω_0 of a TM_{mnp} mode is given by

$$\omega_{mnp} = \frac{1}{\sqrt{\epsilon\mu}} \sqrt{\frac{x_{mn}^2}{R^2} + \frac{p^2\pi^2}{d^2}}, \tag{5.2}$$

where x_{mn} is the n-th root of $J_m(x) = 0$ (thus $n \in \mathbb{N}$). The mode numbers m, n, p are the number of nodes in the φ-, r-, and z-direction respectively. Generally, also for other cavity geometries than a pillbox, the mode is defined by the number of nodes m, n, p.

With $E_z(r, \varphi, z)$ known, the other components of an EM field in a resonant pillbox cavity follow from Maxwell's equations. For the TM_{010} mode this results in

$$E_z(r, z, t) = E_0 J_0\left(\frac{x_{01}r}{R}\right) \cos(\omega_0 t); \tag{5.3a}$$

$$B_\varphi(r, \varphi, t) = \sqrt{\epsilon\mu} E_0 J_1\left(\frac{x_{01}r}{R}\right) \sin(\omega_0 t). \tag{5.3b}$$

All other field components are zero. For this mode the resonant frequency $\omega_0 = x_{01}/(R\sqrt{\epsilon\mu})$. With $x_{01} \approx 2.405$ it follows that a pillbox cavity with radius $R = 38.3\,\text{mm}$, that contains a

vacuum, has a resonant frequency $f_0 = 3\,\text{GHz}$.

The nonzero electric and magnetic field components of the TM_{110} mode are

$$E_z(r, \varphi, z, t) = E_0 J_1\left(\frac{x_{11}r}{R}\right)\cos(\varphi)\cos(\omega_0 t); \tag{5.4a}$$

$$B_r(r, \varphi, t) = \frac{1}{\omega_0 r} E_0 J_1\left(\frac{x_{11}r}{R}\right)\sin(\varphi)\sin(\omega_0 t); \tag{5.4b}$$

$$B_\varphi(r, \varphi, t) = \frac{1}{\omega_0} E_0 \frac{\partial}{\partial r} J_1\left(\frac{x_{11}r}{R}\right)\cos(\varphi)\sin(\omega_0 t), \tag{5.4c}$$

with resonant frequency $\omega_0 = x_{11}/(R\sqrt{\epsilon\mu})$, where $x_{11} \approx 3.832$. For this mode $f_0 = 3\,\text{GHz}$ for a vacuum pillbox cavity with radius $R = 60.9\,\text{mm}$. Close to the z-axis the magnetic field components can be approximated using $\frac{1}{r}J_1(kr) \approx \frac{\partial}{\partial r}J_1(kr) \approx \frac{k}{2}$ for $r = \sqrt{x^2 + y^2} \ll R$. In cartesian coordinates this approximation yields

$$B_x = 0; \tag{5.5a}$$

$$B_y = \frac{\sqrt{\epsilon\mu}}{2}E_0\sin(\omega_0 t). \tag{5.5b}$$

5.1.2 Power loss, energy storage, and quality factor

In the previous section perfectly conducting walls are assumed. In practice however, the conductivity of the walls is finite, leading to power dissipation. Also a lossless dielectric inside the cavity is assumed in the previous section, which still holds in case of a vacuum. The ratio of the time-averaged energy stored U_{strd} in the cavity to the power loss P_{loss} per cycle is called the quality factor Q. It is defined as

$$Q = \omega_0 \frac{U_{strd}}{P_{loss}}. \tag{5.6}$$

The time-averaged stored energy can be calculated straightforwardly according to

$$U_{strd} = \frac{1}{2}\int_{volume}\left(\epsilon|\vec{E}(r, \varphi, z)|^2 + \frac{1}{\mu}|\vec{B}(r, \varphi, z)|^2\right)dV \tag{5.7a}$$

$$= \frac{\varepsilon}{2}\pi E_0^2 J_1^2(x_{01})R^2 d, \tag{5.7b}$$

where the second line holds for the TM_{010} mode. The equation for the TM_{110} can be found in Ref. [3].

To calculate the Ohmic power loss in the cavity walls the skin depth is usually taken as the typical penetration depth of an EM field into the material. The skin depth δ_s is given by [4]

$$\delta_s = \sqrt{\frac{2}{\mu_w \sigma_w \omega}}, \tag{5.8}$$

with μ_w and σ_w the permeability and conductivity of the cavity wall material respectively. For a copper cavity $\mu_w = 1.26 \cdot 10^{-6}\,\text{H/m}$ and $\sigma_w = 5.84 \cdot 10^7\,\Omega^{-1}\text{m}^{-1}$ at $T = 298\,\text{K}$ [5], leading to a skin depth $\delta_s = 1.2\,\mu\text{m}$ if $f = 3\,\text{GHz}$.

The time-averaged power loss can be calculated using

$$P_{loss} = \frac{R_w}{2} \int_{walls} \frac{1}{\mu^2} |\vec{n} \times \vec{B_w}|^2 dS \tag{5.9a}$$

$$= R_w \frac{\varepsilon}{\mu} \pi E_0^2 J_1^2(x_{01}) R(R+d), \tag{5.9b}$$

where the second line holds for the TM_{010} mode. (The equation for the TM_{110} mode can be found in Ref. [3]). In the equation above $R_w = 1/(\sigma_w \delta_s)$ is the resistance of the wall, $\vec{n}$ is the surface normal, and B_w is the magnetic field at the wall. Because for a pillbox cavity the EM fields are known analytically U_{strd} and P_{loss}, and thus Q, can be calculated. For both the TM_{010} and the TM_{110} mode the quality factor expressed in terms of radius, length, and skin depth is given by

$$Q = \frac{1}{\delta_s} \frac{\mu}{\mu_w} \frac{Rd}{R+d}. \tag{5.10}$$

In general a high Q is desirable, because then a relatively low power source would be sufficient to generate high field amplitudes. As is discussed in Sec. 5.3, changing the geometry of the cavity can influence the Q-factor such that up to 90% power saving is possible in comparison to the pillbox geometry. For example, a $3\,\text{GHz}$ TM_{010}pillbox cavity with $d = 6\,\text{mm}$ has a quality factor $Q = 4.3 \cdot 10^3$, which is almost half the quality factor of our power efficient cavity presented in Sec. 5.4. Another consequence of a higher Q is a smaller bandwidth of the cavity (as shown in the next section) and a longer build-up time of the EM field in case of a pulsed source (see the next section).

5.2   Lumped element modeling

5.2.1   Steady state

Considering the cavity as a resonator network, which is lumped element modeling, is useful to derive the bandwidth of a cavity and to understand the idea of impedance matching. The resonant cavity can be modeled as either a series or a parallel circuit with a resistance R_c, a capacitance C, and an inductance L. In this thesis the arbitrary choice for a series circuit is made. The complex impedance of this circuit is given by

$$Z(\omega) = R_c + i\omega L + \frac{1}{i\omega C}. \tag{5.11}$$

Assume the resonator network is driven by an ideal voltage source, i.e., there is no internal resistance in the source and its output is purely sinusoidal with angular frequency ω. The time-averaged power loss in the resonator is then $P_{loss} = \frac{1}{2}|I_0|^2 R_c$, where I_0 is the current amplitude. The time-averaged energy stored in the capacitance and inductance are respectively $U_\text{C} = \frac{1}{4}|I_0|^2 \frac{1}{\omega C}$ and $U_\text{L} = \frac{1}{4}|I_0|^2 L$. The complex power delivered to the network is

$P(\omega) = \frac{1}{2}|I_0|^2 Z(\omega)$. When driving the network at its resonant frequency ω_0 the average energy stored in the capacitance and inductance are equal, from which it follows that $\omega_0 = \frac{1}{\sqrt{LC}}$. It also follows that $Z = R_c$, implying that the power delivered to the network is purely used to compensate for Ohmic losses. Using these results the Q-factor, see Eq. (5.6), in terms of lumped elements is written as[1]

$$Q_0 = \omega_0 \frac{L}{R_c} = \frac{1}{\omega_0 R_c C}. \tag{5.12}$$

Combining this equation with Eq. (5.11) yields for the impedance

$$Z(\omega) = R_c \left[1 + iQ_0 \left(\frac{\omega}{\omega_0} - \frac{\omega_0}{\omega} \right) \right] \tag{5.13a}$$

$$\approx R_c \left[1 + i2Q_0 \left(\frac{\Delta\omega}{\omega_0} \right) \right], \tag{5.13b}$$

where $\Delta\omega = \omega - \omega_0$. The approximation holds when $|\Delta\omega| \ll \omega_0$, which is generally true when exciting a network near or at resonance. Using this result the ratio of the power P absorbed by the network to the power $P_g = \frac{1}{2}|I_0|^2 R_c$ generated by the source is calculated to be

$$\frac{P}{P_g} = \frac{1}{1 + \left(2Q_0 \frac{\Delta\omega}{\omega_0} \right)^2}. \tag{5.14}$$

The power absorption as a function of frequency is thus described by a Lorentzian. At resonance maximal power is absorbed by the network. Using the equation above the full-width-at-half-maximum (FWHM) or bandwidth BW of the network is given by

$$BW = \frac{\omega_0}{Q_0}. \tag{5.15}$$

From Eq. (5.13b) it follows that a frequency change translates into a phase change as follows

$$\varphi(\omega) \approx \arctan\left(2Q_0 \frac{\Delta\omega}{\omega_0} \right). \tag{5.16}$$

Frequency tuning is used to synchronize the RF phase with femtosecond laser pulses as described in Sec. 5.8.1.

When the voltage source does have an internal impedance, maximum power is transferred to the network when the impedances of the source and the network are each others complex conjugate. This is called impedance matching. For a source that has a fixed, purely real impedance R_g matching is obtained when $\omega = \omega_0$ *and* $R_c = R_g$. Usually an external Q-factor is defined as $Q_{ext} = \omega_0 \frac{L}{R_g} = \frac{1}{\omega_0 R_g C}$. The quality factor that describes the entire system is called loaded Q-factor and is related to the unloaded Q_0 and external Q_{ext} by

---

[1]For the Q-factor there is a difference between a series and a parallel circuit for the mapping of values of losses onto R_c, L, and C. The equation presented here only holds for a series RLC-circuit.

$$\frac{1}{Q_{\mathrm{L}}} = \frac{1}{Q_0} + \frac{g}{Q_{ext}}, \tag{5.17}$$

where $g = Q_0/Q_{ext}$ is the coupling factor[2], which describes the matching between the source and the network. Because the power is now partially absorbed by the resistance of the source Eq. (5.14) changes into

$$\frac{P}{P_{max}} = \frac{4g}{(1+g)^2 + 4Q_0^2 \left(\frac{\Delta\omega}{\omega_0}\right)^2}. \tag{5.18}$$

Here P_{max} is the maximum power absorbed by the resonator, which is equal to half the power of the generator in case of perfect matching ($g = 1$). Then the absorbed power is described by a Lorentzian. The bandwidth of the entire system is given by

$$BW = \omega_0 \left(\frac{1}{Q_0} + \frac{g}{Q_{ext}}\right) \tag{5.19a}$$

$$= \frac{\omega_0}{Q_{\mathrm{L}}} = \frac{2\omega_0}{Q_0}, \tag{5.19b}$$

where the second line only holds for the case of perfect matching.

5.2.2   Transient behavior

In the previous section a steady-state RLC-network is assumed. However, if the output of the power source that drives a cavity varies in time it takes some time for the EM field amplitude to adjust accordingly. In this section the case of switching on the power source is considered, which is modeled by a Heaviside step function with amplitude U_g. In case of perfect matching ($g = 1$) and no detuning ($\Delta\omega = 0$) the power stored in the network is given by[3]

$$U_{strd}(t) = U_g Q_0 \left(1 - e^{-\omega_0 t/Q_0}\right)^2. \tag{5.20}$$

The power delivered to the network balances the rate of energy storage and the power loss:

$$P(t) = \frac{dU_{strd}(t)}{dt} + \frac{\omega_0}{Q_0} U_{strd}(t), \tag{5.21}$$

where P is the input power of the cavity, and Eq. (5.6) is used for the power loss. Inserting Eq. (5.20) into Eq. (5.21) and solving the differential equation with the assumption $Q_0 \gg 1$ yields

$$U_{strd}(t) = P_{max} \frac{Q_0}{\omega_0} \left(1 - e^{-t/\tau}\right)^2, \tag{5.22}$$

---

[2]This definition of g only holds for a series RLC-network.
[3]This can be calculated by, e.g., calculating the power stored in the capacitance.

Table 5.1: *Qualitative effects of dimension changes of the cavity geometry depicted in Fig. 5.2. The symbols ↓ and ↑ indicate a decrease and an increase respectively, and 0 indicates no change.*

Geometry change	E_0	Q-factor	ω_0
increase width throat z_1	↓	↑	↑
increase height throat r_1	0	↓	↓
increase width top z_2	0	0	↓
increase height top r_2	0	↑	↓

where $\tau = Q_0/\omega_0$ is the so-called cavity filling time. If $t \gg \tau$ steady-state operation is reached and $U_{strd} = \frac{Q_0}{\omega_0} P_{max}$ as expected: the incoming power balances the dissipated power.

For our cavities with $f_0 = 3\,\text{GHz}$ and typically $Q = 8000$ the filling time is approximately $0.5\,\mu\text{s}$. At $t = 6\tau = 3\,\mu\text{s}$ more than 99% of the input power is stored in the cavity.

5.3 Power efficient cavity design

To sustain a RF field with a certain amplitude the pillbox cavity is generally not the most power efficient geometry. For example, considering the use of a $3\,\text{GHz}$ copper pillbox cavity for compression of electron bunches (as described in section 3.4) the required on-axis electric field strength of $4\,\text{MV/m}$ is sustained if the RF input power is $2.3\,\text{kW}$. This can be calculated using Eqs. (5.6), (5.7b), (5.9b), and (5.10), and it is in close agreement with SUPERFISH results.

The goal is that both the compression cavity and the streak cavity require less than $1\,\text{kW}$ RF power, which can be delivered by commercially available solid state amplifiers. A costly klystron is then not needed. At these power levels transport of the RF signal from the amplifier to the cavities can be done with coaxial cables, rather than an infrastructure of waveguides. This way the setup keeps relatively compact and affordable.

Power efficiency of a cavity can be improved by increasing the stored energy, decreasing the power loss, or a combination of these two. The stored energy is optimized by changing the geometry such that the field is concentrated at the region where the interaction with the electrons takes place. The power loss is minimized by changing the geometry such that the magnetic fields at the walls are reduced, thereby reducing induced currents that lead to Ohmic losses (see Eq. (5.9a)). Figure 5.2 shows a sketch of a geometry that basically fulfills these two conditions. The field is concentrated in the throat section and lowered in the top part. For this geometry analytical expressions of the field profile, resonant frequency, and Q-factor are not available and numerical Poisson solvers have to be used. For cylindrically symmetric field distributions SUPERFISH [6] is an established solver, while CST MWS [7] is an established 3D solver. With the aid of these solvers we have improved the cavity geometry for power efficiency.

First the influences of dimension changes on the Q-factor and the resonant frequency have been investigated. The qualitative results are summarized in Table 5.1.

Next the shape of the top part is changed. Assuming that the dissipating currents are uniform in the cavity wall, the Q-factor is maximum when the ratio of the volume of the
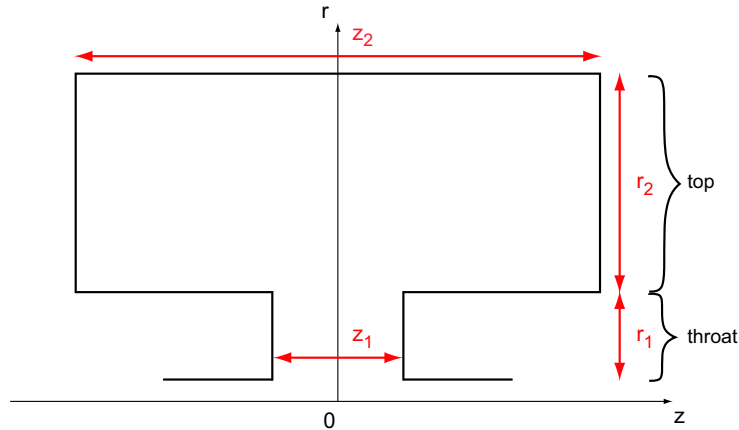
Figure 5.2: *Basic geometry of a more power efficient cavity that is used to investigate the influence of dimension changes on cavity parameters. The geometry is cylindrically symmetric around the z-axis.*

cavity to the area of its walls is maximum. Ideally the top part should thus be spherical. However, because of the throat this is impossible and a toroidal shape with an elliptical cross-section turns out to be optimal.

Finally, edges are rounded to prevent local field enhancement that could lead to breakdown. According to Kilpatrick's empirical formula [8] the maximum allowed field strength in a 3 GHz cavity is approximately 47 MV/m. The fields in our compression and streak cavity are substantially lower than this limit, so no breakdown is expected to occur if there are no local field enhancements.

With this basic, more power efficient geometry in mind the compression cavity and the streak cavity have been designed separately, as presented in Sec. 5.4 and Sec. 5.5 respectively.

5.4   Compression cavity

5.4.1   Design

Starting with the basic geometry presented in Sec. 5.3 a power efficient compression cavity is designed in accordance with the following criteria:

- TM_{010} mode with resonant frequency $f_0 = 2.9985$ GHz;

- Maximum power efficiency, i.e., maximum electric field strength for a given input power;

- On-axis apertures for entrance and exit of electron bunches. The apertures should have a minimal radius of 2 mm in order to avoid direct interaction between electrons and the cavity wall;

- Interaction length $\lesssim 5$ mm such that the linear slope of the sine-varying electric field is applied in time while the bunch is traveling through the interaction region.

The dimensions and a design drawing of the compression cavity are depicted in Fig. 5.3. We have used SUPERFISH [6] to calculate the resonant frequency, quality factor, and field strength at a given input power. The results are summarized in Table 5.2, together with the measured values. The SUPERFISH calculation of the on-axis field profile is shown in Fig. 5.4 together with the measured profile.

RF power is inductively coupled into the cavity with a rotatable loop antenna that is described in more detail in section 5.6.

5.4.2 Cavity machining

The cavity is made out of two OFHC copper (Outokumpu, ASTM C101000) half cells that are brazed to each other to make the cavity vacuum compatible. The cells are made with a single-point diamond turning technique with $1\,\mu$m precision. In case of an ideal pillbox cavity the resonant frequency would then deviate maximally $0.1\,$MHz, as calculated with equation (5.2).

To braze the cavity it is heated in an oven to a temperature of $750\,$°C. With the fabrication of the compression cavity it turned out that the resonant frequency before and after brazing differs $0.85\,$MHz. Apparently the heating and cooling during the brazing proces have a significant influence on the resonant frequency. There is, however, no influence on the on-axis field profile, which has also been measured before and after brazing.

5.4.3 Cavity characterization

First the antenna has been rotated to the position where the cavity impedance is purely real and equal to $(50.0 \pm 0.5)\,\Omega$ as measured with a network analyzer. This way the cavity and source impedances are matched, which is confirmed by a large power absorption ($> 35\,$dB) at the resonant frequency. The absorption as a function of frequency of the cavity has been determined with a reflection measurement: a network analyzer sends a low-power ($\sim 1\,$mW) RF signal into the cavity and measures the amplitude of the reflected signal as a function of the RF frequency. The result is shown in Fig. 5.5. Fitting the data to a Lorentz curve (see Eq. (5.18) with $g = 1$) yields $f_0 = 2.99943\,$GHz and $Q_0 = 8290$, as summarized in Table 5.2 together with the SUPERFISH results. The measured resonant frequency is $0.62\,$MHz higher than calculated with SUPERFISH. This is a result of the brazing process, which is necessary to make the cavity vacuum compatible. Before brazing the resonant frequency was $2.99858\,$GHz, which is in close agreement with the SUPERFISH result.

When driving the cavity at its resonant frequency the electric field amplitude is proportional to the square root of the Q-factor (see Eq. (5.6)). Combining the SUPERFISH results and the measured Q_0 it is calculated that $E_0 = 9.73\,$MV/m when the cavity is driven with $1\,$kW power.

Another characteristic of a cavity is its on-axis field profile. For a cavity with a cylindrically symmetric field distribution the components of the EM field near the z-axis can be approximated by a power series in the radial coordinate r. When substituting these power series into Maxwell's equations it follows that all field components are determined if the on-axis EM field is known. Therefore, measuring the on-axis field is sufficient to check the
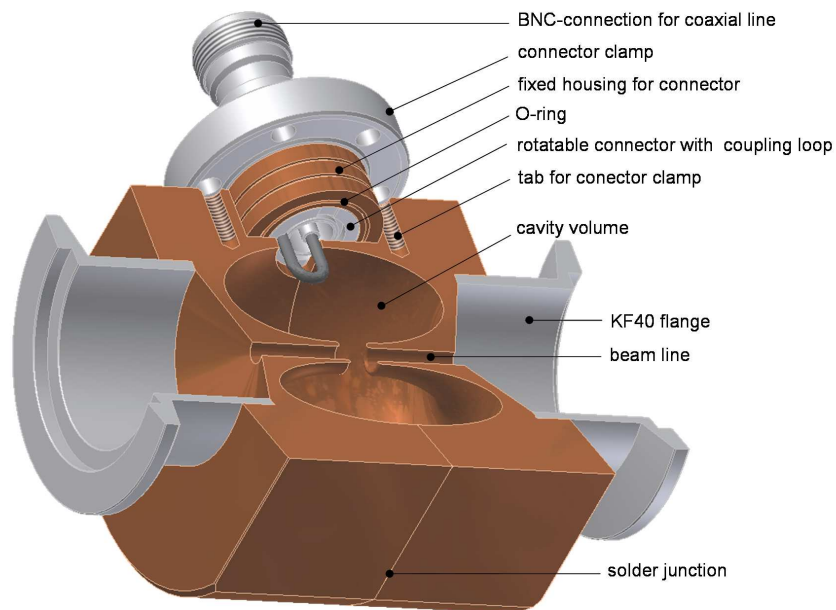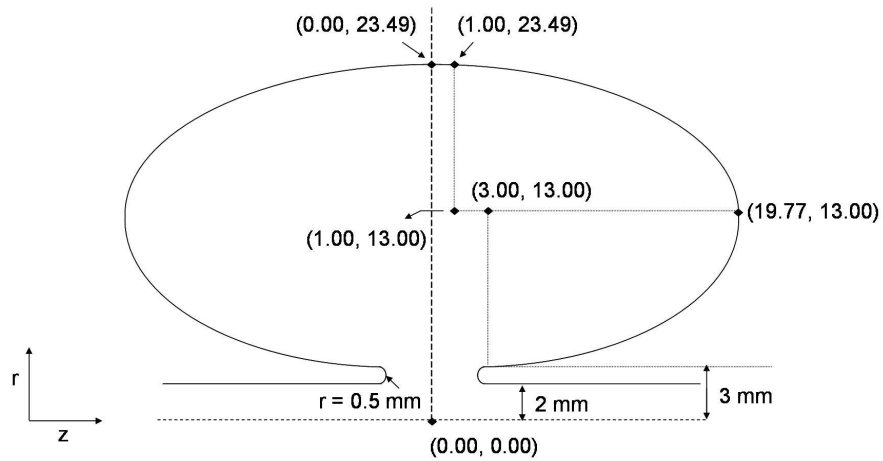
Figure 5.3: *(top) Cross-section of the compression cavity. The z-axis is the axis of cylindrical symmetry. The dimensions of the compression cavity are shown; the numbers between brackets are coordinates (z, r) in* mm. *(bottom) Design drawing of the compression cavity. The coupling loop is rotatable by* $90°$ *to be able to position it such that all incoming power is dissipated into the cavity, i.e., such that impedance matching is established.*
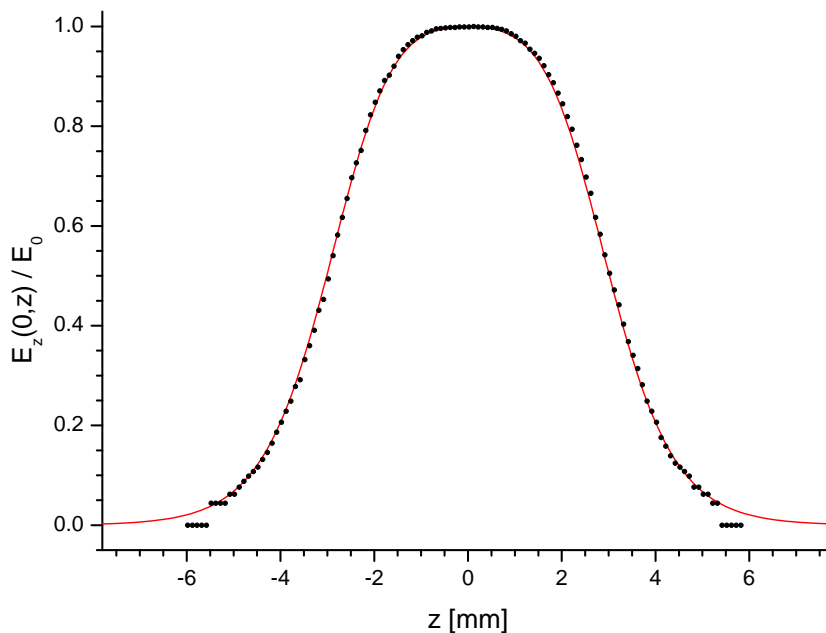
Figure 5.4: *On-axis electric field profile of the compression cavity as calculated with* SU-PERFISH *(solid line) and as measured with the perturbation method (dots). The measurement error is very small and can be neglected. Therefore it is not shown. At $|z| \gtrsim 5\,\mathrm{mm}$ the resolution of the network analyzer is reached, i.e., the frequency shift can not be resolved and a digitalization error becomes apparent.*
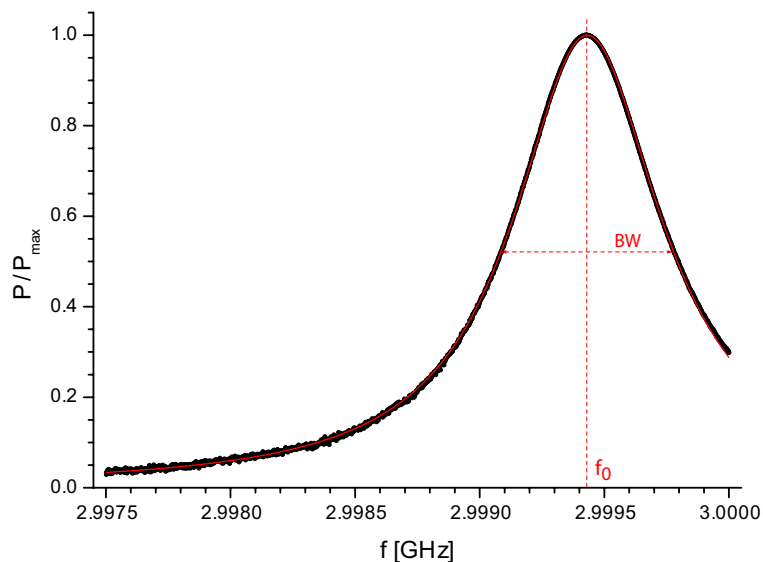
Figure 5.5: *Power absorption of the compression cavity as a function of frequency, measured at a surrounding temperature $T = (21.5 \pm 0.5)\,^{\circ}\mathrm{C}$. The absorbed power is normalized to the maximally absorbed power at the resonant frequency. The measurements (dots) are fitted to a Lorentz curve (solid line), yielding $f_0 = 2.99943\,\mathrm{GHz}$, and $BW = 723\,\mathrm{kHz}$.*

Table 5.2: *Properties of the compression cavity as calculated with* SUPERFISH *(T =*
20.0 °C) and as measured with a reflection measurement under vacuum conditions at a
surrounding temperature T = (21.5 ± 0.5) °C.

Parameter	SUPERFISH	Measured (after soldering)
f_0 [MHz]	2998.81	2999.43
$Q_0 = 2Q_l$	9135	8290 ± 10
BW [kHz]	657	723 ± 1
E_0 [MV/m] @ $P = 1\,\mathrm{kW}$	10.21	9.73 ± 0.01

consistency of the actual EM field with simulation results. The on-axis field profile can be measured with the perturbation method described in Ref. [9]. Placing a small bead inside the cavity causes a local field disturbance resulting in a slight shift $\Delta\omega$ of the resonant frequency given by

$$\frac{\Delta\omega}{\omega_0} = -\frac{3\epsilon_0 \Delta V_b}{4U_{strd}} \left(\frac{\epsilon_r - 1}{\epsilon_r + 2} E^2 + \frac{\mu_r - 1}{\mu_r + 2} B^2 c^2 \right). \tag{5.23}$$

Here E and B are the unperturbed electric and magnetic fields strength at the position of the bead, ε_0 is the permittivity of vacuum, and ε_r and μ_r are the relative permittivity and permeability of the bead. The total energy U_{strd} stored in the cavity, and the volume ΔV_b of the bead are generally not known accurately. However, for the field profile $E \propto \sqrt{\Delta\omega/\omega_0}$ a relative measurement will suffice. Depending on the choice of the bead material this perturbation method is more sensitive to either the electric or the magnetic field.

To measure the on-axis electric field profile of the compression cavity a solder bead was used with a diameter $< 1\,\mathrm{mm}$, glued onto a $50\,\mu\mathrm{m}$ thin fishing wire to guide it through the cavity. The frequency shift was measured with a network analyzer as a function of bead position. The resulting field profile $E_z(z)/E_0$ is shown in Fig. 5.4 together with the profile calculated by SUPERFISH. The measured and calculated field profile are consistent. At the apertures, i.e., at $|z| \gtrsim 5\,\mathrm{mm}$, the resolution limit is reached because of the low electric field strength. Using a larger bead would increase the perturbation such that lower field strengths could be measured. However, in that case the uncertainty in position accuracy of the bead would increase.

5.5 Streak cavity

5.5.1 Design

The streak cavity is used together with the compression cavity in the same setup (see Fig. 6.3). To ensure that the phases of both cavities are locked to each other, the cavities have to be driven at the same frequency, and preferably by the same RF source. For maximum power absorption the cavities should therefore have exactly the same resonant frequency. However, a slight deviation can be allowed depending on absorption requirements. For example, allowing 10% reflection requires a frequency difference of maximally 0.1 MHz between the two cavities,

assuming they have a bandwith of 300 kHz. Other requirements on the design of the streak cavity are:

- TM_{110} mode with resonant frequency tunable to that of the compression cavity;

- A magnetic field amplitude $B_0 = 8$ mT at less than 1 kW input power, in order to have 100 fs resolution for bunch length measurements (see Sec. 6.4);

- On-axis apertures for entrance and exit of electron bunches. The apertures should have a minimal radius of 2 mm in order to avoid direct interaction between electrons and the cavity wall;

- Interaction length such that the transit time of 100 keV electrons equals half the time period of the RF field. This is to maximize the deflection of the electrons.

When fabricating the compression cavity it turned out that the resonant frequency changes during brazing, see Sec. 5.4.2. Therefore in the fabrication process of the streak cavity an extra step is included. Before the final, most accurate lathing step, the cavity was heated and thus annealed to prevent or at least decrease the frequency change due to heating in the brazing process. The idea of this extra step is that stresses in the material could relax without changing the resonant frequency. Indeed, the resonant frequency of the streak cavity had increased only 0.1 MHz after brazing. The annealing before the final lathing step thus seems to be a proper way to avoid changes in the resonant frequency due to brazing.

To be absolutely sure that the resonant frequency of the streak cavity can be tuned to that of the compression cavity a tuning plunger was added, which is described in more detail in Sec. 5.5.3. Simulations have indicated that the plunger does not significantly influence the electro-magnetic field profile near the z-axis.

A design drawing of the streak cavity is shown in Fig. 5.6. The resonant frequency, quality factor, and field strength at a given input power have been calculated with MWS [7]. The results are summarized in Table 5.3 together with the measured values. The MWS calculation of the on-axis field profile is shown in Fig. 5.7 together with the measured profile.

RF power is inductively coupled into the cavity with a rotatable loop antenna that is described in more detail in Sec. 5.6.

5.5.2   Characterization

With a reflection measurement the resonant frequency of the streak cavity, without tuning stub, was measured to be $f_0 = 2.9979$ GHz before brazing. This deviates only very little from the expected value from MWS simulations. After brazing the resonant frequency had increased by only 0.1 MHz.

Next, the tuning stub was inserted into the cavity to the extent necessary to match its resonant frequency with that of the compression cavity. Measuring the absorption with a network analyzer gives the result shown in Fig. 5.8. Fitting the data to a Lorentzian yields $f_0 = 2.99945$ GHz and $Q_0 = 8680$. The difference between the resonant frequency of the compression cavity and the streak cavity is thus only 20 kHz, which is about a tenth of the
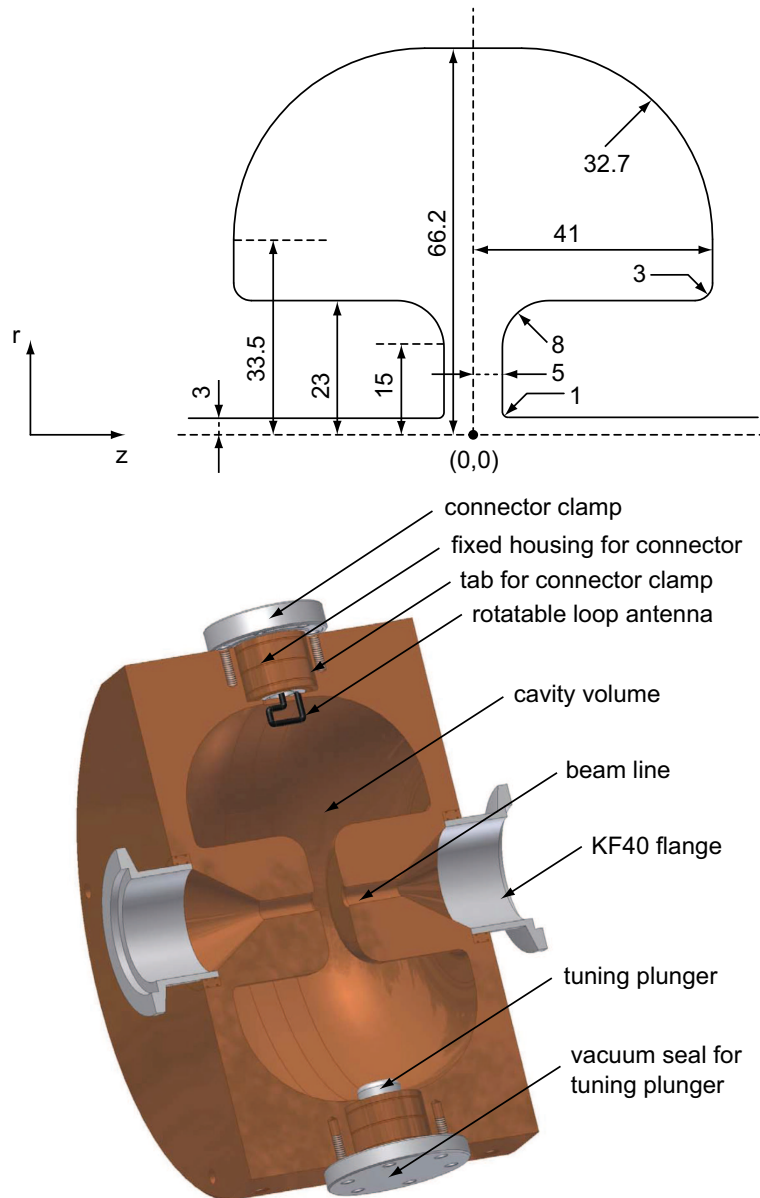
Figure 5.6: *(top) Cross-section of the streak cavity. The z-axis is the axis of cylindrical symmetry. The dimensions are shown in* mm*; a number at an arc is the corresponding radius of curvature in* mm*. (bottom) Design drawing of the streak cavity. The coupling loop is rotatable* 90° *around the radial axis to be able to position it such that all incoming power is dissipated in the cavity, i.e., such that impedance matching is established. A tuning stub can protrude into the cavity to change the resonant frequency, as shown in Fig. 5.9.*
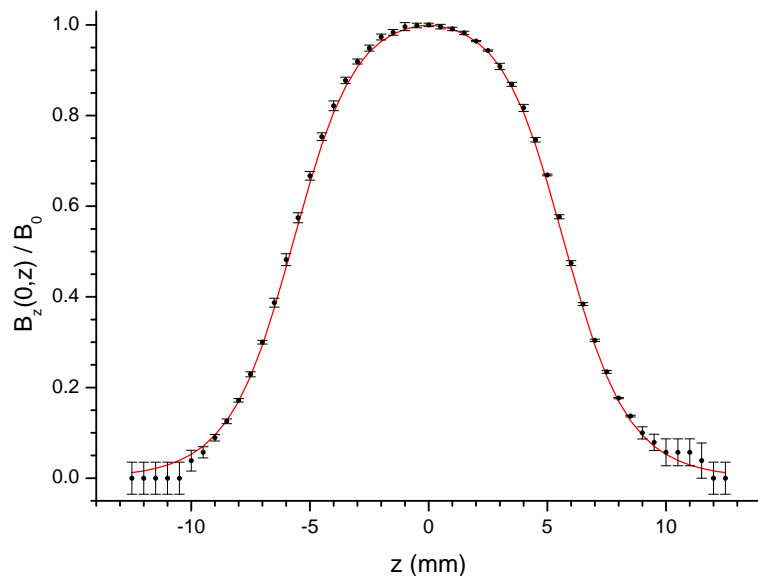
Figure 5.7: *On-axis magnetic field profile of the streak cavity as calculated with MWS (solid line) and as measured with the perturbation method (dots). At $|z| \gtrsim 9\,\mathrm{mm}$ the resolution of the network analyzer is reached, i.e., the frequency shift can not be resolved.*
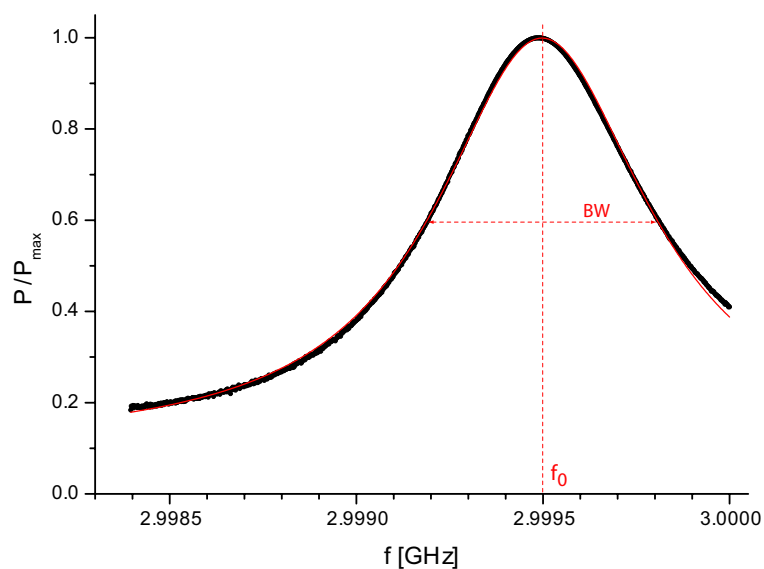
Figure 5.8: *Power absorption of the streak cavity as a function of frequency, measured at a surrounding temperature $T = (21.5 \pm 0.5)\,^{\circ}\mathrm{C}$. The absorbed power is normalized to the maximal absorbed power at the resonant frequency. The measurements (dots) are fitted to a Lorentz curve (solid line), yielding $f_0 = 2.9995\,\mathrm{GHz}$, and $BW = 691\,\mathrm{kHz}$.*

Table 5.3: *Properties of the streak cavity as calculated with MWS(at $T = 25.0\,°C$) and as measured (after soldering, with tuning plunger) with a reflection measurement under vacuum conditions at a surrounding temperature $T = (21.5 \pm 0.5)\,°C$.*

Parameter	MWS	Measured
f_0 [MHz]	2997.94	2999.5
$Q_0 = 2Q_l$	11790	8680 ± 20
BW [kHz]	509	691 ± 1
B_0 [mT] @ $P = 1\,kW$	8.68	7.45 ± 0.02

bandwidth. The values of the characteristic parameters of the streak cavity are summarized in table 5.3.

Using the bead-perturbation method, as described in Sec. 5.4.3, the on-axis magnetic field profile $B_y(z)/B_0$ was measured. Instead of a solder bead, however, a ferromagnetic (iron) bead was used, which is more sensitive to the magnetic field. The measured profile is shown in Fig. 5.7 together with the profile calculated using MWS. As is the case with the compression cavity the measured and simulated field profiles are consistent, except at $|z| \gtrsim 9\,mm$ where the measurement is less accurate because of the small field strengths.

5.5.3 Cavity tuning

Figure 5.9 shows the frequency shift as a function of the length L_p the plunger protrudes into the streak cavity. Because of some solder leaking into the screw thread during brazing, the plunger can only be moved over a short range. Therefore three plungers of different lengths were used. The plunger position $L_p = 0$, corresponding to the point where the plunger just enters the cavity, is known with an accuracy $\leq 1\,mm$. The plunger has a diameter of $14\,mm$ and can be moved into the cavity up to $L_p = 10\,mm$, which allows tuning over a comfortable $1.5\,MHz$.

5.6 Antenna: magnetic coupling

In both cavities the antenna is a small copper loop wire, inserted into the cavity through a hole that enables rotation of the antenna, as shown in Fig. 5.10. A $3\,GHz$ radio-frequency current through the wire generates a varying magnetic field through the loop. Depending on the geometry of the cavity a certain mode is excited (TM_{010} in case of the compression cavity and TM_{110} in case of the streak cavity). By rotating the antenna, the magnetic flux can be changed. This way the absorption of the cavity can be optimized, or in other words impedance matching can be obtained. This can be seen with lumped element modeling, by considering the interaction of the loop with the cavity as a perfect transformer. The loop antenna is the primary coil, consisting of one turn, and the cavity is seen as the secondary coil with an unknown amount of turns n. Applying energy conservation to the lumped element circuit described in Sec. 5.2, but with a perfect transformer between the source and the RLC-circuit, yields $Z = n^2 R_g$. Thus impedance matching is obtained when $n^2 R_g = R$, where n can be tuned by rotating the loop antenna.
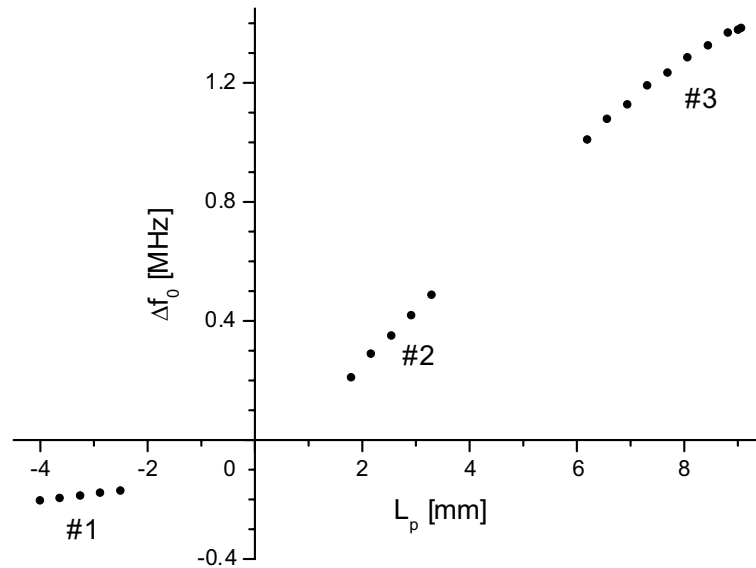
Figure 5.9: *Resonant frequency shift of the streak cavity as a function of the protrusion L_p of a tuning plunger. Three plungers of different lengths are used as indicated by the numbers in the graph.*
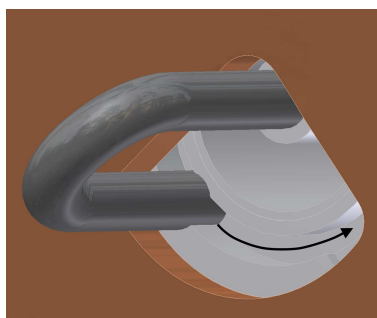
Figure 5.10: *Loop antenna inserted into a cavity through a small hole in the wall. The antenna inductively couples RF power from the coaxial transmission line into the cavity. The antenna can be rotated maximally 90° to obtain impedance matching. (The antenna wire is copper, but colored black in this figure for clarity.)*

5.7 High power cavity operation

5.7.1 RF setup

The RF setup is schematically shown in Fig. 5.11. The RF source is a voltage controlled oscillator (VCO) that is tunable within the range of $f = (2998.5 \pm 1.5)\,\mathrm{MHz}$. Its output power is $10\,\mathrm{mW}$. It operates in a pulsed mode, where external triggering with a TTL pulse control allows generation of pulses on demand. In our setup the repetition rate is $5\,\mathrm{Hz}$ and the pulses have a width of $100\,\mu\mathrm{s}$. The output of the VCO is first pre-amplified and then split 50:50. One signal is transmitted via a trombone phase shifter to the input of a $200\,\mathrm{W}$ RF amplifier (MAL [10], AM83-3S-50-53). Its output is used to drive the compression cavity. The other output of the 50:50 splitter goes to a $1\,\mathrm{kW}$ RF solid state amplifier[4] (MAL [10], AM84-3S2-50-60R). In the transmission line to the streak cavity a phase shifter is included.

Before switching on either amplifier the frequency of the VCO is tuned[5] to match the RF frequency to the resonant frequency of the cavities. Then the amplifiers are switched on and the frequency is fine-tuned by minimizing the reflected power of the streak cavity[6]. In the transmission lines to both cavities a directional coupler picks up a small fraction of the forward and the reflected power. These powers are measured with calibrated diodes and are used to determine the power absorbed by the cavity. Using the numbers from the characterization measurements, see Tables 5.2 and 5.3, the field amplitudes E_0 and B_0 can be calculated.

As expected no breakdown occurs in either cavity when driving at a maximum power of $850\,\mathrm{W}$.

5.7.2 Thermal effects

Temperature changes will lead to expansion (or contraction) of a cavity resulting in a change of the resonant frequency. Using the thermal expansion coefficient $k_{\mathrm{T}} = \frac{1}{R}\frac{dR}{dT}$ the frequency shift of a pillbox cavity oscillating in the $\mathrm{TM}_{\mathrm{mn0}}$ mode is given by

$$\frac{\partial f}{\partial T} = \frac{-x_{mn}}{2\pi\sqrt{\varepsilon\mu}}\frac{1}{R}\frac{dR}{dT} = -f_0\kappa_{\mathrm{T}}. \tag{5.24}$$

For copper $\kappa_{\mathrm{T}} = 16.4 \cdot 10^{-6}\,\mathrm{K}^{-1}$ [5] leading to a frequency shift $\frac{\partial f}{\partial T} = -51\,\mathrm{kHz/K}$ for a $3\,\mathrm{GHz}$ pillbox cavity.

When driving the compression cavity with $10\,\mu\mathrm{s}$ pulses of $8.4\,\mathrm{mJ}$ at a repetition rate of $1\,\mathrm{kHz}$ a frequency drop has been observed. However, in our experiments, where we used a repetition rate of $5\,\mathrm{Hz}$, no considerable frequency change occurred, not even when stretching the pulse length to $100\,\mu\mathrm{s}$.

A change of the resonant frequency (while the frequency of the driving RF source remains unaltered) has two main consequences:

---

[4]Testing shows that the maximum output power of this amplifier actually is $850\,\mathrm{W}$.

[5]This can be done by changing the repetition rate of the Mantis oscillator, see Sec. 5.8.

[6]The cavities do not have exactly the same resonant frequency. In our experiments the maximum field strength to be obtained, and thus the power absorbance, is more critical for the streak cavity then for the compression cavity.

1. Less power absorption by the cavity (see Sec. 5.2) leading to a lower field amplitude;

2. A phase shift of the EM field in the cavity with respect to the RF input.

The phase shift is given by

$$\frac{\partial \varphi}{\partial T} = \frac{\partial \varphi}{\partial f} \frac{\partial f}{\partial T}. \tag{5.25}$$

From the complex impedance of a cavity (given by Eq. (5.13b)) it follows that $\frac{\partial \varphi}{\partial f} = \frac{2Q_0}{f_0}$, with f_0 the resonant frequency of the unperturbed cavity. Inserting this result and Eq. (5.24) into Eq. (5.25) yields for the phase shift of a pillbox cavity

$$\frac{\partial \varphi}{\partial T} = -2Q_0 \kappa_T \tag{5.26}$$

For an actual copper cavity with typically $Q_0 = 8000$ the phase stability is approximately $0.27 \, \mathrm{rad/K}$. Temperature changes could possibly lead to a drift of the RF phase offset with respect to the laser pulses. Temperature induced phase jitter is not expected because that would require fast temperature changes. Most importantly however, is that we have not noticed any temperature influences during our experiments.

5.8 Synchronization and timing

A schematic of the timing and synchronization is shown in Fig. 5.11. The Ti:Sapphire laser oscillator (Mantis, see Sec. 4.1.1) serves as the master clock of the setup in two ways: for synchronization of the phase of the $3 \, \mathrm{GHz}$ RF signal, and for the timing of trigger pulses for several components.

5.8.1 Synchronization

In order to inject an electron bunch on the desired phase of the RF field in a cavity the phase has to be synchronized to the femtosecond laser pulse that generates the bunch. This is done with $18 \, \mathrm{fs}$ precision with a Phase Locked Loop (PLL) synchronization system: the frequency of a voltage controlled oscillator (VCO) is continuously adapted to zero the phase difference with the laser oscillator (Mantis, see section 4.1.1). This synchronization system is described in more detail in Ref. [11]. By changing the repetition frequency of the laser the frequency of the VCO can thus be tuned to match the resonant frequency of a cavity. The bandwidth of the VCO ranges from 2.9970 to 3.0000 GHz, which is fully covered by the Mantis.

5.8.2 Timing

A timing delay unit (TDU) has been built to generate synchronized TTL pulse trains. The working of the TDU is based on counters. Because the Mantis serves as a clock for the TDU, the timing and the TTL pulse length are adjustable with a stepsize of $f_{osc}^{-1} = 13.3 \, \mathrm{ns}$. A $1 \, \mathrm{kHz}$ TTL pulse train from the TDU is used to trigger the Q-switch of the pump laser (Evolution
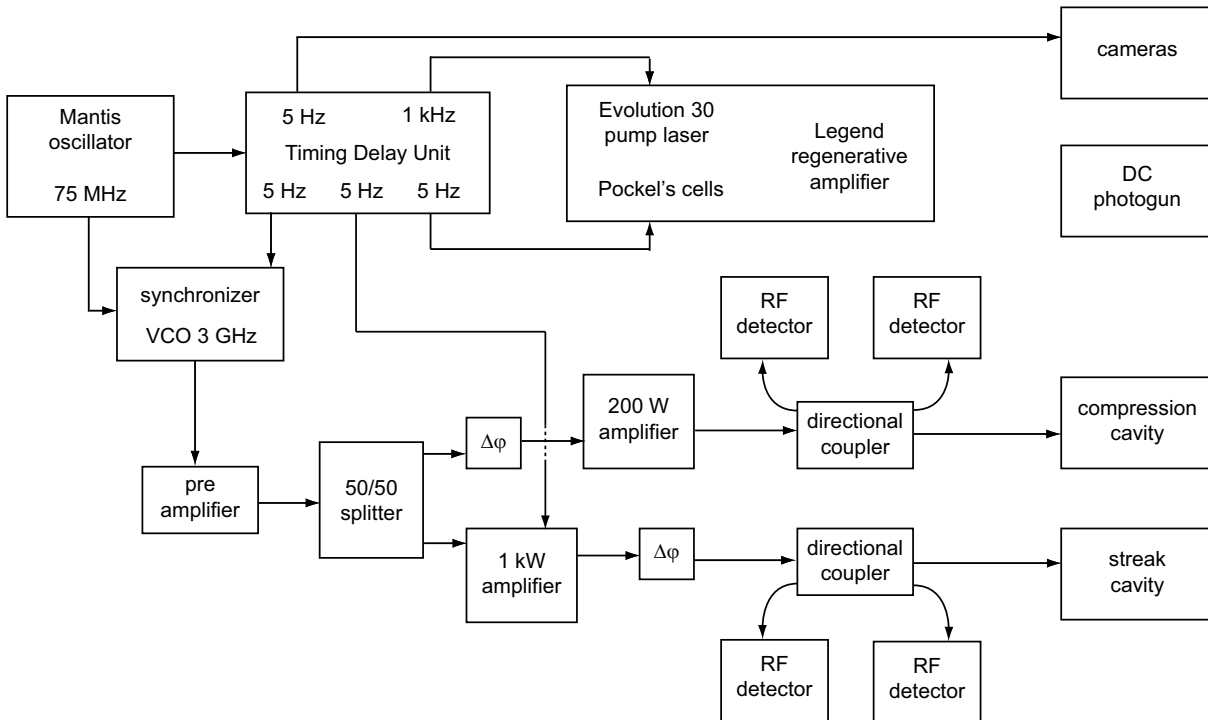
Figure 5.11: *Schematic overview of the RF setup, including timing and synchronization.*

30, see Sec. 4.1.1) of the regenerative Ti:Sapphire amplifier. A 5 Hz signal is used to trigger the two Pockels cells that are switched to let a pulse from the oscillator enter the regenerative cavity and to couple the amplified pulse out of the cavity.

Another 5 Hz TTL pulse triggers several CCD cameras that visualize the laser spot (see Sec. 4.1.3), and that capture the light from a phosphor screen being hit with electrons (see Sec. 7.5.3). By properly timing the triggers it is ensured that the cameras capture images of single pulses. Further, by choosing a proper trigger pulse duration the integration time of the cameras is minimized, thereby reducing the background noise.

A third 5 Hz signal is used to switch the output of the VCO (in the synchronizer) and to switch the 1 kW amplifier that drives the streak cavity.[7] Proper timing ensures that the fields in the compression cavity and streak cavity have been built up when an electron bunch arrives.

---

[7]The 200 W amplifier that drives the compression cavity can operate in continuous mode. The output, however, is pulsed because of the pulsed seed signal from the VCO.

References

[1] F. B. Kiewiet, *Generation of ultrashort, high-brightness relativistic electron bunches*, PhD thesis, Technische Universiteit Eindhoven, 2003.

[2] W. P. E. M. Op 't Root, *Generation of high-field, single-cycle terahertz pulses using relativistic electron bunches*, PhD thesis, Technische Universiteit Eindhoven, 2009.

[3] J. Daniëls, Dielectrics in RF cavities, Master thesis, Technische Universiteit Eindhoven, 2009.

[4] D. M. Pozar, *Microwave Engineering*, John Wiley & Sons, Inc., 2005.

[5] Handbook of Chemistry and Physics, `http://www.hbcpnetbase.com`.

[6] J.H. Billen, and L.M. Young, Poisson Superfish.

[7] CST Microwave Studio, CST GmbH, Germany.

[8] W. Kilpatrick, Rev. Sci. Instrum. **28**, 824 (1957).

[9] L. C. Maier, and J. C. Slater, J. Appl. Phys. **23**, 68 (1952).

[10] Microwave Amplifiers Ltd, `http://www.maltd.com`.

[11] F. B. Kiewiet, A. H. Kemper, O. J. Luiten, G. J. H. Brussaard, and M. J. van der Wiel, Nucl. Instrum. Methods A **484**, 619 (2002).

6

Compression of sub-relativistic space-charge-dominated electron bunches for single-shot femtosecond electron diffraction

This chapter is an adapted version of the article by T. van Oudheusden, P. L. E. M. Pasmans, S. B. van der Geer, M. J. de Loos, M. J. van der Wiel, and O. J. Luiten, submitted to *Phys. Rev. Lett.* and available at *arXiv* [1].

6.1 Introduction

The breathtaking pace at which ultrafast X-ray and electron science have evolved over the past decade is presently culminating in studies of structural dynamics with both atomic spatial *and* temporal resolution, i.e. sub-nm and sub-100 fs [2, 3, 4]. This may revolutionize (bio-)chemistry, and material science and might open up vast new areas of research. In particular, in 2009 the first hard X-ray free electron laser (LCLS) has become operational [4]. This has already resulted in X-ray diffraction experiments on sub-micron crystals of a membrane protein [5]. Over the past few years ultrafast electron diffraction (UED) techniques have been successfully applied to investigate condensed matter phase transitions dynamics at the atomic spatio-temporal scale [6, 7, 8, 9]. X-ray diffraction and electron diffraction provide principally different, but in fact complementary, information of atomic structure. Because of their shorter mean free path, however, electrons are favorable for probing thin films, surfaces, or gases. Unfortunately, single-shot, femtosecond operation has not yet been achieved with electrons: because of the repulsive Coulomb force high-space-charge-density bunches will expand rapidly in all directions. To solve this problem the paradigm in the high-brightness electron beam community is to accelerate the electrons to relativistic velocities as quickly as possible. Special relativity dictates that the Coulomb force is then effectively damped, resulting in a slower bunch expansion. Although it has been shown that relativistic bunches can be used for UED [10] they pose difficulties like a reduced cross-section, radiation damage to samples, non-standard detectors, and general expense of technology. However, at the preferred electron energies of $100 - 300$ keV [11] the bunch charge required for single-shot UED results inevitably in loss of temporal resolution. The obvious solution is to lower the charge per bunch [3, 6, 7] and use multiple shots to obtain a diffraction pattern of sufficient

quality. However, in this way the choice of samples is restricted for reasons of radiation damage and repeatability of the process under investigation. Following this strategy, the closest to single-shot, femtosecond operation has been achieved by Sciaini et al., who used $\sim 0.001\,\mathrm{pC}$ bunches and integrated 4-12 shots per time point to monitor electronically driven atomic motions of Bi [7]. By positioning the sample at $3\,\mathrm{cm}$ from the photocathode they achieved $350\,\mathrm{fs}$ resolution. Preferably, however, the bunch charge should be $\gtrsim 0.1\,\mathrm{pC}$, in particular for UED on more complicated molecular crystals, while maintaining a high beam quality and $\lesssim 100\,\mathrm{fs}$ resolution.

In this Letter we demonstrate 100-fold compression of $0.25\,\mathrm{pC}$ electron bunches to sub-$100\,\mathrm{fs}$ durations, see Fig. 6.1. To show that these bunches are of sufficient quality for single-shot UED we have used a single bunch to record the diffraction pattern of a polycrystalline gold foil, as shown Fig. 6.2.

6.2   Electron bunch considerations

The quality of a diffraction pattern is mainly determined by the transverse coherence length $L_\perp$ of the electron bunch, defined as $L_\perp = \lambda/(2\pi\sigma_\theta)$, where λ is the electron De Broglie wavelength, and σ_θ the transverse root-mean-square (RMS) angular spread of the electrons. The transverse coherence length should preferably be larger than the lattice spacing, implying $L_\perp \gtrsim 1\,\mathrm{nm}$ (see Sec. 7.5.2). Further, the transverse RMS bunch size should preferably be matched to the sample size, which is often limited by sample preparation techniques to $\lesssim 100\,\mu\mathrm{m}$. When creating the electron bunch by photoemission the combination of the requirements on $L_\perp$ and spotsize dictates that the RMS radius of the laser at the photocathode should be smaller than $50\,\mu\mathrm{m}$ [11]. For a high quality diffraction pattern at least $0.1\,\mathrm{pC}$ ($\sim 10^6$ electrons) is required. When extracting such a charge from a cathode, using a femtosecond laser pulse with the required $50\,\mu\mathrm{m}$ RMS spotsize, a pancake of electrons is created of which the dynamics are dominated by, generally nonlinear, space-charge forces. As a result the bunch will not only expand rapidly, but it will also deteriorate: the RMS angular spread (measured in the beam waist) will increase, leading to a smaller $L_\perp$. By carefully shaping the transverse intensity profile of the photoemission laser pulse an ellipsoidal bunch can be created [12], with linear correlations between the velocities and the positions of the electrons [13]. The expansion of such a bunch is fully reversible with linear charged particle optics, i.e. the transverse coherence length is not affected by space-charge forces. To reverse the longitudinal bunch expansion we use radio-frequency (RF) techniques, as we proposed in Ref. [11].

6.3   Experimental setup

Our setup is schematically shown in Fig. 6.3 and is described in more detail in Ch. 3, 4, and 5. A (pancake-like) bunch, containing $\geq 10^6$ electrons, is liberated from a copper cathode by photoemission with the third harmonic of a 50 fs, 800 nm Ti:Sapphire laser pulse. The transverse laser profile is Gaussian with a $200\,\mu\mathrm{m}$ waist, concentrically truncated by a $200\,\mu\mathrm{m}$ diameter pinhole. The RMS spotsize of the resulting dome-shaped intensity profile
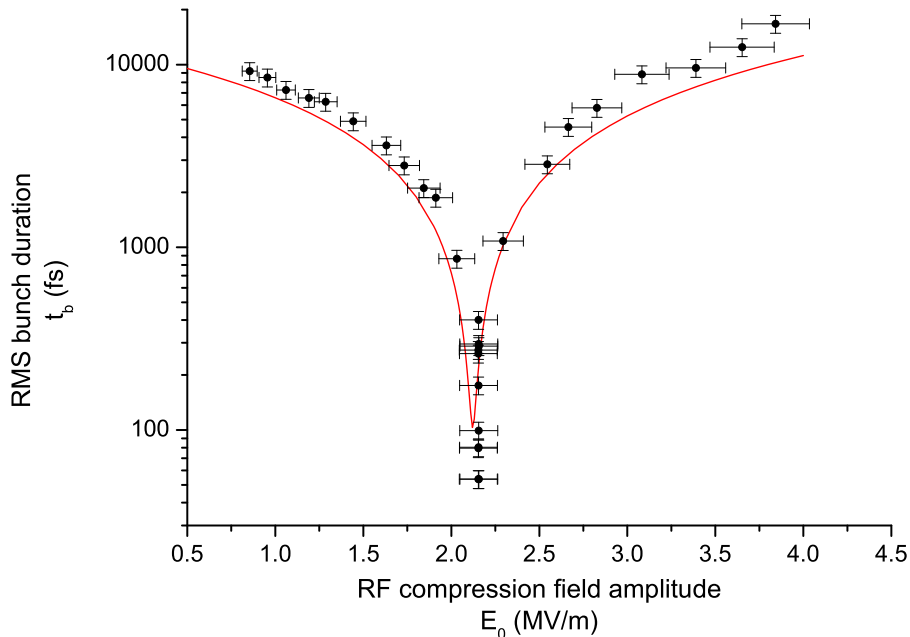
Figure 6.1: *RMS duration t_b of 95.0 keV, 250 fC electron bunches as a function of the RF compression field amplitude E_0. GPT simulations (solid line) are in close agreement with the measurements (dots).*

is approximately 50 μm. This initial distribution has been demonstrated to evolve into an ellipsoidal bunch [14, 15].

After photoemission the rapidly expanding electron bunch is accelerated in a DC electric field to an energy of 95.0 keV. Two solenoids control the transverse bunch size, as illustrated in Fig. 6.3. The first one focuses the bunch through the RF compression cavity and the second one is used to obtain the desired spotsize at the sample. To compress the bunch in the longitudinal direction we use a 3 GHz RF cavity oscillating in the TM_{010} mode. The RF phase offset is synchronized in such a way that the on-axis longitudinal electrical field $E_z(t)$ inside the cavity decelerates the electrons at the front of the bunch and accelerates the electrons at the back of the bunch, leading to velocity bunching in the subsequent drift space. The required amplitude of the RF electric field for maximum compression is 2.2 MV/m, see Fig. 6.1, which is achieved by driving our power efficient cavity with 51 W RF power.

To measure the bunch length we use another power efficient 3 GHz RF cavity, oscillating in the TM_{110} mode, which acts as an ultrafast streak camera (see Sec. 5.5 and Ref. [16]): the on-axis magnetic field $B_y(t)$ deflects the electrons in the x-direction. The RF phase offset is chosen such that the electrons at the center of the bunch are not deflected. In this way the longitudinal bunch profile is projected as a streak on the xy-plane. For detection we use a micro-channel plate (MCP) with a phosphor screen that is imaged 1:1 onto a CCD camera. The relation between the bunch duration t_b and the length X_{str} of the streak on the phosphor screen is obtained by integrating the Lorentz force that is acting on the electron bunch during its travel along the axis through the streak cavity. For bunch durations t_b much smaller than the RF period it follows that
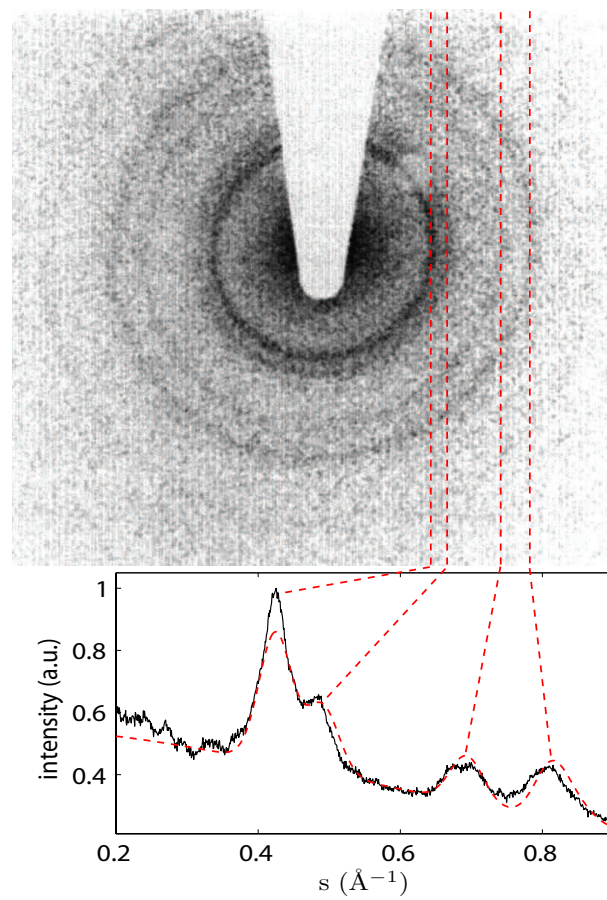
Figure 6.2: *(top) Electron diffraction pattern of a polycrystalline gold foil, recorded with a single 200 fC bunch. (bottom) Azimuthal integration (solid line) of the Debye-Scherrer rings in the top panel, and a fit (dashed line) based on kinematical diffraction theory.*
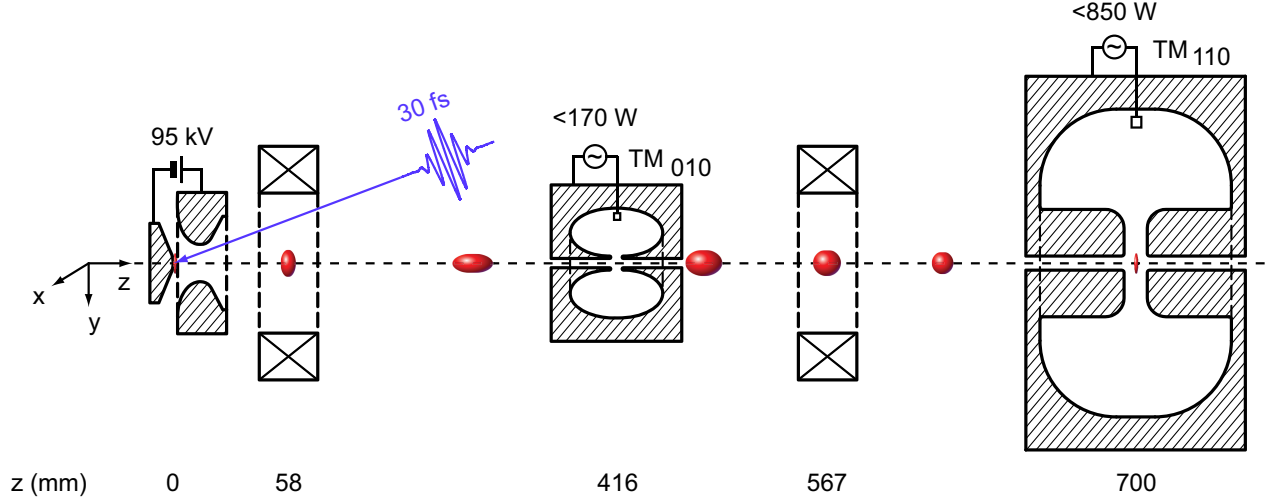
Figure 6.3: *Schematic of the setup and bunch evolution as it propagates through the beamline.*

$$t_b = \mathcal{C} \frac{X_{str}}{B_0}. \tag{6.1}$$

Here B_0 is the maximum amplitude of the magnetic field and $\mathcal{C} = \gamma m v / (2\pi f_0 e d_{cav} L_{scr})$, with e the elementary charge, m the electron mass, $\gamma = \left[1 - (v^2/c^2)\right]^{-1/2}$ the Lorentz factor, with v the speed of the electrons and c the speed of light, L_{scr} the distance from the exit of the streak cavity to the MCP, and $f_0 = 3\,\mathrm{GHz}$ the resonant frequency of the cavity. The effective cavity length is given by $d_{cav} = \int_{-\infty}^{\infty} b(z) \cos\left(\frac{2\pi f_0 z}{v}\right) dz$, where $b(z) = B_y(z)/B_0$ is the on-axis field profile of the cavity, which is known accurately from both simulations and measurements (see Fig. 5.7). For our setup $\mathcal{C} = (0.90 \pm 0.01)\,10^{-11}\,\mathrm{s\,T\,m^{-1}}$. As an independent check we have measured the position x_{scr} of the streak on the screen as a function of the RF phase offset, which is equivalent to a change in arrival time. The results for various values of B_0 are shown in Fig. 6.4. The slope of the linear fit to all data yields $\mathcal{C} = (1.06 \pm 0.07)\,10^{-11}\,\mathrm{s\,T\,m^{-1}}$, in satisfactory agreement with the result above.

6.4   Bunch compression measurements

In Fig. 6.5 streaks of a non-compressed and a maximally compressed $0.25\,\mathrm{pC}$ bunch are shown. Due to the streaking action the distribution on the MCP is a convolution of the transverse and the longitudinal bunch profile. For Gaussian distributions the RMS width of the intensity profile on the MCP is thus given by $\sigma_{\mathrm{MCP}} = \sqrt{\sigma_x^2 + X_{str}^2}$, where σ_x is the RMS size of the bunch in the x-direction on the MCP when the streak cavity is turned off. The transverse beam size of the bunch thus limits the resolution of the bunch length measurement. To increase the resolution we have placed a $10\,\mu\mathrm{m}$ slit at $7\,\mathrm{cm}$ in front of the center of the streak cavity to bring down the spotsize σ_x.

The width of the streak on the MCP is determined by summing five images and integrating the resulting image in the y-direction to increase the signal-to-noise ratio. The intensity
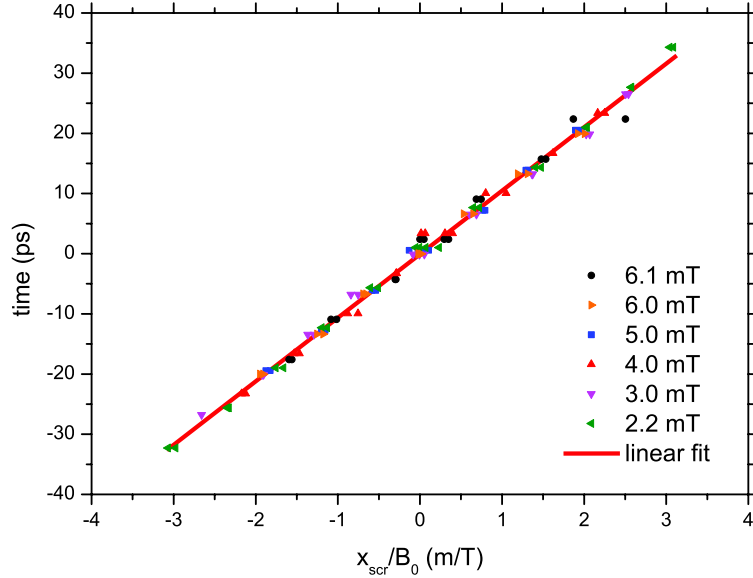
Figure 6.4: *Time delay as a function of x_{scr}/B_0. The red line is a linear fit to the data. The thickness of the red line reflects the confidence bounds of the fit.*

profile thus obtained is fitted to a Gaussian, yielding σ_{MCP}. For streak lengths $X_{str} \approx \sigma_x$ we adopted a different procedure: single images are analyzed by taking lineouts through the streak. Each lineout is fitted to a Gaussian and shifted such that all lineouts are centered at the same position. These shifted lineouts are summed and the result is fitted to a Gaussian to obtain σ_{MCP}.

Figure 6.1 shows the RMS bunch duration as a function of the RF compression field amplitude E_0. We are able to compress 0.25 pC bunches from 10 ps down to 100 fs durations. Also shown in this figure is the result of detailed particle tracking simulations with the GPT code [17], which take into account realistic external fields and all Coulombic interactions (as described in Sec. 3.4). Clearly the simulations agree very well with the measurements. We attribute remaining discrepancies to uncertainties in the charge, laser spotsize, and solenoid field strengths. The error in E_0 is mainly due to a systematic error in the detection of the absorbed RF power.

At the field strength of maximal compression there is hardly any difference between the streak and the slit projection, as shown in Fig. 6.5. We also show in Fig. 6.5 the streak intensity profiles of a maximally compressed bunch, the profile of the slit, and a Gaussian with $\sigma_{67} = \sqrt{(\sigma_{t,slit})^2 + (67\,\mathrm{fs})^2}$, where $\sigma_{t,slit}$ is the slit width converted to the time scale as if it were a streak. Because the σ_{67}-profile overlaps with the measured streak profile deconvolution of the streak yields a RMS bunch duration $t_b = 67$ fs. For comparison Fig. 6.5d also shows a Gaussian with $\sigma_{100} = \sqrt{(\sigma_{t,slit})^2 + (100\,\mathrm{fs})^2}$, clearly showing that RMS bunch durations well below 100 fs have been achieved.
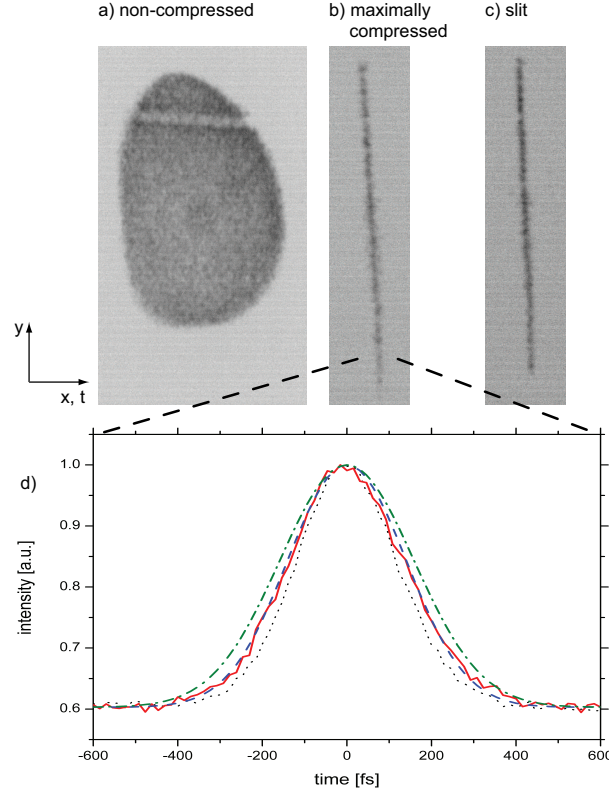
Figure 6.5: *(a) Streak of a non-compressed bunch, (b) streak of a maximally compressed bunch, (c) projection of the $10\,\mu m$ slit when the streak cavity is off. The pronounced horizontal line in panel (a) is due to a local narrowing in the slit. (d) Intensity profiles of a streak of a $67\,\mathrm{fs}$ bunch (red solid line), of the projection of the slit (black dotted line), of a Gaussian with $\sigma_{67} = \sqrt{(\sigma_{t,slit})^2 + (67\,fs)^2}$ (blue dashed line), and of a Gaussian with $\sigma_{100} = \sqrt{(\sigma_{t,slit})^2 + (100\,fs)^2}$ (green dash-dotted line).*

6.5 Compression field settings for optimum bunch compression

When measuring the bunch length at a fixed position z_{scr} in the beamline, obviously the shortest bunch length is measured if $z_{focus} = z_{scr}$. The focal length z_{focus} of the compression cavity depends on the RF field strength E_0 and the RF phase offset φ_0 in a not completely trivial way. In order to obtain the shortest bunch length it is essential to fully understand this dependency.

Figure 6.6 shows the RMS bunch duration t_b at the fixed position of the streak cavity, as simulated with GPT, where both E_0 and φ_0 are varied. All settings are the same as in the compression experiment described in the previous section. From Fig. 6.6 it is seen that for a fixed E_0 there are generally two minima for t_b as a function of φ_0: one at an accelerating phase ($\varphi_0 < 0$), and one at a decelerating phase ($\varphi_0 > 0$). Only below a certain optimal value $E_0 = E_{0,opt}$ there is a single minimum at $\varphi_0 \approx 0$.

This can be understood as follows. Consider an electron at the front and at the back of a bunch, separated a distance $2L$ apart, with velocities v_{front} and v_{back} respectively. If $v_{front} < v_{back}$ the electron at the back will overtake the front electron after having traveled a

83
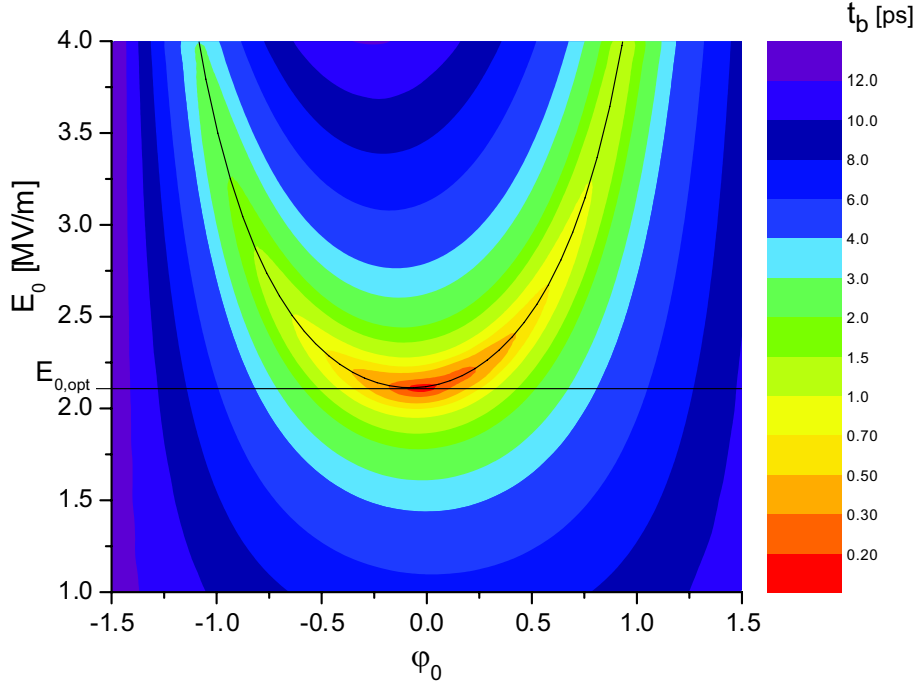
Figure 6.6: *RMS bunch duration in [ps] (at a fixed distance from the compression cavity) according to* GPT *simulations for various E_0 and φ_0. The bunch has a charge $Q = 0.25$ pC, and a kinetic energy $U_k = 95.0$ keV. The initial charge distribution is a Gaussian that is truncated at $1\,\sigma = 100\,\mu$m. The black curve is described by Eq. (6.4), where the parameters have the same values as in the experiment.*

distance $z_{focus} = 2Lv_{front}/(v_{back} - v_{front})$. Combining this with Eq. (3.6) for the momentum kick induced by the compression cavity, we find

$$z_{focus} \approx \frac{2\sqrt{2/m}U_k^{3/2}}{e\omega d_{cav}E_0\cos(\varphi_0)}, \tag{6.2}$$

with U_k the kinetic energy of the bunch, ω the angular frequency of the RF field, and d_{cav} the (effective) RF cavity length. Equation (6.2) shows the explicit dependence of the focal strength of the compression cavity on E_0 and φ_0. For one specific value of $E_0\cos(\varphi_0)$ the bunch is precisely focused at the screen. For other values the bunch is overfocused or underfocused, resulting in a measured bunch length that is larger than the waist. This is schematically shown in Figs. 6.7(a)-(c) for the three scenarios $E_0 = E_{0,opt}$, $E_0 < E_{0,opt}$, and $E_0 > E_{0,opt}$:

- For $E_0 = E_{0,opt}$ the bunch is shortest at the position of the screen z_{scr} when $\varphi_0 = 0$. If $\varphi_0 \neq 0$ the bunch is underfocused and has a longer duration at $z = z_{scr}$.

- For $E_0 < E_{0,opt}$ the bunch is inevitably underfocused: the bunch is shortest behind the screen. If $\varphi_0 \neq 0$ the position of the focus is even further away, and even longer bunch durations are measured at $z = z_{scr}$.

- For $E_0 > E_{0,opt}$ the bunch is generally overfocused. For two values of φ_0 (one at an accelerating phase $\varphi_0 < 0$, and one at a decelerating phase $\varphi_0 > 0$) the focal length is such that $z_{focus} = z_{scr}$. Therefore, if $E_0 > E_{0,opt}$, there are two minima for t_b as a function of φ_0.

The analysis is simplified by expanding Eq. (6.2) around $\varphi_0 = 0$ up to second order in φ_0 and rewriting it, yielding the approximation

$$E_0 \approx \frac{2\sqrt{2/m}U_k^{3/2}}{e\omega d_{cav}z_{focus}}\left(1 + \frac{1}{2}\varphi_0^2\right) \tag{6.3a}$$

$$= E_{0,opt}\left(1 + \frac{1}{2}\varphi_0^2\right), \tag{6.3b}$$

reflecting the parabola-like character of the lines of constant z_{focus} in Fig. 6.6. It follows that the experimental value $E_{0,opt} = 2.2\,\mathrm{MV/m}$, see Fig. 6.1, is obtained if $d_{cav} = 3.3\,\mathrm{mm}$. This effective length corresponds quite reasonably to the plateau of the on-axis field profile of the cavity as shown in Fig. 5.4.
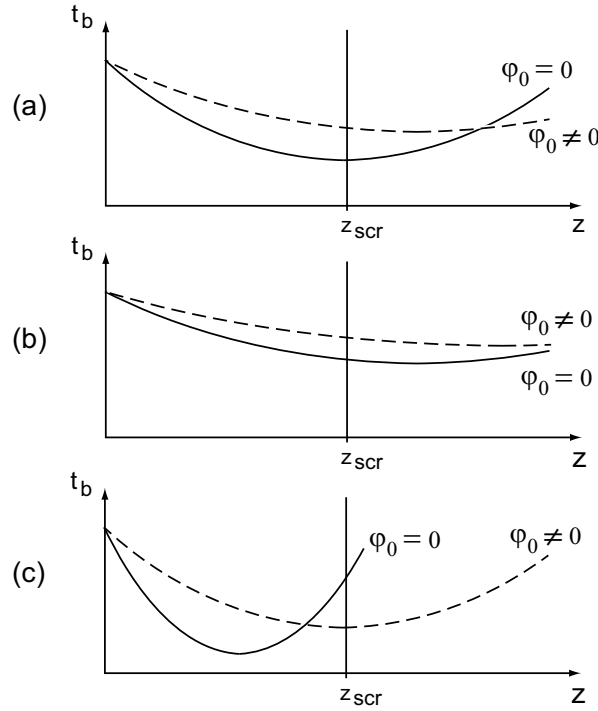
Figure 6.7: *Schematic curves of the bunch duration t_b as a function of position z for different values of the RF field amplitude E_0: (a) $E_0 = E_{0,opt}$, and $\varphi_0 = 0$ (solid line), $\varphi_0 \neq 0$ (dashed line); (b) $E_0 < E_{0,opt}$, and $\varphi_0 = 0$ (solid line), $\varphi_0 \neq 0$ (dashed line); (c) $E_0 > E_{0,opt}$, and $\varphi_0 = 0$ (solid line), $\varphi_0 < 0$ (dashed line), $\varphi_0 > 0$ (dotted line).*

From Fig. 6.6 it is seen that there is a slight asymmetry. This is a result of the fact that the compression cavity also slightly changes the kinetic energy of the bunch if $\varphi_0 \neq 0$,

according to Eq. (3.3). Inclusion of this effect yields the following equation for the focal length

$$z_{focus} \approx \frac{2\sqrt{2/m}U_k^{3/2}}{e\omega d_{cav}E_0\cos(\varphi_0)}\left[1 + \frac{ed_{cav}E_0}{U_k}\sin(\varphi_0)\right].$$ (6.4)

In Fig. 6.6 a curve described by this equation is shown, where z_{focus}, U_k, d_{cav}, and ω have the corresponding experimental values. The curve is in perfect agreement with the GPT simulations.

To illustrate the existence of two minima for t_b if $E_0 > E_{0,opt}$, the duration of a 0.5 pC bunch has been measured as a function of the RF phase offset, with $E_0 = 2.6$ MV/m fixed. Figure 6.8 shows the results of the measurements and of GPT simulations, which are in reasonable agreement. Clearly there are two minima, indicating that $E_0 > E_{0,opt}$. To obtain the shortest bunch E_0 has to be lowered.

To create the shortest bunch in practice, we use the following procedure. First the zero-crossing ($\varphi_0 = 0$) is roughly determined by using a bending magnet after the compression cavity: the deflection angle depends on the kinetic energy which is altered by the RF phase offset φ_0 of the compression cavity. The phase is adjusted such that the electrons hit the MCP at the same place as when the compression cavity was off. Then, starting at low RF field amplitude, the phase and the amplitude are further optimized by measuring the streak length.
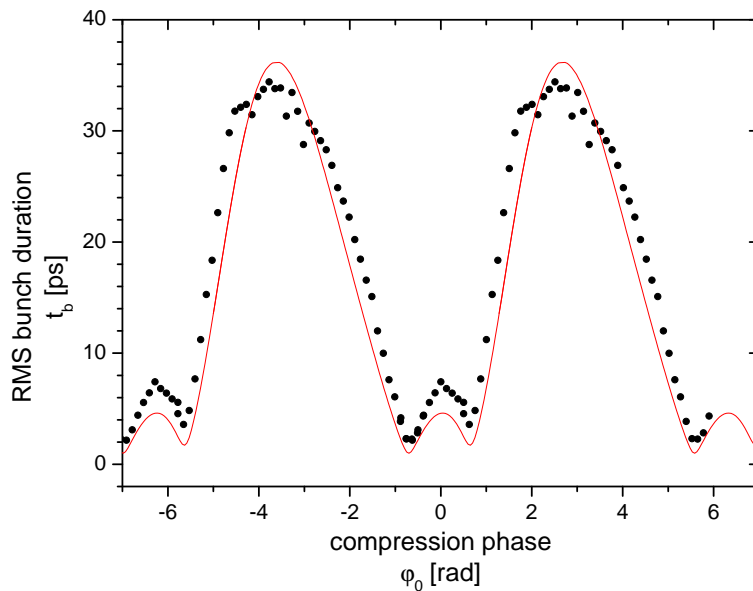
Figure 6.8: *RMS bunch duration as a function of the RF phase offset of the compression cavity. Data (dots) compare well to GPT simulations (solid line). The bunch has a charge $Q = 0.5$ pC, and a kinetic energy $U_k = 95.0$ keV. The initial charge distribution is a Gaussian that is truncated at $1\,\sigma = 100\,\mu$m. The RF compression field amplitude is fixed at 2.6 MV/m.*

6.6 Charge variations

Results of GPT simulations for compression of bunches of various charges are shown in Fig. 6.9. From this figure it is seen that (1) the RF field strength for maximum compression at a given position in the beamline is lower for bunches of higher charges, and (2) bunches of higher charges are longer at optimum compression. This can be explained as follows. Using the asymptotic expansion velocity $v_{\rm L}$, as introduced in Sec. 2.2.3, and the momentum difference $\Delta p_{z,bunch}$ induced by the compression cavity, see Eq. (3.6), it follows that the expansion is completely inverted if $E_0 = mv_c/(e\omega d_{cav} z_{cav})$, with z_{cav} the distance from the accelerator to the compression cavity. The RF field strength necessary for optimum compression is thus independent of the bunch charge density.[1] However, right after photoemission the expansion velocity is not constant; the expansion accelerates to reach the asymptotic expansion velocity. The acceleration depends on Q, as can be seen with Eq. (2.19). This effect can be taken into account by defining a virtual object distance, which is larger than the real object distance, leading to a smaller image distance. When lowering the focal strength (c.q. the RF field amplitude) of the compression cavity accordingly, the image point is repositioned to its original place in the beamline. This explains point (1). Because of the lower RF field strength the bunch will be a little less compressed at the fixed detection position, which explains point (2).

According to the simulations in Fig. 6.9 the measured bunch duration of 67 fs can be obtained if the bunch charge is 0.1 pC. In the experiments presented in Sec. 6.4 the nominal charge $Q = 0.24$ pC with $\sigma_{\rm Q} = 0.05$ pC due to laser power fluctuations (based on 500 consecutive shots). Given this $\sigma_{\rm Q}$ there is a finite probability that occasionally bunches of 0.1 pC are created, which are compressed to durations well below 100 fs.

Further, the GPT results show that for charges up to 1 pC bunches shorter than 200 fs can be created. Thus, relaxing the temporal resolution by only a factor of two allows a factor of 4 higher charge, which could be beneficial for UED on more complex structures like (bio-)molecules.

6.7 Arrival time jitter

For a pump-probe UED experiment the arrival time jitter of the electron bunch with respect to the pump (generally an ultrashort laser pulse) is crucial. In our setup phase jitter of the RF compression cavity leads to changes in the average velocity of the electron bunch, resulting in arrival time jitter at the position of the sample (or streak cavity), which can be determined from the measurements shown in Fig. 6.4. The thickness of the fitted curve reflects the confidence bounds, yielding an RMS jitter of 106 fs. This arrival time jitter can be translated back into 28 fs phase jitter of the RF field in the compression cavity, which agrees with the expectation based on the 20 fs synchronization accuracy between our 3 GHz oscillator and Ti:Sapphire oscillator [18]. The measurements shown in Fig. 6.4 have been performed at $E_0 = 2.9$ MV/m. As the arrival time jitter scales linearly with E_0, the RMS arrival time jitter is 80 fs at the field strength of maximum compression, i.e. $E_0 = 2.2$ MV/m.

---

[1]This is in analogy with optics, where the image distance depends only on the object distance and the focal strength of the lens.
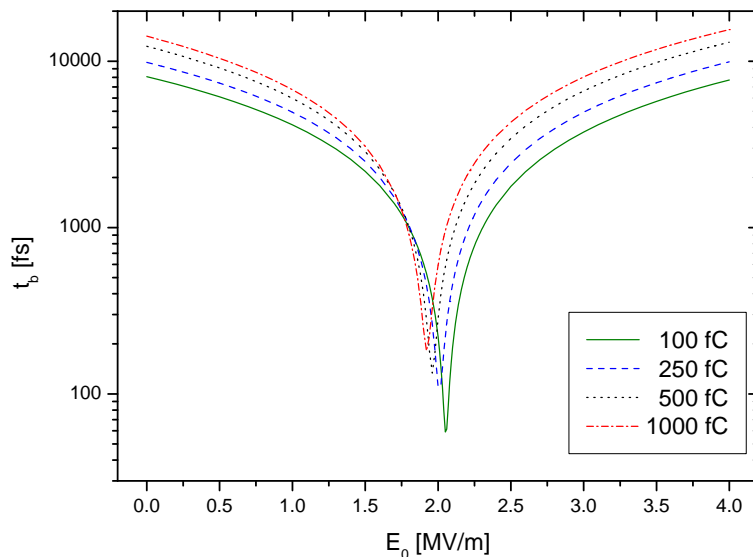
Figure 6.9: *RMS bunch duration as a function of compression field strength as simulated with* GPT *for various bunch charges. In the simulations the same settings are used as in the experiment described in Sec. 6.4.*

6.8 Single-shot electron diffraction

To show that our bunches have sufficient charge and are of sufficient quality for single-shot UED we carried out a diffraction experiment, that is described in more detail in Ch. 7.

We replaced the streak cavity by a standard calibration sample for transmission electron microscopy [19], consisting of a 300 μm copper mesh, a carbon interlayer and a polycrystalline gold layer of (9 ± 1) nm thickness. A third solenoid is positioned behind the sample with the MCP in its the focal plane. Figure 6.2 shows a diffraction pattern, recorded with a single 200 fC electron bunch. Figure 6.2 also shows the azimuthal integral of the Debye-Scherrer rings. The background due to the grid and the carbon layer has been subtracted from this curve, confirming that the rings are due to diffraction of electrons on the gold film. The curve is fitted according to kinematical diffraction theory, with the elastic scattering amplitude, the inelastic scattering amplitude, and the peak width as fit parameters. The relative positions of the Bragg peaks and their relative intensities are fixed at the theoretical values.

6.9 Conclusions

In conclusion we have demonstrated RF compression of sub-relativistic, space-charge-dominated electron bunches to sub-100 fs durations. Detailed charged particle simulations with the GPT code are consistent with our measurements. Our bunches are suitable for single-shot UED experiments, as we have shown by capturing a high-quality diffraction pattern from a polycrystalline gold film using a single electron bunch.

References

[1] T. van Oudheusden, P. L. E. M. Pasmans, S. B. van der Geer, M. J. de Loos, M. J. van der Wiel, and O. J. Luiten, arXiv **1006.2041v1 [physics.acc-ph]** (2010).

[2] J. R. Dwyer, C. T. Hebeisen, R. Ernstorfer, M. Harb, V. B. Deyirmenjian, R. E. Jordan, and R. J. D. Miller, Phil. Trans. R. Soc. A **364**, 741 (2006).

[3] R. Srinivasan, V. A. Lobastov, C.-Y. Ruan, and A. H. Zewail, Helv. Chim. Acta **86**, 1763 (2003).

[4] B. McNeil, Nature Photonics **3**, 375 (2009).

[5] D. A. Shapiro *et al.*, arXiv **0803.4027[physics:bio-ph]** (2010).

[6] B. J. Siwick, J. R. Dwyer, R. E. Jordan, and R. J. D. Miller, Science **302**, 1382 (2003).

[7] G. Sciaini *et al.*, Nature **456**, 56 (2009).

[8] N. Gedik, D.-S. Yang, G. Logvenov, I. Bozovic, and A. H. Zewail, Science **316**, 425 (2007).

[9] C.-Y. Ruan, V. A. Lobastov, F. Vigliotti, S. Chen, and A. H. Zewail, Science **304**, 80 (2004).

[10] P. Musumeci, J. T. Moody, C. M. Scoby, M. S. Gutierrez, H. A. Bender, and N. S. Wilcox, Rev. Sci. Instrum. **81**, 013306 (2010).

[11] T. van Oudheusden, E. F. de Jong, S. B. van der Geer, W. P. E. M. Op 't Root, B. J. Siwick, O. J. Luiten, J. Appl. Phys. **102**, 093501 (2007).

[12] O. J. Luiten, S. B. van der Geer, M. J. de Loos, F. B. Kiewiet, and M. J. van der Wiel, Phys. Rev. Let. **93**, 094802 (2004).

[13] O. D. Kellogg, *Foundations of Potential Theory*, Springer-Verlag, Berlin, 1929.

[14] P. Musumeci, J. T. Moody, R. J. England, J. B. Rosenzweig, and T. Tran, Phys. Rev. Lett. **100**, 244801 (2008).

[15] J. T. Moody, P. Musumeci, M. S. Gutierrez, J. B. Rosenzweig, and C. M. Scoby, Phys. Rev. ST Accel. Beams **12**, 070704 (2009).

[16] T. van Oudheusden, J. R. Nohlmans, W. S. C. Roelofs, W. P. E. M. Op 't Root, O. J. Luiten, 3 GHz RF streak camera for diagnosis of sub-100 fs, 100 keV electron bunches, in *Ultrafast Phenomena XVI*, edited by P. Corkum, S. De Silvestri, K. A. Nelson, E. Riedle, and R. W. Schoenlein, page 938, 2009.

[17] Pulsar Physics, `http://www.pulsar.nl/gpt`.

[18] F. B. Kiewiet, A. H. Kemper, O. J. Luiten, G. J. H. Brussaard, and M. J. van der Wiel, Nucl. Instrum. Methods A **484**, 619 (2002).

[19] Agar Scientific, Cross Grating S106, `http://www.agarscientific.com`.

7

Single-shot electron diffraction

In this chapter a diffraction experiment on a gold film is described, that is performed to demonstrate that the electron bunches created as described in this thesis are suitable for single-shot UED. To analyze the experimental results first a brief overview of well-known kinematical diffraction theory is given: we present in Sec. 7.1 some basic elastic scattering theory, and in Sec. 7.2 we treat conditions for constructive interference. The equation for the diffraction peak intensities is given, based on kinematical diffraction theory. Then, in Sec. 7.3 mechanisms that lead to inelastic scattering are briefly mentioned and the inelastic cross-section is given. Limitations of the kinematical theory, and the mean free path of electrons are described in Sec. 7.4. Finally, in Sec. 7.5, we connect the visibility of the diffraction pattern to the coherence length of an electron bunch, and we show the results of an electron diffraction experiment on a polycrystalline gold film.

Throughout this chapter theory is illustrated with examples for gold, where applicable.

7.1   Elastic scattering

When an electron passes along an atom it interacts with the atom's nucleus through the Coulomb force, leading to scattering of the electron. Generally two types of scattering are discerned: elastic scattering (this section), where the momentum of the electron is changed, while the energy change is insignificantly small[1]; inelastic scattering (see Sec. 7.3), where both the electron's energy and momentum are changed.

7.1.1   Scattering on a single atom

We start by describing one electron as a wave that scatters on a single atom positioned at $\vec{r_0}$. The incoming wave is usually assumed to be a plane wave as it comes from a distant source. The outgoing wave is described as a spherical wave originating from the atom on which the electron scatters. The total wave is a linear combination of the scattered and unscattered wave[2]

---

[1] If an electron scatters it radiates and loses some energy. However, this energy loss is very small and can be neglected in diffraction theory: the velocity and the wavelength of the electron are assumed to be unaltered after the scattering event.

[2] We left out the time-dependency $e^{-i\omega t}$ for convenience.

$$\psi(\vec{r}) = \psi_0 \left[e^{i\vec{k_0}\cdot\vec{r}} + f(\vec{\Delta k})\frac{e^{i\vec{k}\cdot(\vec{r}-\vec{r_0})}}{|\vec{r}-\vec{r_0}|} \right], \tag{7.1}$$

where $f(\vec{\Delta k})$ is the scattering amplitude, and $\vec{\Delta k} = \vec{k} - \vec{k_0}$, with $\vec{k_0}$ the wavevector of the incoming wave and $\vec{k}$ the wavevector of the outgoing wave. Note that for elastic scattering $|\vec{k_0}| = |\vec{k}| = k$ and only the angle $\theta = 2\arcsin\left(|\vec{\Delta k}|/(2\vec{k_0})\right)$ between the incoming and outgoing wave is relevant. To solve the Schrödinger equation for the total wave function, usually the (first) Born approximation is applied, which assumes that the total wave ψ does not differ too much from the incident wave ψ_0, and that the wave is scattered only once by the material (see e.g. Refs. [1, 2]). When also assuming that the scatterer is small compared to the distance to the detector, i.e. $|\vec{r}-\vec{r_0}| \approx |\vec{r}|$, the wave function is given by

$$\psi(\vec{r}) = \psi_0 \left[e^{i\vec{k_0}\cdot\vec{r}} + f(\theta)\frac{e^{i\vec{k}\cdot\vec{r}}}{|\vec{r}|} \right], \tag{7.2}$$

with the scattering amplitude

$$f(\theta) \approx -\frac{m}{2\pi\hbar^2} \int e^{i\vec{\Delta k}\cdot\vec{r_0}} V_{at}(\vec{r_0}) d^3\vec{r_0}, \tag{7.3}$$

where m is the electron mass, $\hbar$ is the reduced Planck constant, and $V_{at}(\vec{r})$ is the scattering potential of the atom. Equation (7.3) shows that the scattered wave is proportional to the Fourier transform of the scattering potential. It is this principle that is used in diffraction experiments. In case of a periodic potential (i.e. periodically arranged atoms) constructive interference can occur as described in Sec. 7.2.

When scattering on N_{at} atoms at positions $\vec{R}_j$ the scattering potential has to be replaced by $V(\vec{r}) = \sum_{j=0}^{N_{at}} V_{at,\vec{R}_j}(\vec{r} - \vec{R}_j)$, where $V_{at,\vec{R}_j}$ is the scattering amplitude of the specific atom at position $\vec{R}_j$. The total scattering amplitude is then simply the sum of all atomic scattering amplitudes $f_{at,\vec{R}_j}$. The quantity measured is the probability for scattering over an angle θ, which is given by

$$P_{scatt}(\theta) = \psi^*\psi \propto \left| \sum_{j=1}^{N_{at}} f_{at,\vec{R}_j}(\theta) e^{-i\vec{\Delta k}\cdot\vec{R}_j} \right|^2. \tag{7.4}$$

7.1.2 Scattering amplitude and cross-section

For V_{at} in Eq. (7.3) usually a screened Coulomb potential is used, according to $V_{at}(r) = -\frac{Ze^2}{4\pi\varepsilon_0 r}e^{-r/r_{at}}$, with e the elementary charge, Z the atomic number, and ε_0 the permittivity of vacuum. Using the effective radius of the atom $r_{at} = a_H Z^{-1/3}$, with a_H the Bohr radius, as follows from the Thomas-Fermi model of an atom, the scattering amplitude yields

$$f(\theta) = \frac{2Za_H}{(\Delta k)^2 a_H^2 + Z^{2/3}}. \tag{7.5}$$

To characterize the angular distribution of scattered particles commonly the differential cross-section $\frac{d\sigma}{d\Omega}$ is used: an incoming electron that passes through the area element $d\sigma$ is scattered into a cone of solid angle $d\Omega$. The scattering amplitude $f(\theta)$ is related to the differential cross-section for elastic scattering by [2]

$$\frac{d\sigma_{el}}{d\Omega} = |f(\theta)|^2. \tag{7.6}$$

In case of an unscreened Coulomb potential the well-known Rutherford cross-section is obtained

$$\frac{d\sigma_{\mathrm{R}}}{d\Omega} = \left[\frac{Ze^2}{16\pi\varepsilon_0 U_k \sin^2(\theta/2)} \right]^2, \tag{7.7}$$

where $U_k = \hbar^2 k_0^2/(2m)$ is the kinetic energy of the incident electrons. From Eq. (7.5) or (7.7) it can be seen that the scattering amplitude decreases for larger scattering angles. Figure 7.1 shows the differential elastic scattering cross-section from the NIST database [3] and the Rutherford cross-section, which clearly is only valid for relatively large scattering angles. At small angles the scattering cross-section is approximately constant, and therefore the precise dependence of f_{at} on θ can generally be ignored when considering diffraction from a crystal.
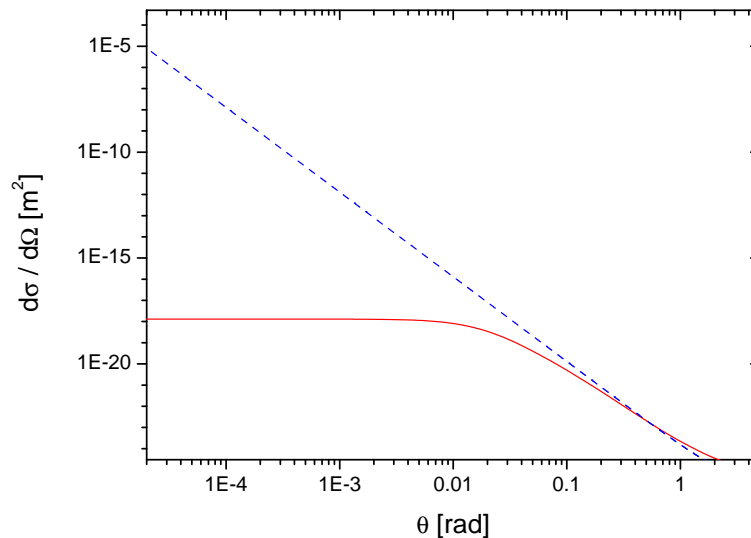
Figure 7.1: *Differential scattering cross-section for elastic scattering of $100\,\mathrm{keV}$ electrons on gold, according to NIST [3] (red solid line), and the Rutherford cross-section (blue dashed line).*

7.1.3 Scattering on a crystal

Because of the periodicity in a crystal, a unit cell can be defined that consists of a single atom, a single molecule, multiple atoms, or multiple molecules. The origins of the unit cells are given by $\vec{r_g} = m\vec{a_1} + n\vec{a_2} + p\vec{a_3}$, where $\{m, n, p\} \in \mathbb{Z}$, and $\vec{a_1}$, $\vec{a_2}$, and $\vec{a_3}$ are the primitive vectors that span the crystal. In a mono-atomic crystal the positions $\vec{R_j}$ of the atoms, as

introduced in Sec. 7.1.1, are precisely $\{\vec{r_g}\}$. Combining this with Eq. (7.4) it follows that the scattering intensity is maximum when

$$\vec{\Delta k} \cdot (m\vec{a_1} + n\vec{a_2} + p\vec{a_3}) = q2\pi, \tag{7.8}$$

with $q \in \mathbb{Z}$.

If the unit cell contains more than one atom the position of the k-th atom in the unit cell is given by $\vec{r_k} = u_k\vec{a_1} + v_k\vec{a_2} + w_k\vec{a_3}$, and the position of the atom in the lattice is given by $\vec{R_j} = \vec{r_g} + \vec{r_k}$. The scattered part of the wave function yields

$$
\begin{aligned}
\psi_{scatt}(\vec{\Delta k}) \quad &\propto \quad \sum_{\vec{r_g}} \sum_{\vec{r_k}} f_{at}(\vec{r_g} + \vec{r_k})e^{-i\vec{\Delta k}\cdot(\vec{r_g}+\vec{r_k})} \\
&= \quad \sum_{\vec{r_k}} f_{at}(\vec{r_k})e^{-i\vec{\Delta k}\cdot\vec{r_k}} \sum_{\vec{r_g}} e^{-i\vec{\Delta k}\cdot\vec{r_g}} \\
&= \quad \mathcal{F}(\vec{\Delta k}) \sum_{\vec{r_g}} e^{-i\vec{\Delta k}\cdot\vec{r_g}} \\
&= \quad \mathcal{F}(\vec{\Delta k})\mathcal{S}(\vec{\Delta k}), \tag{7.9}
\end{aligned}
$$

where in the second line the periodicity of the crystal is used: $f_{at}(\vec{R_j} + \vec{r_g}) = f_{at}(\vec{R_j})$. The so-called shape factor (or form factor, or lattice amplitude), which depends only on the lattice type of the crystal, is defined as

$$\mathcal{S}(\vec{\Delta k}) \equiv \sum_{\vec{r_g}}^{lattice} e^{-i\vec{\Delta k}\cdot\vec{r_g}}. \tag{7.10}$$

The so-called structure factor, which depends only on the positions and types of atoms inside a unit cell, is defined as

$$\mathcal{F}(\vec{\Delta k}) \equiv \sum_{\vec{r_k}}^{basis} f_{at}(\vec{r_k})e^{-i\vec{\Delta k}\cdot\vec{r_k}}. \tag{7.11}$$

The decomposition of the scattered wave into a shape factor and a structure factor reflects the decomposition of a crystal into a lattice and a basis. When making a molecular movie (see Sec. 1.1) typically diffraction from a crystal of molecules is measured and the change in time of the structure factor is studied to examine the dynamical behavior of the molecule.

7.2 Diffraction

7.2.1 Laue condition and Bragg condition

The condition for constructive interference can be described in the reciprocal space, yielding the Laue condition, or in the real space, yielding the Bragg condition. Both conditions are thus principally the same, as explained in this section.

The reciprocal lattice vectors $\vec{g}$ are defined by $e^{i\vec{g}\cdot\vec{r}_g} = 1$ and written as $\vec{g} = h\vec{a_1^*} + k\vec{a_2^*} + l\vec{a_3^*}$, where $\{h, k, l\} \in \mathbb{Z}$, and $\{\vec{a_1^*}, \vec{a_2^*}, \text{and } \vec{a_3^*}\}$ are the primitive vectors that span the reciprocal lattice. It can be shown that the reciprocal lattice vectors are normal to the lattice planes which are spaced a distance $d_{hkl} = 2\pi/|\vec{g}|$ apart (see e.g. Ref. [4]). Comparing the shape factor, as defined by Eq. (7.10), with the definition of the reciprocal lattice yields the Laue condition for constructive interference

$$\Delta\vec{k} = \vec{g}. \tag{7.12}$$

This condition is visualized in Fig. 7.2 by the geometrical Ewald sphere construction: the tip of the incoming wave vector $\vec{k_0}$ is placed at a point of the reciprocal lattice. The center of the Ewald sphere is at the tail of $\vec{k_0}$ and the radius of the Ewald sphere equals $|\vec{k_0}| = 2\pi/\lambda$. Because for elastic scattering $|\vec{k_0}| = |\vec{k}| = k$ the tips of all possible scattered vectors $\vec{k}$ also lie on the Ewald sphere. In geometrical terms the Laue condition states that constructive interference occurs when the Ewald sphere intersects a point of the reciprocal lattice. Because the wave vectors of the incoming and scattered wave have the same length, this condition is only fulfilled for certain scattering angles $2\theta_{\mathrm{B}}$.

This can also be considered in real space. Figure 7.3(a) shows a plane wave incident on a surface at angle θ_i and scattered into an angle θ_s. The path difference between the two rays scattered at points O and P is $\Delta_{\mathrm{OP}} = OP[\cos(\theta_i) - \cos(\theta_s)]$. Because the separation between O and P is continuous, there will be as much destructive as constructive interference and no diffraction pattern will build up unless $\theta_i = \theta_s = \theta_{\mathrm{B}}$. Figure 7.3(b) shows a plane wave incident on a crystal lattice. Part of the plane wave is scattered by the upper plane of the crystal, while another part is scattered by the lower plane. From the figure it can be derived geometrically that the path difference between these two scattered parts is $\Delta l = 2d\sin(\theta_{\mathrm{B}})$. The scattered parts will interfere constructively if they are in phase, which is the case when the so-called Bragg condition is fulfilled

$$2d\sin(\theta_{\mathrm{B}}) = q\lambda, \tag{7.13}$$

with θ_{B} the Bragg angle, λ the De Broglie wavelength of the electrons, d the lattice plane spacing, and $q \in \mathbb{Z}$. Using $|\vec{g}| = 2\pi/d$ and $|\Delta\vec{k}| = 2k\sin(\theta_{\mathrm{B}}) = 4\pi/\lambda\sin(\theta_{\mathrm{B}})$ it is straightforward to see that the Bragg condition and the Laue condition are equivalent.
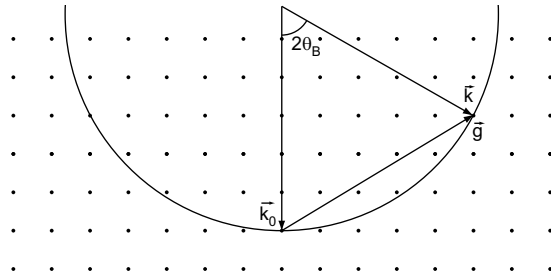
Figure 7.2: *Ewald sphere construction in the reciprocal space that shows for which reciprocal lattice points the Laue condition is fulfilled.*
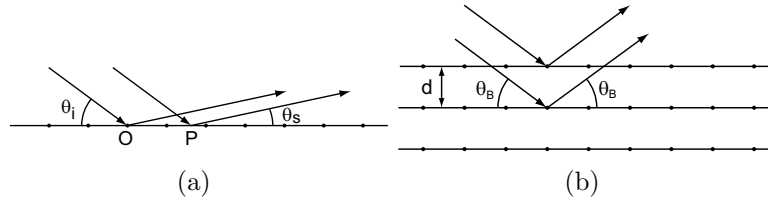
Figure 7.3: *(a) Scattering of a plane wave with $\theta_i \neq \theta_s$. (b) Bragg angle θ_B for a plane wave scattering from different crystal planes.*

7.2.2   Structure factor

If the Laue condition is fulfilled, the structure factor can be calculated analytically for the different types of unit cells, see e.g. Refs. [1, 5]. For some types the structure factor equals zero for certain combinations of h, k, and l. For example, gold has a Face-Centered Cubic (FCC) structure as illustrated in Fig. 7.4. The following four vectors give the positions of the atoms in the unit cell:

$$\{\vec{r_k}\} = \begin{aligned} &\{0\vec{a_1} + 0\vec{a_2} + 0\vec{a_3}, \\ &0\vec{a_1} + \tfrac{1}{2}\vec{a_2} + \tfrac{1}{2}\vec{a_3}, \\ &\tfrac{1}{2}\vec{a_1} + 0\vec{a_2} + \tfrac{1}{2}\vec{a_3}, \\ &\tfrac{1}{2}\vec{a_1} + \tfrac{1}{2}\vec{a_2} + 0\vec{a_3}\}. \end{aligned}$$

Inserting these $\{\vec{r_k}\}$ into the structure factor leads to

$$\mathcal{F}_{\text{FCC}} = \begin{cases} 4f_{at} & \text{if } h,\, k,\, l \text{ are either all even or all odd;} \\ 0 & \text{otherwise.} \end{cases}$$

Therefore the first few observable diffraction peaks are, at increasing Bragg angle, the (111), (200), (220), (311), and (222) peak.
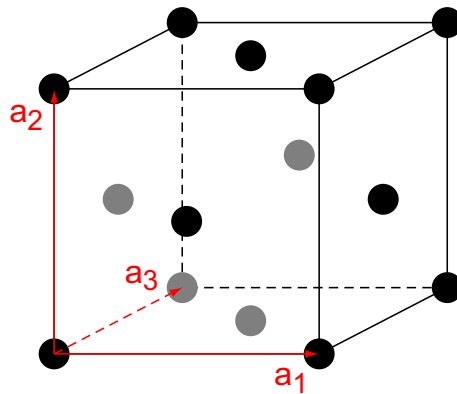
Figure 7.4: *FCC unit cell.*

7.2.3 Lineshape: intensity and width

Assuming an ideal crystal and an ideal electron bunch, the width of a diffraction peak is determined by the shape factor. If the crystal is, for example, a rectangular prism with N_x, N_y, and N_z unit cells along the $\vec{e_x}$-, $\vec{e_y}$-, and $\vec{e_z}$-directions the intensity associated with the shape factor yields

$$\mathcal{S}^*\mathcal{S} = \frac{\sin^2(\pi\Delta k_x a_x N_x)}{\sin^2(\pi\Delta k_x a_x)}\frac{\sin^2(\pi\Delta k_y a_y N_y)}{\sin^2(\pi\Delta k_y a_y)}\frac{\sin^2(\pi\Delta k_z a_z N_z)}{\sin^2(\pi\Delta k_z a_z)}. \tag{7.14}$$

This equation is well-known in optics as the intensity of the diffraction pattern of a grating with N_i slits and spacing a_i (where $i = x, y, z$). From this equation it follows immediately that a diffraction peak has a full-width-at-half-maximum $\Delta k_{i,\mathrm{FWHM}} = 0.886/(a_i N_i)$. For a 10 nm thin sample the peak width is thus approximately $0.1\,\mathrm{nm}^{-1}$, while the peak position $\Delta k_i \sim 1\,\mathrm{nm}^{-1}$.

The intensity I_{hkl} of a diffraction peak corresponding to the hkl family of planes is given by [5]

$$I_{hkl} \propto p_{hkl}e^{-2M_g}d_{hkl}. \tag{7.15}$$

The factor p_{hkl} is the multiplicity of the (hkl) plane, arising from the symmetry of a crystal. The factor e^{-M_g} (which is squared in Eq. (7.15)) is the so-called 'Debye-Waller' factor [5]. This temperature dependent factor takes into account thermal vibrations of atoms around their center positions and is typically used to study phase transitions of condensed matter in UED experiments.

7.3 Inelastic scattering

During an inelastic scattering event both the momentum and the energy of the incident electron are changed. Mechanisms that may lead to the energy transfer are, in order of increasing energy,

- phonon excitations, and excitations of oscillations of molecules (20 meV to 1 eV);

- inter- and intra-band excitations of outer atomic electrons (3 to 25 eV);

- excitations of plasmons (3 to 25 eV);

- ionization of core electrons in inner atomic shells (10 eV to 1 keV; the energy change is proportional to the atomic number).

The latter is the dominant contribution to inelastic scattering and the corresponding differential cross-section is, in the small angle approximation, given by [5]

$$\frac{d\sigma_{inel}}{d\Omega} = Z\frac{\lambda^4\left(1 + U_k/U_0\right)^2}{4\pi^4 a_{\mathrm{H}}^2}\frac{1 - \left[1 + \left(\theta^2 + \theta_{\mathrm{E}}^2\right)/\theta_0^2\right]^{-2}}{\left(\theta^2 + \theta_{\mathrm{E}}^2\right)^2}, \tag{7.16}$$

with U_0 and U_k the rest energy and the kinetic of an electron respectively, $\theta_\mathrm{E} \approx \Delta U/(2U_k) \approx 13.5[eV]Z/(4U_k)$ [6] the characteristic angle for inelastic scattering, $\theta_0 = \lambda Z^{1/3}/(2\pi a_\mathrm{H})$ the characteristic angle for elastic scattering, a_H the Bohr radius, and Z the atomic number. Using Eq. (7.16) it is calculated that the ratio of the total inelastic to the total elastic cross-section is approximately $26/Z$, while experimentally a ratio of $20/Z$ is found [5]. For gold ($Z = 79$) a ratio between 0.25 and 0.33 is thus expected. On the basis of the equations in this paragraph the typical angles for gold are $\theta_\mathrm{E} = 11\,\mathrm{mrad}$ and $\theta_0 = 48\,\mathrm{mrad}$ in case of $90\,\mathrm{keV}$ electrons incident on a gold crystal.

7.4   Limitations of kinematical theory

In kinematical theory it is assumed that an electron scatters maximally once while passing through a sample. This is a good approximation if the sample thickness is less then or comparable to the mean free path $\mathcal{L}_{mf}$ given by

$$\mathcal{L}_{mf} = \left(n\sigma_{tot}\right)^{-1}, \tag{7.17}$$

with n the number density, and σ_{tot} the total scattering cross-section (both elastic and inelastic scattering). For gold this yields $\mathcal{L}_{mf} = 6.4\,\mathrm{nm}$.

Further, kinematical theory assumes no interaction between incident and scattered waves, and no absorption. Dynamical theory (not described in this thesis) incorporates these effects, see e.g. Ref. [5].

7.5   Single-shot electron diffraction on a polycrystalline gold film

7.5.1   Fulfilling the Bragg condition

In practice there are two approaches to fulfill the Bragg condition. The 'Laue method' uses a distribution of wavelengths of the incident electrons to probe a single crystal sample. For some of the wavelengths the Bragg condition is satisfied for some crystal planes, yielding a diffraction pattern of 'Laue spots'. In the 'Debye-Scherrer method' electrons of the same wavelength are used to probe a polycrystalline sample. Because there is an angular distribution of crystallites some are oriented such that the Bragg condition is fulfilled. Sufficient crystallites have to be irradiated to obtain a high-quality diffraction pattern, consisting of 'Debye-Scherrer rings'. Using monochromatic electrons for diffraction on a single crystal sample, would require the diffractometer to provide three degrees of freedom for complete structural characterization. Using polychromatic electrons on a polycrystalline sample, would generally produce a blurred diffraction pattern of poor visibility.

In this section a diffraction experiment is described, where a polycrystalline gold film is probed in transmission with an electron bunch that has a relatively small energy spread (or a small bandwidth when considering their wavelength).

7.5.2 Coherence of the incident electron bunch

Angular spread of the electron ensemble that scatters on the sample will lead to blurring of the diffraction pattern. In case of severe blurring neighboring diffraction peaks cannot be discerned, or, in other words, the visibility is too low. Visibility is defined as $\mathcal{V} \equiv (I_{max} - I_{min})/(I_{max} + I_{min})$, where I_{max} and I_{min} are the intensities of a maximum and the adjacent minimum. According to Ref. [7] coherence means $\mathcal{V} \geq 0.88$, which is obtained, in the case of an array of uniform circular scatterers, when the lattice spacing $a_0 \leq \lambda/(\pi\Delta\theta)$. Combining this with the coherence length of an electron bunch, as defined by Eq. (3.1), and using $\Delta\theta = 2\sigma_\theta$ in case of uniform angular spread, it follows that an electron bunch with $L_\perp \geq a_0$ yields a diffraction pattern of proper visibility. For example gold has a lattice constant $a_0 = 0.408$ nm, and small molecules have lattice constants of several nm. As we are aiming for coherence lengths of typically several nm we expect to obtain a clear diffraction pattern of a gold sample. A diffraction experiment on a small molecule would also be possible according to this calculation.

If the sample is not in a beam waist, the incident electrons also have a correlated angular spread. In case of diffraction on a polycrystalline sample this does not make a difference, as long as the crystallites are sufficiently small. However, for a crystalline sample the orientation of the crystal with respect to the incoming electrons is of utmost importance. In case of a large angular spread, many electrons will not contribute to the diffraction pattern, leading to a lower visibility.

Also energy spread, i.e. a spread in wavelength, of the incident electrons can lead to blurring of the diffraction pattern. The longitudinal coherence $L_\parallel$ can be defined as the distance that waves, with wavelengths between $\lambda - 1/2\Delta\lambda$ and $\lambda + 1/2\Delta\lambda$, have to travel to acquire a phase difference of π, leading to

$$L_\parallel \approx \frac{\lambda^2}{\Delta\lambda} = hc\frac{\sqrt{U_k(U_k + 2U_0)}}{U_k + U_0}\frac{1}{\Delta U_k}. \tag{7.18}$$

When again requiring $a_0 \leq \lambda/(\pi\Delta\theta)$ and using $\Delta\theta_B = \theta_B\Delta\lambda/\lambda$ it follows that an electron bunch with $L_\parallel \geq a_0\pi\theta_B$ yields a diffraction pattern of good visibility. For a 100 keV electron bunch with $\sigma_{U_k} = 1$ keV and typical Bragg angles of $1 - 10$ mrad it follows that a_0 can be as large as $20 - 200$ nm. In the experiments described in this thesis it is therefore the transverse coherence that determines the quality of a diffraction pattern.

7.5.3 Experimental setup

To show that the electron bunches created as described in Ch. 6 are of sufficient quality to capture a diffraction pattern with a single bunch, we have carried out a diffraction experiment on a polycrystalline gold film. The setup is the same as depicted in Fig. 6.3, but the streak cavity is replaced by a sample chamber. Downstream of the sample chamber a third solenoid is placed, which is specified in Table 4.1. The focal strength of this solenoid is such that the MCP is in the focal plane.[3] The sample is a standard TEM calibration sample [8], as specified in Table 7.1.

---

[3]The diffraction pattern can be measured either far away from the sample, or, more conveniently, in the focal plane of a charged-particle lens.

Table 7.1: *Specifications of the S106 cross grating gold sample [8].*

mesh	copper	2160 lines/mm
mesh thickness	copper	12 μm
interlayer	carbon	not specified, typically 10 nm
film	gold	(9 ± 1) nm
diameter		3 mm
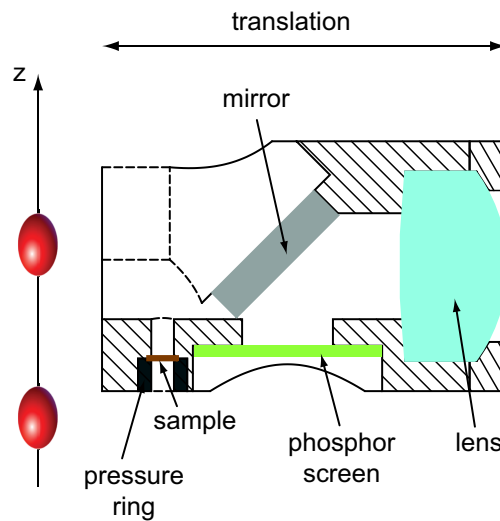
Figure 7.5: *Sample holder with phosphor screen (in the same plane as the sample), mirror and lens. The entire mount can be translated in the direction perpendicular to the electron beam path.*

The sample is placed in a holder and clamped with a pressure ring. Next to the sample a P20 phosphor screen is placed at the focal plane of an achromatic doublet lens, as illustrated in Fig. 7.5. A mirror behind the screen directs the collected light to a vacuum window. Outside the vacuum another achromatic doublet is used to image the screen onto a CCD camera. This part of the holder is described in detail in Ref. [9]. To move the sample holder (and the P20 screen) in and out of the beamline it is connected to the end of a linear translation feedthrough.

The UV photoemission laser is shaped with a 200 μm pinhole as described in Sec. 4.1.3, yielding a RMS spotsize $\sigma_c = 54 \, \mu$m at the cathode, and a thermal emittance $\varepsilon_{n,th} = 40$ nm.

The electron bunch is first centered at the phosphor screen. The field strength of the first solenoid is adjusted such that the waist is approximately at the screen. (The second solenoid is not used.) Then the sample is moved to the position of the beam waist and the field strength of the third solenoid is adjusted to obtain the sharpest possible diffraction pattern on the MCP. The bunch parameters at the sample and the solenoid settings are summarized in Table 7.2. Finally, a beam stop is inserted just in front of the MCP to block the zeroth order diffraction peak.

Table 7.2: *Bunch parameters at the sample.*

|	
RMS spotsize σ_x	$(440 \pm 20)\,\mu\text{m}$
RMS spotsize σ_y	$(300 \pm 20)\,\mu\text{m}$
transverse coherence length $L_\perp$	$(4 \pm 1)\,\text{nm}$
charge Q	$0.2\,\text{pC}$
kinetic energy U_k	$90.0\,\text{keV}$

7.5.4 Experimental results

In Fig. 7.6 we show an example of a single-shot diffraction pattern of the gold film that has been captured as described in the previous section. This image is a truly single-shot-recording as follows from the timings of the different elements involved: the repetition frequency of the photoemission laser $f_{rep} = 5\,\text{Hz}$, the integration time of the camera $T_{int} = 1\,\text{ms}$, and the decay time (to 10% of the intensity) of the phosphor screen behind the MCP is $0.2\,\text{ms}$.

The bottom panel of Fig. 7.6 shows the azimuthal integral of the Debye-Scherrer rings. The backgrounds due to the mesh and the carbon layer have been subtracted from this curve, confirming that the rings are due to diffraction of electrons on the gold film. The curve is fitted according to kinematical diffraction theory as described by Eqs. (7.15) and (7.16). The relative peak positions are fixed to their theoretical values and the relative peak heights are fixed to literature values [3]. The fitting parameters are the elastic and inelastic scattering intensities, the characteristic angle θ_{E} for inelastic scattering, and the widths of the peaks (we assumed Gaussian broadening of the diffraction peaks). The first four peaks, corresponding to the (111), (200), (220), and (311) lattice planes, are clearly visible. The relative peak positions are consistent with the theoretical values. The relative intensities are in good agreement with literature values.

To do a diffraction measurement on a sample placed at the same position as the point of optimum bunch compression (see Ch. 6) the streak camera had to be removed from the setup. The duration of the actual bunches that are used in the diffraction experiment is thus undetermined. However, the settings for optimum bunch compression are known from the experiments presented in Ch. 6. With the RF field strength of the compression cavity at the value for optimum compression, and varying the RF phase offset the diffraction pattern remained intact. It is therefore concluded that the compressed bunches, as presented in Ch. 6, are of sufficient quality for single-shot UED experiments.

For future experiments one option is to use laser ponderomotive scattering [10] to measure the bunch length, which can be done inside the sample chamber.
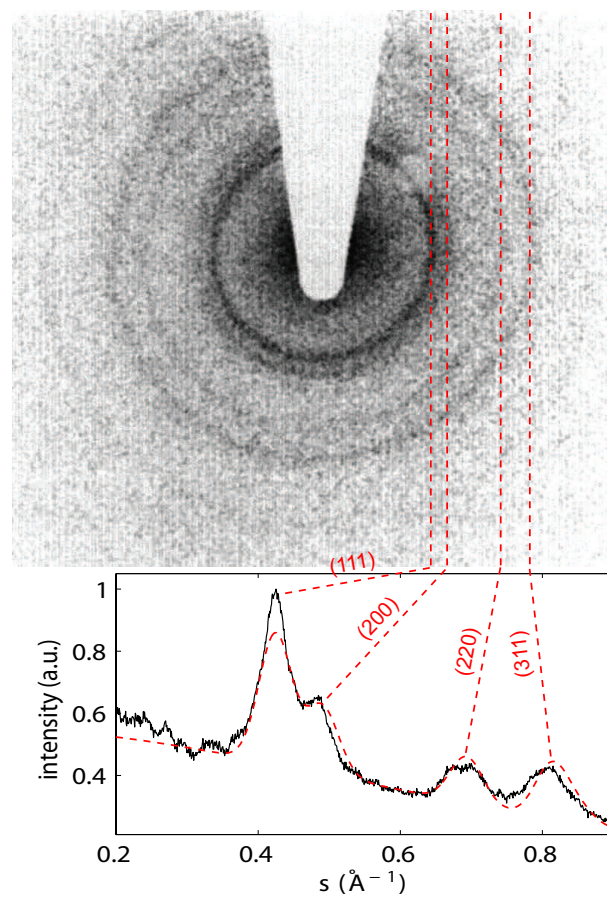
Figure 7.6: *Single-shot diffraction pattern. (top) Debye-Scherrer rings. (bottom) Azimuthal integral of the Debye-Scherrer rings (solid line) and a fit according to kinematical diffraction theory (dashed line).*

References

[1] B. Fultz, and J. M. Howe, *Transmission Electron Microscopy and Diffractometry of Materials*, Springer, 2002.

[2] D. J. Griffiths, *Introduction to Quantum Mechanics*, Pearson Education, 2005.

[3] NIST Standard Reference Database 64, NIST electron elastic scattering cross-section database, June 2003, version 3.1.

[4] N. W. Ashcroft, and N. D. Mermin, *Solid State Physics*, W. B. Saunders Company, 1976.

[5] L. Reimer, and H. Kohl, *Transmission Electron Microscopy, Physics of Image Formation*, Springer, 2008.

[6] H. Koppe, Z. Phys. A **124**, 658 (1948).

[7] E. Hecht, *Optics*, Pearson Education, 2002.

[8] Agar Scientific, Cross Grating S106, `http://www.agarscientific.com`.

[9] F. B. Kiewiet, *Generation of ultrashort, high-brightness relativistic electron bunches*, PhD thesis, Technische Universiteit Eindhoven, 2003.

[10] C. T. Hebeisen, G. Sciaini, M. Harb, R. Ernstorfer, T. Dartigalongue, S. G. Kruglik, and R. J. D. Miller, Opt. Express **16**, 3334 (2008).

8

Transverse phase-space measurements of (waterbag) bunches

In this chapter we show preliminary measurements of the transverse beam quality, i.e., the transverse phase-space and the emittance, of bunches produced with the 100 kV DC photogun that is described in Ch. 4. Before presenting the results we theoretically treat the phase-space distribution of a waterbag bunch.

As pointed out in Sec. 2.2 the linear space-charge fields inside a waterbag bunch lead to a linear 6D phase-space distribution $f(\vec{r}, \vec{p})$, given by

$$f(\vec{r}, \vec{p}) = \rho_0 \Theta \left(1 - \left(\frac{x}{A} \right)^2 - \left(\frac{y}{B} \right)^2 - \left(\frac{z}{C} \right)^2 \right) \delta \left(\vec{p} - \mathbf{D}\vec{r} \right), \tag{8.1}$$

where ρ_0 is the charge density, $\vec{r}$ the particle position, $\vec{p}$ the particle momentum, $\Theta(x)$ the Heaviside step function, and $\delta(\vec{x})$ the 3D Dirac delta function. For a purely space-charge-driven expansion the 3×3 matrix $\mathbf{D}$ is diagonal. Linear charged particle optics transform the 6D phase-space in a linear way: the ellipsoid can be rotated and deformed, and non-diagonal elements can be added to the matrix $\mathbf{D}$, but $f(\vec{r}, \vec{p})$ retains its linear character [1]. This makes a uniformly charged ellipsoid the ideal bunch.

The 6D phase-space distribution cannot be measured directly. However, it is fully determined by the three projections onto the three 2D phases-spaces (x, p_x), (y, p_y), and (z, p_z), if for all particles the three degrees of freedom are decoupled. For a waterbag bunch the distribution $f_x(x, p_x)$ of the projection of $f(\vec{r}, \vec{p})$ onto the (x, p_x)-space is given by

$$f_x(x, p_x) \equiv \int dy \int dp_y \int dz \int dp_z f(\vec{r}, \vec{p}) \tag{8.2a}$$

$$= \rho_0 \frac{\pi BC}{A^2} \left(A^2 - x^2 \right) \delta(p_x - D_{11}x). \tag{8.2b}$$

The (y, p_y) and (z, p_z) phase-space distributions can be obtained analogously. These 2D phase-phase distributions are therefore straight lines with parabolic density profiles.

The density distribution can also be obtained from the projection of the bunch onto the (x, y)-space. This is simply the transverse beam profile, which can be easily measured. For a waterbag bunch the density distribution of this projection is given by $\sigma(x, y) =$

$2\rho_0 C \sqrt{1 - (x/A)^2 - (y/B)^2}$. Integration of this 2D density profile yields a parabolic line density profile. Projections onto the (y, z)-space and the (x, z)-space have analogous density distributions, which can be measured with e.g. a streak camera.

So far we have treated zero-temperature waterbag bunches. In reality however, the photoemitted electron bunch starts off with a nonzero uncorrelated energy spread and angular spread (see also Sec. 2.1.3). This is taken into account by a convolution of a thermal momentum distribution with the ideal $T_e = 0$ phase-space distribution (as given by Eq. (8.2b)), yielding

$$f_x(x, p_x) = \rho_0 \frac{\pi BC}{A^2} \left(A^2 - x^2\right) \frac{e^{-(p_x - D_{11}x)^2 / 2mk_{\mathrm{B}}T_e}}{\sqrt{2\pi mk_{\mathrm{B}}T_e}}, \tag{8.3}$$

where k_{B} is Boltzmann's constant, and T_e is the effective temperature. As an illustration we show in Fig. 8.1 schematically the (x, p_x) phase-space distribution of a $T_e = 0$ waterbag bunch and of a $T_e \neq 0$ waterbag bunch, both at $t = 0$ (i.e. at the time of photoemission) and at $t > 0$.

To establish experimentally the realization of a waterbag bunch, the distribution of the three different 2D phase-space projections should be measured. In Sec. 8.1 we show preliminary measurements of the transverse phase-space distribution of bunches created in our novel setup. As a more practical method to determine the emittance of the bunch we have performed a waist scan, that is presented in Sec. 8.2. In Sec. 8.3 we draw our conclusions.
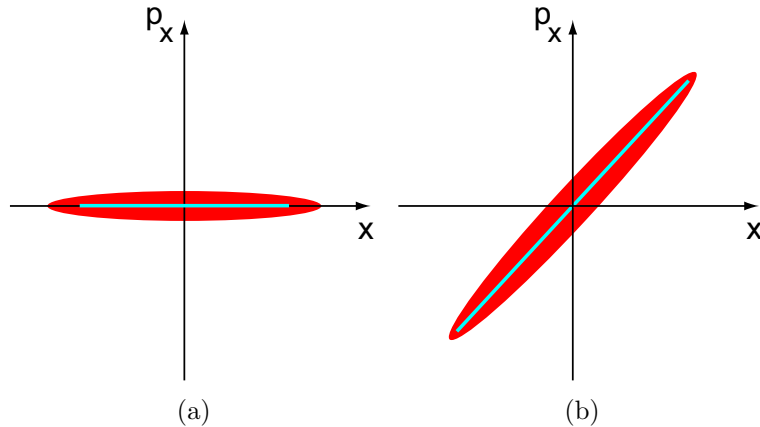
Figure 8.1: *Schematic (x, p_x) phase-space distribution of a zero-temperature waterbag bunch (blue line) and of a nonzero-temperature waterbag bunch (red ellips). (a) At $t = 0$ the matrix $\mathbf{D} = \mathbf{0}$ in Eq. (8.1) and the phase-space distribution is oriented along the x-axis. (b) At $t \neq 0$ the phase-space distribution is skewed.*

8.1   Transverse phase-space measurements

To measure the transverse phase-space distribution a pinhole can be scanned across the beam. By measuring, at all transverse positions in the beam, the average angle and the angular

spread of the beamlet emerging from the pinhole, the transverse phase-space distribution can be fully mapped. If the x- and y-phase-spaces are completely decoupled a slit can be used instead of a pinhole. We applied this latter method in order to have a better signal to noise ratio.

The setup is as depicted in Fig. 6.3, with the compression cavity removed and the streak cavity replaced by a vacuum cube, in which a $10\,\mu$m slit can be translated with a calibrated linear feedthrough. The angle x' and local angular spread are determined from the position and the width of the projection of the slit onto a micro-channel plate MCP, that is placed at a distance $430\,$mm downstream of the slit.

Electron bunches are created by photoemission with transversely shaped femtosecond laser pulses, see Sec. 4.1.3. Pinholes with radii of $50\,\mu$m and $100\,\mu$m have been used to create a truncated Gaussian laser profile. The measured (x, x')- and (y, y')-trace-spaces of $95.0\,$keV bunches of charges in the range of $0.1-1\,$pC are shown in Figs. 8.2(a) and 8.2(b). The measured local angular spread $\sigma_{x'} \approx \sigma_{y'} \sim 0.1\,$mrad is too small to be discerned on the scale of the figures.

For the case of a $0.1\,$pC bunch with an initial radius of $100\,\mu$m the phase-space distribution is almost linear. For this initial charge density it is expected that a waterbag bunch can be obtained, as indicated by the dot in the waterbag existence regime in Fig. 2.3. For higher initial space-charge densities the image-charge field strengths are on the same order of magnitude as the acceleration field strength, leading to a nonlinear bunch expansion and thus a non-waterbag distribution. This is confirmed by the measurements: for bunches with higher initial charge densities the trace-space distributions clearly show the typical S-shape.

The projection of the phase-space of a $0.1\,$pC bunch, with initial radius $100\,\mu$m, onto the (x, y)-plane is shown in Fig. 8.3. Integration in either the x- or y- direction yields a parabolic density profile, as expected for a waterbag bunch, see Sec. 2.2.1. This is a second necessary, but insufficient, condition for having realized a waterbag bunch indeed.
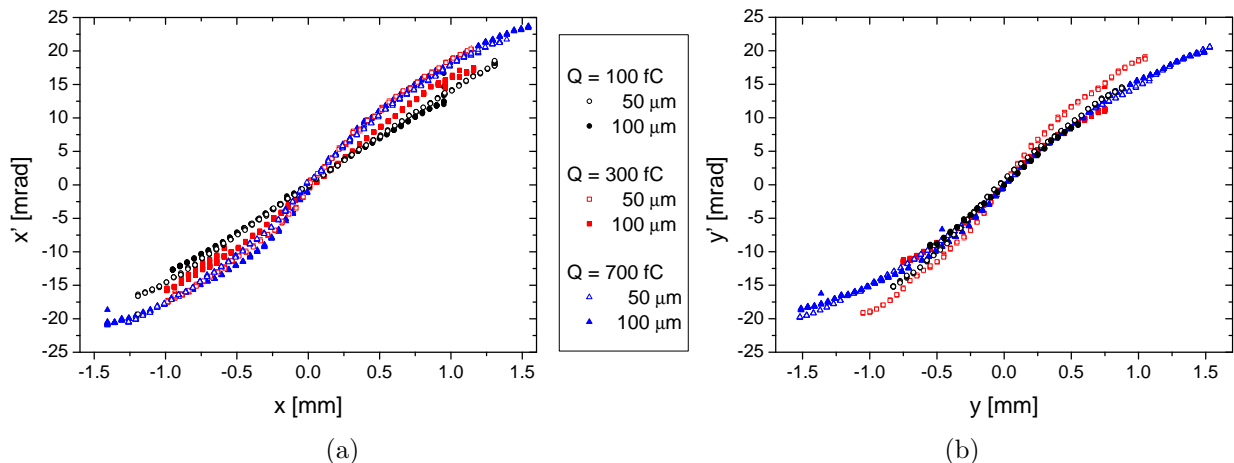
Figure 8.2: *(a) Transverse trace-space (x, x') and (b) trace-space (y, y') of bunches of different charges and different initial radii.*

In principle, the transverse emittance of a bunch can be calculated from its trace-space distribution by Eq. (2.3). However, we have not yet measured the local trace-space densities
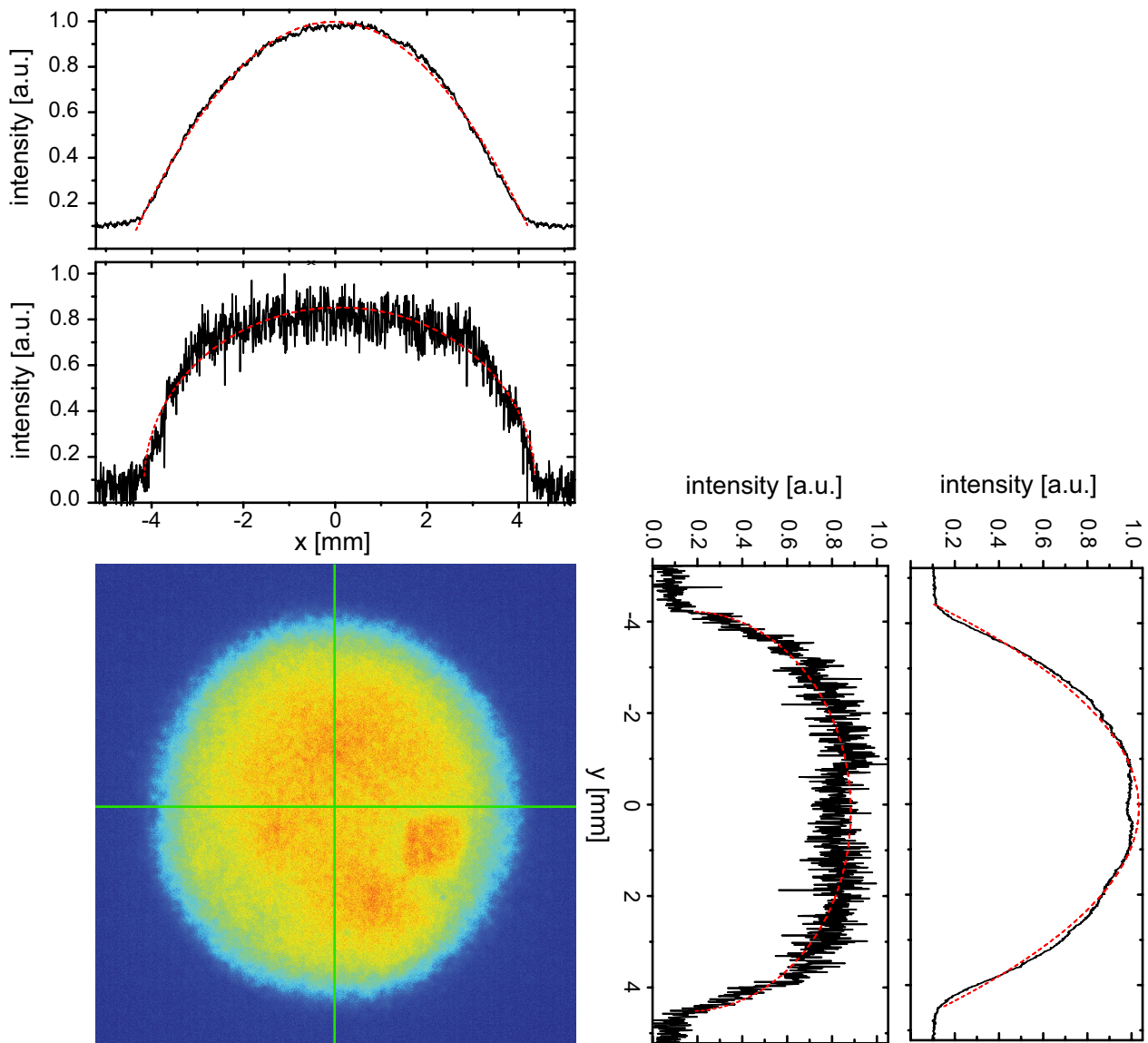
Figure 8.3: *Projection of the phase-space distribution onto the (x, y)-plane of a $0.1\,\text{pC}$ bunch, created with an ultrashort laser pulse with a Gaussian transverse intensity profile, that is truncated at a radius of $100\,\mu\text{m}$, corresponding to the $1\,\sigma$ point. Also shown are the profiles (black solid lines) of the horizontal and vertical lineout through the center of the spot (as indicated by the green lines), fitted to a half-circular profile (red dashed lines). The outer panels show the resulting profiles (black solid lines) after integration in the x-direction (right panel) and y-direction (top panel) and parabolic fits (red dashed lines).*

with sufficient accuracy. If we assume a parabolic density distribution, in accordance with the phase-space distribution of a waterbag bunch, the resulting emittance is a factor 4 higher than the value expected, which is the thermal value. The reason for this difference is presently not understood.

8.2   Emittance measurement

A more straightforward method to measure the emittance is by means of a waist scan. The propagation of a charged particle beam, with negligible space-charge fields, is fully analogous to the propagation of a TEM_{00} light beam with the optical wavelength replaced by $4\pi\varepsilon_x$. To determine the emittance, the spotsize σ_x is measured at a fixed distance l_s, as a function of the focal strength f_x of a solenoid. This is schematically shown in Fig. 8.4. The geometrical emittance ε_x can be determined using

$$\sigma_x = \frac{\sigma_v}{f_x}\sqrt{\frac{\varepsilon_x^2}{\sigma_v^4}\left[(f_x - l_s)l_v + f_x l_s\right]^2 + \left[f_x - l_s\right]^2}. \tag{8.4}$$

In this equation the position at a distance l_v in front of the solenoid can be seen as a virtual object distance, where the waist (of a virtual source) is σ_v.
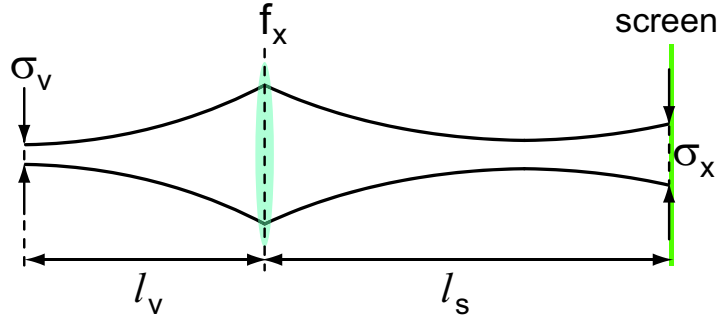

Figure 8.4: *Schematic of focusing a divergent beam, and definition of the parameters in Eq. (8.4).*

The setup is the same as in the previous section. In the early stage of the work presented in this thesis, we used a Gaussian transverse laser profile for photoemission with $\sigma_x = \sigma_y = 0.45\,\text{mm}$. We accelerated $0.3\,\text{pC}$ bunches to $40\,\text{keV}$. The current of the first solenoid is fixed at a value such that the beam is approximately collimated. Figure 8.5 shows the RMS spotsize as a function of the focal length of the second solenoid, which we calculated using Eqs. (4.1) and (4.2). The data are fitted to Eq. (8.4), yielding the emittance, and the virtual source distance l_v and size σ_v. The thermal emittance is calculated using $\varepsilon_{n,x}^{th} = \sigma_{x,laser} \cdot 8 \cdot 10^{-4}$ [2]. The laser spotsize $\sigma_{x,laser}$ is measured at the virtual cathode (see Sec. 4.1.3). The emittances thus obtained are summarized in Table 8.1.

Firstly, it is remarkable that $\varepsilon_{n,y} < \varepsilon_{n,x}$, while the minimum of σ_y is larger than the minimum of σ_x (see Fig. 8.5). This could be explained by astigmatism present in the beam. If the spotsize at the solenoid is smaller, the waist of the bunch will be larger. The different values of the fitting parameter σ_v for the x- and y-direction confirm that astigmatism could explain this, at first sight, inconsistency.

Secondly, the emittance is a factor two or three higher than the thermal emittance. Because we used a Gaussian laser pulse emittance conservation is not expected and an increase by a factor two or three seems reasonable. However, the emittance growth for Gaussian bunches should be compared to GPT simulations.
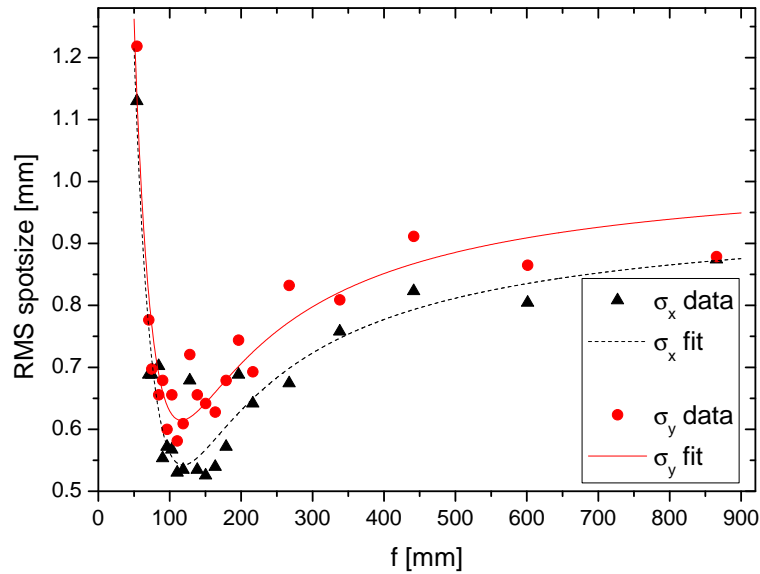
Figure 8.5: *RMS spotsize as a function of the focal length f of the second solenoid. The data are fitted to Eq. (8.4).*

Table 8.1: *Thermal emittance and normalized emittance as measured through a waist scan.*

direction	$\varepsilon_{n,th}$ [μm]	ε_n [μm]	σ_v [mm]	l_v [mm]
x	0.2	0.6	0.45	70
y	0.2	0.4	0.32	70

8.3   Conclusions

The first preliminary measurements of the transverse phase-space distribution and transverse beam profile presented in this chapter indicate the realization of a 95 keV, 0.1 pC waterbag bunch. However, the emittance cannot be determined accurately from these measurements. To indisputably claim the realization of sub-relativistic waterbag bunches also the longitudinal phase-space has to be measured. In addition, the deviations from linear behavior, which occur for initial charge densities $\gtrsim 50\,\mathrm{pC/mm^2}$ in an acceleration field of 10 MV/m, and which we attribute to image-charge fields that are nonlinear functions of position, should be studied analytically.

The emittance is, even for a Gaussian beam, only a factor two or three higher than the thermal value, which is sufficient for electron diffraction experiments.

References

[1] O. J. Luiten, S. B. van der Geer, M. J. de Loos, F. B. Kiewiet, and M. J. van der Wiel, Phys. Rev. Let. **93**, 094802 (2004).

[2] Ph. Piot, Review of experimental results on high-brightness photo-emission electron sources, in *The Physics and Applications of High Brightness Electron Beams*, edited by J. Rosenzweig, G. Travish, and L. Serafini, page 127, 2002.

9

Conclusions and recommendations

9.1 Conclusions

In this thesis we show full control and subsequent inversion of the Coulomb explosion of space-charge dominated electron bunches at sub-relativistic speeds. In particular, we demonstrate longitudinal compression in a single step by more than two orders of magnitude -a record by itself- to sub-100-fs bunch durations. To control the fourth dimension (time), i.e. to compress the electron bunches, we have introduced the use of a radio-frequency (RF) cavity. This constitutes a radical change in approach compared to existing ultrafast electron diffraction (UED) experiments. To show that high-quality diffraction patterns can be obtained with $\sim 10^6$ electrons in a single sub-100 fs shot, we have carried out a diffraction experiment on a gold nanolayer.

Compared to state-of-the-art UED experiments we have improved the temporal resolution by a factor five, and combined this with an increased bunch charge by at least two orders of magnitude. Thereby we have provided a 'poor man's X-FEL' (X-ray Free Electron laser) in the sense that single-shot, sub-relativistic, femtosecond electron diffraction can be performed. The bunch compression results and single-shot diffraction patterns presented in this thesis pave the way for the study of structural dynamics with atomic spatio-temporal resolution.

9.2 Recommendations

Ideally the bunch should be a uniformly charged ellipsoid (or 'waterbag' bunch), because this is the only charge distribution with linear space-charge fields. The preliminary transverse phase-space measurements presented in this thesis indicate that we have created waterbag-like bunches. Strictly speaking, to claim the realization of waterbag bunches also the longitudinal phase-space has to be measured. This can be done with, e.g., the streak cavity (that we have used for bunch length measurements) in combination with a constant transverse magnetic field perpendicular to the streaking magnetic field. In this way the energy-time-correlation of a bunch can be obtained.

Further, by measuring all three 2D phase-spaces of bunches of different initial charge densities (at the cathode) the 'waterbag existence regime regime' can be mapped in which a thin sheet of electrons will develop into a waterbag bunch. Outside the waterbag existence regime nonlinearities of the image-charge field are expected to degrade the beam quality.

This can be examined in more detail both analytically and by particle tracking simulations with, e.g., the GPT code.

Besides these two more academic issues there is quite some practical potential to create even brighter bunches, i.e. shorter bunches with improved transverse coherence. To explore the limits we recommend further research on potential sources of aberrations, on RF compression, and on the electron source itself. These issues are discussed below.

When having created a high-quality waterbag bunch the (transverse) coherence should not be spoiled by nonlinear electro-magnetic fields, i.e. the charged particle optics have to be aberration-free. The main component to be explored in this sense is the RF compression cavity. Our experiments convincingly show that the bunches we have realized are of sufficient quality for single-shot electron diffraction, in agreement with our expectations based on GPT simulations that include the detailed field map of the cavity. For further beam quality optimization however, the effect of the nonlinear fringe fields (at the cavity apertures) and of (spherical) aberrations of the field inside the cavity should be studied.

Also the compression limits have to be further looked into. We measured bunch durations as small as 67 fs, but compression of 0.1 pC bunches down to 10 fs should be possible according to GPT simulations. To achieve this, the amplitude of the RF field has to be increased, resulting in a shorter bunch at a focal position closer to the cavity. The energy spread in the focus will then be larger, leading to a smaller longitudinal coherence length. As the longitudinal coherence length of our bunches is an order of magnitude larger than the transverse coherence length, a small decrease in favor of a shorter bunch can be allowed. Furthermore, when looking into the limits of longitudinal compression combined with transverse focusing (which is usually the case in UED experiments) path length differences have to be considered.

Finally, if a true waterbag bunch has been created and if all optics are aberration-free, the only source for deviation from a linear phase-space would be the thermal, i.e., uncorrelated velocities related to the creation of free electrons. It is therefore the electron source that limits the bunch quality: the initial (thermal) energy spread has to be lowered. In our group promising research is being carried out on an ultracold plasma, from which electron bunches are extracted that have a 1000 times lower effective temperature compared to photoemitted bunches [1]. The transverse coherence length of such 'ultracold' bunches is on the order of 10 nm. Combining this ultracold electron source with the RF compression technique would extend the applicability of the poor man's X-FEL presented in this thesis to the study of femtosecond dynamics of relatively large molecules, like proteins and viruses. This would undoubtedly generate new insight into the building-blocks of life.

References

[1] G. Taban, *A cold atom electron source*, PhD thesis, Technische Universiteit Eindhoven, 2009.

Summary

In this thesis we show unprecedented 100-fold compression of space-charge dominated electron bunches to sub-100 fs durations. Thereby we show for the first time full control of the fourth dimension (time) of sub-relativistic electron bunches. With 95 keV the kinetic energy of the electrons is within the optimum range of 30 – 300 keV for diffraction experiments. Furthermore, our bunches carry sufficient charge to record a diffraction pattern using only a single bunch. Compared to state-of-the-art diffraction setups we have increased the bunch charge by two orders of magnitude, combined with a factor 5 improved temporal resolution. With the work presented in this thesis we pave the way for the study of structural dynamics by means of single-shot, femtosecond electron diffraction.

To realize extremely short, highly charged bunches the problem to be overcome is irreversible expansion due to the repelling Coulomb force. A uniformly charged ellipsoidal bunch, or 'waterbag' bunch, is the only distribution that has space-charge fields which are linear functions of position. Its expansion is therefore reversible with external linear electro-magnetic fields. We have introduced the use of waterbag bunches into the sub-relativistic regime. In Ch. 2 we present analytical equations in closed form that describe the space-charge induced expansion of waterbag bunches.

We create electron bunches by femtosecond photoemission in a 100 kV DC photogun. The necessary transverse shaping of the laser pulses and the robust design of the DC photogun are described in detail in Ch. 4. To compress the electron bunches we use an oscillatory electric field, sustained in a 3 GHz resonant radio-frequency (RF) cavity. This cavity thus acts as a temporal lens, a novelty in the sub-relativistic regime (see Ch. 3). Its shape has been optimized for power efficiency, saving about 90% power compared to a regular pillbox design. To measure the bunch length we use a 3 GHz streaking camera, in which the deflector is another power efficient RF cavity. The strategy for power optimization of both cavities and the resulting designs are presented in Ch. 5. The resonant frequencies and the on-axis field profiles are in excellent agreement with the results of the numerical Poison solvers that we used to design the cavities.

At optimum settings of the RF field amplitude and phase offset a shortest bunch duration of 67 fs has been measured for a 0.1 pC, 95 keV bunch (see Ch. 6). Bunch duration measurements as a function of the RF amplitude and the phase offset are in good agreement with state-of-the-art particle tracking simulations that include all Coulomb interactions of the electrons in the bunch, and utilize the detailed fieldmaps of the accelerator and the RF cavity.

To show that our bunches are of sufficient quality for diffraction experiments, in terms of

angular and energy spread, we have recorded single-shot diffraction patterns of a polycrystalline gold nanolayer (see Ch. 7). The four lowest-order diffraction peaks are easily resolved and their positions are in excellent agreement with theoretical values.

Finally, preliminary measurements of the transverse phase-space and the transverse density profile of our bunches indicate that we have realized 95 keV, 0.1pC waterbag-like bunches (see Ch. 8). Further measurements on the longitudinal phase-space are desirable to confirm the realization of true waterbag bunches.

With the work presented in this thesis we show that sub-relativistic single-shot femtosecond electron diffraction is possible. Thereby we provide an important analytical tool for the study of structural dynamics in, e.g., phase transitions, chemical reactions, and conformation changes with both atomic spatial *and* temporal resolution, i.e., 1 Å and 100 fs. With the present 100 kV photogun, the transverse coherence length is on the order of 1 nm. This allows the study of dynamics in a wide range of samples, that consist of crystals of atoms or small molecules. Our temporal charged-particle lens (i.e., the RF compression cavity) may be used as well in combination with the extraction of electron bunches from an ultracold plasma (another development in our research group), instead of extraction from a photocathode. This would lead to an increase of the transverse coherence length of the electron bunches by an order of magnitude. Such a development would enable the study of dynamics of relatively large (bio-)molecules at the atomic spatio-temporal scale, which will undoubtedly lead to new insight into the building-blocks of life.

Valorization

In this thesis we demonstrate single-shot femtosecond electron diffraction, as a table-top alternative to X-ray diffraction as presently being pursued at the recently commissioned X-ray Free Electron Laser (X-FEL) LCLS at Stanford. Our alternative, a 'poor man's X-FEL', does not require taking samples to, or in fact installing a custom sample-preparation chamber at, such a giant facility. Instead, we offer the solution of adding a 1-meter size beam line to an existing sample chamber, thus providing convenient access to femtosecond diffraction technology in a normal laboratory.

Compared to state-of-the-art ultrafast electron diffraction (UED) setups, our setup has four advantages: (1) there is a time-focus of the electron bunch rather then a continuous expansion; (2) the position of the time-focus is adjustable to fit the geometry of the sample chamber; (3) single-shot operation; (4) five times higher temporal resolution. These advantages are the result of the inclusion of a temporal charged-particle lens, whereas state-of-the-art UED setups can be seen as a 'camera obscura' in the longitudinal sense (i.e., there is no lens acting on the bunch length). The temporal lens we designed is a power-efficient 3 GHz radio-frequency (RF) resonant cavity, driven by a 100W solid-state RF amplifier.

Since the beginning of my PhD project our group has been in contact with two pioneering groups in the UED-field: the Miller group at the University of Toronto and the Siwick group at McGill University. This has already resulted in transfer of the designs of our DC photogun and RF compression cavity to these groups. Further contacts are intensified by the exchange of students.

At the 2007 FEMMS conference I initiated the contact with Sommersdijk (Chemical Technology, Eindhoven University of Technology), who is presently planning incorporation of a sample stage in our UED setup, appropriate for his research on (macro-)molecular assemblies and biomimetic mineralization. Further PR contacts with the UED community have been made by presentations at the 2008 and 2010 Ultrafast Phenomena conferences, and at the 2009 MRS Fall conference.

At the end of my PhD period the interest in our setup increased further, by giving seminars and conference presentations, from Carbone (Laboratory of Ultrafast Spectroscopy at cole Polytechnique Fdrale de Lausanne), Rudolf (surfaces and thin films group at the University of Groningen), Van der Zande (molecular and laser physics group at Radboud Universiteit Nijmegen), Centurion (Ultrafast Dynamics group at the University of Nebraska-Lincoln), and Parmigiani (condensed matter, strongly correlated electron systems at the University of Trieste). This has resulted in urgent requests for knowledge transfer or preferably reproduction of our compression cavity or the entire setup.

Naturally FEI Company, the world leader in electron microscopy and small SEM/diffractometers, was the first party to approach when considering valorization of our development. FEI has definitely shown interest in our research, as exemplified by the fact that the Eindhoven research director is member of my thesis committee. However, at this early stage the development of a new microscope or stand-alone diffractometer that includes our compression cavity does not yet appear to fit the company's strategy.

Since we were determined to pursue valorization, discussions were started with AccTec B.V., a full daughter of TUE-Holding. The CQT group (at the TU/E), in which I carried out my PhD research, has strong ties with AccTec. Through this connection AccTec has an appropriate network of potential scientific customers, and is close to the source of new developments in beam physics. AccTec has already experience in acting as the vehicle to market earlier 'products' of the research of the CQT group to scientific customers: these products include an RF photogun, an RF mode converter and a laser/RF synchronization system with world-record low time jitter. AccTec is currently taking steps to market, at first instance, a 'construction kit' containing the 100kV DC photogun, the RF compression cavity, solenoids, steering coils, and a miniaturized deflector cavity (for bunch length measurements). The package also includes the synchronization system, necessary to launch the electron bunches into the cavity with low jitter with respect to the RF-phase, and a particle tracking code for optimizing the beam line design to fit the customer's sample chamber. This code, GPT, has been selling worldwide by Pulsar Physics v.o.f., an earlier spin-off of the CQT-group, and will be equipped with the field maps of all electron-optical components of the diffraction beam line. The approach of a construction kit is favored over producing a complete stand-alone apparatus, because potential customers generally already have a large and complicated sample preparation chamber as their core business.

In the envisaged AccTec/CQT collaboration, it is anticipated that CQT participates in first demonstration experiments with the early lead customers. After a number of publications in high-impact journals, and further PR at conferences, the scientific market is expected to grow by itself, judging from the attendance at Ultrafast Phenomena conferences and recent interest in our setup from the earlier mentioned research groups at universities in Europe as well as in the USA. A likely scenario is that a point will be reached where AccTec will be in a position to return to FEI Company for a possible take-over of our commercial activities.

With the marketing strategy as described in this chapter we are confident that we optimally utilize our beam physics knowledge and experience in designing and fabricating the crucial components of a device, that provides exciting new possibilities to serve the exponentially growing UED community.

Nawoord

Tijden mijn promotie-onderzoek heb ik ondersteuning gehad en gevoeld van een aantal mensen die ik in dit nawoord graag daarvoor wil bedanken. Wat ik tegen jullie wil zeggen, kan samengevat worden met het volgende citaat waarvan ik helaas de auteur niet kon achterhalen: "Teamwork is working together - even when apart."

Op de eerste plaats wil ik graag mijn co-promotor Jom Luiten bedanken. Tijdens mijn afstudeerperiode heb je me enthousiast gemaakt om mijn werk voort te zetten middels een promotie. Dank voor het vertrouwen dat je me hebt gegeven om mij een ambitieus project op me te laten nemen. En als het tegen zat tijdens mijn promotie heeft jouw immer positive instelling me gesterkt in het doorzetten van mijn experimenten, die uiteindelijk een schitterend resultaat hebben opgeleverd.

In dit licht wil ik ook mijn promotor Marnix van der Wiel bedanken. Als ik even op een dood spoor zat, wist jij met je kritische blik altijd weer een zetje te geven. Helaas was je na je emeritaat logischerwijs minder vaak aanwezig, maar je belangstelling voor mijn onderzoek heb ik altijd blijven voelen. Ik heb grote waardering voor de manier waarop je kritisch en bondig, maar tegelijkertijd open, mijn werk hebt becommentarieerd.

De opstelling waarmee ik uiteindelijk mijn experimenten gedaan heb, is het resultaat van een samenwerking met een aantal technici en studenten. Met name Eddy Rietman en Ad Kemper waren van begin af aan hartstochtelijk betrokken bij de ontwikkeling van mijn opstelling. De manier waarop we met elkaar mijn wensen hebben kunnen combineren met jullie mechanische en elektrische inbreng vond ik erg prettig en heeft geresulteerd in een betrouwbare opstelling. Nog een vijftal technici stond altijd paraat om onderdelen van mijn opstelling te maken of aan te passen. Harry van Doorn, Wim Kemper, Jolanda van de Ven, Louis van Mol, en Iman Koole bedankt dat ik altijd op jullie ad hoc hulp kon rekenen.

Op deze plaats wil ik ook twee afstudeerders noemen. Erwin de Jong en Jacco Nohlmans, jullie hebben de twee zuinige cavities in mijn opstelling ontworpen, waarmee ik uiteindelijk elektronen bunches heb gecomprimeerd en gemeten. Dankzij jullie inbreng is de opstelling compact gebleven en is mijn RF kennis verder uitgebreid.

In het lab was ik -gelukkig- zelden alleen. De allereerste conditionering van de versneller was samen met Wim Urbanus, de eerste tests met de streak cavity heb ik gedaan met Christian Roelofs, en bij de compressie metingen en de diffractie metingen heeft Arjan Klessens meegeholpen. Bij die laatste metingen kon ik ook rekenen op de steun van Peter Pasmans, die mijn opstelling gaat gebruiken om daadwerkelijk tijdopgeloste diffractie experimenten te doen. Peter, tijdens mijn laatste (jouw eerste) jaar hebben we veel samengewerkt en ik ben blij dat mijn opstelling is overgegaan in goede handen.

Alhoewel niet direct bij mijn project betrokken heb ik met name op laser-gebied veel

steun gehad aan Seth Brussaard, die net als ik zich niet kan inhouden om aan spiegeltjes te draaien om de laser puls te optimaliseren. Na de fusie met de AQT-groep was ook Edgar Vredenbregt regelmatig in het CQT-lab aanwezig. Met je parate fysische èn technische kennis was je een ideale discussie partner 'on the spot'.

Voor alle GPT simulaties wil ik Bas en Marieke erg bedanken! Als ik tegen onverwachte effecten aanliep, en toen ik er in het lab maar niet achter kwam waarom de elektronen bunch niet korter werd, waren jullie daar om uitgebreide simulaties te doen. En Bas, het dagdromen is voorbij, die oversteek naar Engeland komt er gewoon!

Mijn mede-promovendi wil ik bedanken voor de bereidheid om elkaar te helpen, de een meer met de handen, de ander meer met het hoofd. Merijn, we zijn begonnen in dezelfde trein en geëindigd in hetzelfde bureau. Samen hebben we veel gediscussieerd, en als het over onze opstellingen ging liepen we iedere keer weer in dezelfde valkuil...

Willem en Xavier, wij hebben drie jaar lang één laser-systeem moeten delen. Ondanks tegenstrijdige belangen hebben we daar toch in harmonie het beste van gemaakt en hebben we op een prettige manier het lab gedeeld. Bedankt hiervoor!

Tijdens mijn promotie heb ik ook een aantal stagiairs begeleid. Paul Lumens, Erwin Smakman, Rossella Porrazzo, en Joost Daniëls, bedankt voor jullie bijdrage en gezelligheid.

Het citaat aan het begin van dit nawoord is misschien nog wel het meest van toepassing op de mensen die het verste weg stonden van mijn dagelijkse bezigheden. Ondanks dat mijn ouders, mijn broer en Franka zich maar moeilijk voor konden stellen welke problemen mij bezig hielden, heb ik toch onvoorwaardelijk steun, begrip en liefde ontvangen. Pap, mam, Joost & Franka, wat fijn dat ik altijd op jullie kan rekenen!

Curriculum vitae

14 juni 1982   geboren te Bergen op Zoom, Nederland

1994 - 2000   Gymnasium
Katholieke Scholengemeenschap Etten-Leur

2000 - 2001   Propedeuse Technische Natuurkunde
Technische Universiteit Eindhoven

2001 - 2006   Ingenieur Technische Natuurkunde
Technische Universiteit Eindhoven

2004   Bedrijfsstage
TNO
afdeling: Technisch Physische Dienst (TPD), Eindhoven

2006 - 2010   Onderzoeker in Opleiding
Stichting FOM
Technische Universiteit Eindhoven
faculteit: Technische Natuurkunde
capaciteitsgroep: Coherentie & Quantum Technologie (CQT)

2010 - heden   research engineer
MA3 solutions